

ENTANGLEMENT GENERATION AND QUANTUM
CHEMISTRY: QUANTUM MECHANICS AT THE
EXPONENTIAL SCALE

A Dissertation

Presented to the Faculty of the Graduate School

of Cornell University

in Partial Fulfillment of the Requirements for the Degree of

Doctor of Philosophy

by

Matthew Joseph Otten

May 2018

© 2018 Matthew Joseph Otten
ALL RIGHTS RESERVED

ENTANGLEMENT GENERATION AND QUANTUM CHEMISTRY:
QUANTUM MECHANICS AT THE EXPONENTIAL SCALE

Matthew Joseph Otten, Ph.D.

Cornell University 2018

This thesis concerns two main subjects: the parallelization and applications of a recently developed quantum chemistry method known as heat-bath configuration interaction (Chapter 2) and the generation of entanglement in plasmonically coupled quantum dots (Chapters 3 and 4).

Chapter 2 describes the implementation (with a careful eye towards parallelization) and applications of the recently developed heat-bath configuration interaction (HCI) algorithm. HCI is a fast selected configuration interaction plus perturbation theory method for finding the exact energy of small, challenging systems within a given basis. Though it is faster than many alternatives, it is still an exponentially scaling algorithm; careful implementation and the use of parallel computing are necessary to study interesting systems. We describe the important implementation and parallelization details, along with providing performance results. We then apply the method to two interesting systems: solid silicon, as a benchmark for other quantum chemistry methods, and the binding curve of Cr_2 , which cannot be computed reliably by any of the other state of the art algorithms.

Chapter 3 concerns the modeling of the quantum dynamics of two, three, or four quantum dots in proximity to a plasmonic system such as a metal nanoparticle or an array of metal nanoparticles. For all systems, an initial state with only one quantum dot in its excited state evolves spontaneously into a state with entanglement between all pairs of QDs. The entanglement arises from the couplings

of the QDs to the dissipative, plasmonic environment. Moreover, we predict that similarly entangled states can be generated in systems with appropriate geometries, starting in their ground states, by exciting the entire system with a single, ultrafast laser pulse. By using a series of repeated pulses, the system can also be prepared in an entangled state at an arbitrary time.

Chapter 4 investigates systems of two or more quantum dots interacting with a dissipative plasmonic nanostructure by using a cavity quantum electrodynamics approach with a model Hamiltonian. We focus on determining and understanding system configurations that generate multiple bipartite quantum entanglements between the occupation states of the quantum dots. These configurations include allowing for the quantum dots to be asymmetrically coupled to the plasmonic system. Analytical solution of a simplified limit for an arbitrary number of quantum dots and numerical simulations and optimization for the two- and three-dot cases are used to develop guidelines for maximizing the bipartite entanglements. For any number of quantum dots, we show that through simple starting states and parameter guidelines, one quantum dot can be made to share a strong amount of bipartite entanglement with all other quantum dots in the system, while entangling all other pairs to a lesser degree.

BIOGRAPHICAL SKETCH

Matthew Joseph Otten was born and grew up in Granite City, Illinois, a suburb of St. Louis, Missouri. After graduating from Granite City High School, he attended the Illinois Institute of Technology, graduating with a B.S. in physics and a minor in the philosophy and sociology of science and technology. While an undergraduate, Matthew did research at Argonne National Laboratory, both in the Advanced Photon Source and the Mathematics and Computer Science divisions. He then came to Cornell University to obtain a Ph.D. in the department of physics, working under Cyrus Umrigar, studying highly accurate electronic structure methods. During his Ph.D., he was a Givens Associate at Argonne National Laboratory, studying the dynamics of lossy quantum systems with Stephen Gray and parallelization on novel computing architectures with Misun Min. Matthew also spent time as a Livermore Graduate Scholar at Lawrence Livermore National Laboratory, working jointly with Miguel Morales and Cyrus Umrigar on electronic structure methods.

To my family.

ACKNOWLEDGEMENTS

I would like to thank the many mentors I have had the privilege of working with over the years. First and foremost, I am grateful to Dr. Cyrus Umrigar for his guidance, support, and wealth of knowledge, as well as his patience with my many forays into other (sometimes unrelated) projects. I am also grateful for Dr. Misun Min, for introducing me to and allowing me to work on some of the largest computers in the world; Dr. Stephen Gray, for useful discussions on lossy quantum dynamics; Dr. Miguel Morales, for key insights on how to apply the many computational techniques I learned to useful systems; and Dr. Gregory Fuchs, for grounding some of my ideas with experimental realism and for reading this thesis. I would also like to thank the other members of my committee, Dr. Daniel Ralph and Dr. Erich Mueller for serving on my committee and, especially, for commenting on this thesis. I thank Dr. Tomas Arias and the rest of his group for the use of computing resources. I am grateful to the Umrigar research group for useful collaborations. To the rest of the faculty and staff of the Cornell physics department, I say thanks for the inspiring classes, lectures, and discussions and the help through my many bureaucratically difficult situations (especially Kacey Bray Acquilano and Deb Hatfield).

TABLE OF CONTENTS

Biographical Sketch	iii
Dedication	iv
Acknowledgements	v
Table of Contents	vi
List of Tables	viii
List of Figures	ix
1 Introduction	1
2 Parallelization and applications of heat-bath configuration interaction	7
2.1 Introduction	8
2.1.1 Brief Overview of Heat-bath Configuration Interaction . . .	10
2.2 Implementation and Parallelization Details	14
2.2.1 Variational Stage	15
2.2.2 Perturbative Stage	18
2.2.3 Performance Results	19
2.3 Applications	21
2.3.1 Benchmarking Other Methods	21
2.3.2 Chromium Dimer	23
2.4 Conclusion	26
3 Entanglement of two, three, or four plasmonically coupled quantum dots	28
3.1 Introduction	29
3.2 Theoretical Methods	30
3.3 Results	32
3.3.1 Entanglement in the dark	32
3.3.2 Entanglement with optical pulses	34
3.4 Concluding Remarks	40
4 Origins and optimization of entanglement in plasmonically coupled quantum dots	42
4.1 Introduction	43
4.2 Theoretical Methods	45
4.2.1 Approximate Analysis	47
4.2.2 Concurrence Optimization	51
4.2.3 Simulation Details	52
4.3 Results	53
4.3.1 Two Quantum Dots in the Dark	53
4.3.2 $N > 2$ Quantum Dots in the Dark	59
4.3.3 Two Quantum Dots Subjected to Ultrafast Laser Pulses . .	62
4.3.4 Three Quantum Dots Subjected to Ultrafast Laser Pulses . .	66

4.4	Concluding Remarks	70
5	Conclusion	74
A	Appendix for “Parallelization and applications of heat-bath configuration interaction”	76
A.1	Efficient Generation of Hamiltonian Matrix	77
A.1.1	Key Variables	77
A.1.2	Setup	78
A.1.3	Constructing the Hamiltonian	79
B	Supporting Material for “Entanglement of two, three, or four plasmonically coupled quantum dots”	81
B.1	Quantum Master Equation	82
B.2	Concurrence	86
B.3	Numerical Aspects	87
B.4	Concurrence Results for Different Parameter Choices	88
B.4.1	Dark Results with Smaller Couplings	88
B.4.2	Pulsed Results with Smaller Couplings	88
B.4.3	Quantum Dots with Different Energy Levels	90
C	Supporting Material for “Origins and optimization of entanglement in plasmonically coupled quantum dots”	92
C.1	Three and $N + 1$ State Models	93
C.2	Local Field Enhancement	101
	Bibliography	103

LIST OF TABLES

4.1	Constraints for optimization parameters.	62
4.2	Summary of optimization run results for a laser pulse interacting with a system composed of two and three quantum dots. An “ <i>f</i> ” denotes that the parameter value was fixed and therefore not optimized over.	69

LIST OF FIGURES

2.1	HCI parallel efficiency. The variational stage sees a gain of roughly $1.7\times$ when doubling the number of cores. The perturbative stage benefits from both core count and increased memory; increasing the number of nodes increases the memory and leads to superlinear scaling.	20
2.2	Benchmarking quantum chemistry methods using HCI. The HCI curve represents the essentially exact answer; CCSD has a nearly constant error for the different volumes, whereas MP2's error varies for the different systems.	22
2.3	HCI calculations and experimental results for Cr_2 in the cc-pVDZ-DK basis set, correlating 12 electrons. E_{bind} represents the binding energy. The HCI curve is qualitatively very far off from the DMRG-NEVPT2 and experimental curves. The two experimental curves differ by about 0.1 eV, reflecting the uncertainty in the experimental dissociation energy.	25
2.4	HCI calculations and experimental results for Cr_2 in the cc-pVDZ-DK basis set, correlating 28 electrons. E_{bind} represents the binding energy. The HCI curve agrees qualitatively very well with the DMRG-NEVPT2 and experimental curves. The two experimental curves differ by about 0.1 eV, reflecting the uncertainty in the experimental dissociation energy.	27
3.1	(a) Diagram of a plasmonic-two-QD system composed of three metal nanoparticles (the plasmonic system, labeled 'SP') with QDs (labeled 'QD1' and 'QD2') in the interparticle gaps. Bipartite concurrence of two (b), three (c), and four (d) QD systems where one of the QDs (QD1) is initially excited, with $\hbar g_i = 30$ meV in all cases. $i:j$ refers to the concurrence between QDi and QDj. Part (b) also shows the population of the symmetric state $ S\rangle$, P_S , and of the antisymmetric state $ A\rangle$, P_A	34
3.2	Maximum concurrence when a plasmon-two-QD system initially in its ground state is exposed to a 20-fs laser pulse. (a) Concurrence as a function of laser-pulse fluence and plasmon-QD coupling coefficient for one of the QDs ($g_1 = g_2 + \Delta g$) relative to the other ($\hbar g_2 = 30$ meV). (b) Concurrence as a function of time, for coupling coefficients $\hbar g_1 = 15$ meV ($\Delta g = -15$ meV) and $\hbar g_2 = 30$ meV, and laser-pulse fluence 81 nJ/cm ² , that produce the largest concurrence. The populations of QD1 and QD2 are also plotted.	35
3.3	Results for a plasmon-three-QD system with laser-pulse fluence of 500 nJ/cm ² , and coupling coefficients $\hbar g_1 = 30$ meV and $\hbar g_2 = \hbar g_3 = 35$ meV. (a) Excited-state populations for the three QDs. (b) Bipartite concurrences.	37

3.4	Concurrences for a plasmon-three-QD system with a repeating 500 nJ/cm ² pulse. Coupling coefficients are $\hbar g_1 = 30$ meV, $\hbar g_2 = \hbar g_3 = 35$ meV. The dotted vertical lines represent the times associated with the maxima of the pulses.	38
4.1	Time dependence of the populations of the states $ S; s = 0\rangle$, $ A; s = 0\rangle$, and $ q_2 = 0, q_1 = 0; s = 1\rangle$, and the concurrence, for a two-QD system initially in the $ q_2 = 0, q_1 = 1; 0\rangle$ state, with no surface plasmon decay or QD dephasing, i.e., $\hbar\gamma_s = \hbar\gamma_d = 0$ meV. (a) A case with $g_1 < g_2$ corresponding to the initially excited QD1 not being as strongly coupled to the surface plasmon as QD2: $\hbar g_1 = 12.5$ meV, $\hbar g_2 = 25$ meV. (b) A case with $g_1 > g_2$: $\hbar g_1 = 25$ meV, $\hbar g_2 = 12.5$ meV.	55
4.2	Results for a surface plasmon decay width $\hbar\gamma_s = 100$ meV. Upper two panels (a) and (b) show the time-dependence of the the $ S; s = 0\rangle$, $ A; s = 0\rangle$, $ q_2 = 0, q_1 = 0; s = 1\rangle$ state populations and concurrence for a two-QD system, initially in the $ q_2 = 0, q_1 = 1; 0\rangle$ state, and with no QD dephasing, i.e., $\hbar\gamma_d = 0$ meV. The cases with (a) $\hbar g_1 = 12.5$ meV, $\hbar g_2 = 25$ meV and (b) $\hbar g_1 = 25$ meV, $\hbar g_2 = 12.5$ meV are displayed. The lower two panels (c) and (d) are the maximum concurrences found as a function of the QD/plasmon coupling factors, g_1 and g_2 . Panel (c) corresponds to no QD dephasing, $\gamma_d = 0$, and contains within it the concurrence maxima from the particular cases (a) and (b) above. Panel (d) is the corresponding maximum concurrence when the QD dephasing is set to $\hbar\gamma_d = 2.0$ meV. The dashed lines in (c) and (d) represent $g_2 = \sqrt{3}g_1$	57
4.3	Asymptotic figure of merit, Eq. (4.20) for a three-QD system, with one QD initially excited, $\gamma_s > 0$, and $\gamma_d = 0$, as a function of the ratios of the QD/plasmon coupling parameters.	61
4.4	Panels (a) and (b) show the time-dependence of the populations of the $ A\rangle$ and $ S\rangle$ states (traced over all $ s\rangle$) and concurrence for pulsed excitation of an initially cold two-QD/surface plasmon system with parameters $\hbar g_1 = 12.8$ meV, $\hbar g_2 = 24.9$ meV, $F = 263.4$ nJ/cm ² , $\tau = 12.5$ fs, $\hbar\gamma_s = 186$ meV, and $\hbar\gamma_d = 0$ meV. These parameters are the result of a local optimization run. Panels (c) and (d) keep these same parameter values except for the QD dephasing, which is either (c) $\hbar\gamma_d = 0.2$ meV or (d) $\hbar\gamma_d = 2$ meV.	63
4.5	Maximum concurrence for a parameter sweep of the two-QD system, with $\hbar g_2 = 30$ meV, $\tau = 20$ fs, $\hbar\gamma_s = 150$ meV, $\hbar\gamma_d = 2$ meV. The dashed lines represent coupling ratios obeying Eq. (4.19).	65

4.6	Populations and concurrences for the final parameters from a local optimization run on the three-QD system with $\hbar\gamma_d$ fixed at 0.2 meV. The final parameters are $\hbar g_1 = 14.6$ meV, $\hbar g_2 = 19.3$ meV, $\hbar g_3 = 19.3$ meV, $F = 587.0$ nJ/cm ² , $\tau = 36.4$ fs, and $\hbar\gamma_s = 180.4$ meV (with $\hbar\gamma_d$ fixed at 0.2 meV). Panel (a) shows the various bipartite concurrences, and panel (b) shows the QD excitation probabilities. Because $g_2 = g_3$, the QD3:QD1 and QD2:QD1 concurrences are identical, as are the QD2 and QD3 excitation probabilities. Panel (c) shows the time-dependent probabilities of the $ S\rangle$ and $ A\rangle$ states associated with either the QD3:QD1 or QD2:QD1 subsystems and the pulse envelope.	67
4.7	Populations and concurrences for the final parameters from a second local optimization run on the three-QD system with $\hbar\gamma_d$ fixed at 0.2 meV. The final parameters are $\hbar g_1 = 19.0$ meV, $\hbar g_2 = 16.3$ meV, $\hbar g_3 = 21.7$ meV, $F = 603.4$ nJ/cm ² , $\tau = 39.4$ fs, and $\hbar\gamma_s = 107.7$ meV (with $\hbar\gamma_d$ fixed at 0.2 meV). Panel (a) shows the various bipartite concurrences, and panel (b) shows the QD excitation probabilities. The pulse envelope and the populations of the $ S\rangle$ and $ A\rangle$ states are shown for the QD3:QD1 pair in panel (c) and the QD2:QD1 pair in panel (d).	68
B.1	Uncoupled ($g = 0$) and coupled ($g > 0$) QD/plasmon level structure for the case of two QDs interacting with a plasmon. The kets correspond to products of two-QD ($ 0, 0\rangle$, $ S\rangle$, $ A\rangle$) and plasmon ($ 0\rangle$, $ 1\rangle$) states. The $ S\rangle 0\rangle$ and $ 0, 0\rangle 1\rangle$ states mix and split relative to the $ A\rangle 0\rangle$ state, by energies $\pm\sqrt{2\hbar g}$	85
B.2	Concurrence as a function of time with QD1 initially excited, no laser, and various exciton-plasmon coupling strengths $\hbar g$, for different numbers of quantum dots. $i:j$ refers to the concurrence between QD <i>i</i> and QD <i>j</i>	89
B.3	Concurrence as a function of time with various coupling strengths and laser intensities. (a) Concurrence for a two-QD system with $\hbar g_1 = 8$ meV, $\hbar g_2 = 15$ meV, and a laser fluence of 298 nJ/cm ² . (b) Concurrence for a two-QD system with $\hbar g_1 = 5$ meV, $\hbar g_2 = 10$ meV, and a laser fluence of 662 nJ/cm ² . (c) Concurrence for a three-QD system with $\hbar g_1 = \hbar g_2 = 10.4$ meV, $\hbar g_3 = 24.8$ meV, and a laser fluence of 124 nJ/cm ² . (d) Concurrence for a three-QD system with $\hbar g_1 = \hbar g_2 = 14.8$ meV, $\hbar g_3 = 20$ meV, and a laser fluence of 293 nJ/cm ² . Note that in (c) and (d) both QD1 and QD2 play the role of the excited quantum dot.	90
B.4	Concurrence as a function of time for the coupling coefficients, $\hbar g_1 = 15$ meV and $\hbar g_2 = 30$ meV the laser-pulse fluence, 81 nJ/cm ² and various differences in energy levels ($\hbar\omega$) for each QD.	91

CHAPTER 1
INTRODUCTION

At the beginning of the 20th century, physics was changing, as great minds, such as Max Planck and Albert Einstein solved long standing problems in physics using the notion of quantization; that is, that certain quantities could only take discrete values, rather than continuous values. Though seemingly minor, this idea was revolutionary and led to the development of a whole new field of physics: quantum mechanics. The simple change from continuous to discrete has profound effects on the predictions made. These effects include the famous ‘spooky action at a distance’ that made Einstein consider the theory incomplete. Quantum mechanics has withstood the test of time; it has been verified experimentally many times and has spawned many useful devices, such as lasers and transistors.

The fundamental equation of quantum mechanics is the Schrödinger equation:

$$H\psi(t, x) = i\hbar \frac{\partial}{\partial t} \psi(t, x), \quad (1.1)$$

where H is the Hamiltonian operator, which describes the energetics of the system; i is an imaginary number; \hbar is Planck’s constant; and $\psi(t, x)$ is the wave function, which mathematically describes the quantum state of a system as a probability amplitude. Solving the Schrödinger equation involves solving for the wave function. Different systems have different Hamiltonians, which lead to radically different solutions. There are very few problems, that is, very few Hamiltonians, for which analytical solutions to the Schrödinger equation are known, such as the time-independent hydrogen atom. Much of the work in theoretical quantum mechanics during the early and mid 20th century was dedicated to coming up with clever methods and approximations to solve the harder problems. With the rise of computers in the late 20th century, physicists and quantum chemists began to develop powerful computational methods for quantum mechanics. One of the key issues that makes solving the Schrödinger equation so difficult is the dimensionality of the problem; rather than being three dimensional, like fluid mechanics, it

is $3N$ dimensional, where N is the number of electrons. Hydrogen has one electron; interesting systems have many more. Creating a grid in the $3N$ dimensional space capable of capturing the important physics would be nigh impossible for any interesting system.

Even though the problem may seem intractable, several very successful methods have been developed to allow for approximate answers, especially when solving for time-independent solutions. One of the most famous is density functional theory (DFT) [1], which scales as N^3 and has been widely used to study materials for many important applications, such as energy storage. However, in practice, DFT is an uncontrolled approximation; that is, there is no clear systematic way to systematically improve the answer. For certain problems, such as those with strong correlation (where the interaction between the electrons is important), DFT fails to give results that agree even qualitatively with experiment. DFT is capable of doing calculations on hundreds of thousands of electrons using modern day supercomputers. Quantum Monte Carlo (QMC), in particular Diffusion Monte Carlo (DMC) is another successful method for solving the Schrödinger equation, using a stochastic approach [2]. DMC also has order N^3 scaling per Monte Carlo step, but with a much larger prefactor than DFT, and can do calculations for thousands of electrons on modern day supercomputers. All variants of QMC suffer from the fermion sign problem, unless approximations are made. The sign problem is systematically improvable, at high cost, by using high order expansions in the trial wave function. One advantage of DMC as opposed to almost all other methods is that DMC works with an infinite basis set whereas other methods provide energies within a finite basis set and extrapolation to the the infinite basis set limit is very expensive. Coupled cluster, a method from quantum chemistry, is highly accurate for single reference problems, but has prohibitive N^7 scaling for

one of the most popular variants, coupled cluster singles doubles and perturbative triples (CCSD(T)) [3], limiting it to about ten atoms. CCSD(T) has an error from the truncation of the wave function, and for multi-reference systems, e.g., systems undergoing dissociation, the resulting error can be large.

At the most expensive end of the spectrum are exponentially scaling algorithms, such as density matrix renormalization group (DMRG) [4] (except in 1-dimensional systems), and full configuration interaction (FCI) [5]. With a few caveats, these exponentially scaling algorithms can give exact results, but are far too expensive for systems comprised of more than a few atoms. For many problems, DFT and especially DMC has enough accuracy to capture the important physics. There are some extremely challenging and interesting problems that require the most expensive level of theory, those that scale exponentially, to really understand what is happening in experiments. Collectively, these methods are often referred to as ‘electronic structure’ methods, and they typically solve for time-independent quantities. Solving for the dynamics of quantum systems involves a different set of methods.

Many interesting quantum phenomenon arise from the dynamics of the system. Experiments happen in real time; laser pulses excite systems which then relax, emitting light in the process. The dynamic evolution itself can lead to interesting effects that cannot be seen when solving the time-independent Schrödinger equation, especially when ‘noise’ effects which cause the system to lose energy (i.e., decoherence and decay) are included. The Schrödinger equation does not include loss terms; a different formulation of quantum mechanics must be used, which can be written as the Lindblad density matrix master equation:

$$\frac{\partial \rho}{\partial t} = -\frac{i}{\hbar}(H\rho - \rho H) + L(\rho), \quad (1.2)$$

where ρ is the density matrix, H is the Hamiltonian (like in the Schrödinger equation), and L is a Lindblad superoperator, which describes Markovian loss effects from coupling with the world outside of the system of interest. Whereas the wavefunction, ψ , can often be considered a vector of complex numbers, the density matrix, ρ , is a Hermitian matrix of complex numbers, which makes solving the Lindblad master equation much harder than solving the Schrödinger equation. Due to the increased cost and the addition of time-dependence, solving the Lindblad master equation is often not about getting high accuracy, but more about coming up with highly parameterized model systems which get the general physics correct, including cavity quantum electrodynamics (CQED) models [6] and the Jaynes-Cummings Hamiltonian [7]. These models allow the important physics to be captured without the full cost of tracking every electron in the system. Even then, the computational cost grows exponentially with system size.

Take, for example, a system of qubits. A qubit is a quantum analog of a bit – a quantum system that can take the value 0, 1, or a superposition of 0 and 1. This is often written in ‘braket’ notation, as $\alpha|0\rangle + \beta|1\rangle$. To solve for the dynamics of a modest 10 qubit system, a matrix of $2^{10} \times 2^{10}$ must be evolved according to eq. (1.2), the Lindblad master equation. 1000×1000 is doable, but expensive. To solve for the dynamics of 20 qubits, it is one million by one million, which is now a supercomputer class calculation. A qubit is the smallest quantum system in a Lindblad master equation calculation; some systems, such as a plasmonic metal nanoparticle, need 50 or more levels to describe them!

Both the time independent electronic structure systems, and the time dependent Lindbladian systems can take exponential work to obtain interesting physics. For some problems, simplifications and approximations can be made to turn the

problem from exponentially scaling to only polynomially scaling, without losing access to the interesting physics. For both the Schrödinger and Lindblad master equations, the full exponential cost should only be paid when absolutely necessary.

CHAPTER 2
PARALLELIZATION AND APPLICATIONS OF HEAT-BATH
CONFIGURATION INTERACTION

2.1 Introduction

The standard quantum chemistry Hamiltonian can be written as

$$\hat{H} = h_{\text{nuc}} + \sum_{pr} h_{rp} a_r^\dagger a_p + \frac{1}{2} \sum_{pqrs} g_{rspq} a_r^\dagger a_s^\dagger a_q a_p \quad (2.1)$$

where a_r (a_r^\dagger) is the single-particle creation (annihilation) operator and h_{rp} and g_{rspq} are integral values, typically calculated by a standard quantum chemistry program (such as MOLPRO [8] or PySCF [9]). To evaluate the energy of the system, we represent the wavefunction in the space of Slater determinants. A Slater determinant is an antisymmetrized wavefunction composed of orthonormal spin orbitals, and can be compactly represented by a bit string signifying which orbitals are occupied. For example, in bracket notation, a valid Slater determinant of two electrons in four orbitals is $|0011\rangle$. We can calculate the matrix elements between a pair of Slater determinants i and j , $H_{ij} = \langle i | \hat{H} | j \rangle$, allowing us to construct the full Hamiltonian for the set of determinants. If the states in the matrix element differ by the occupations of three or more orbitals, the matrix element is 0 (because our Hamiltonian operator \hat{H} has only upto 2-body operators).

Full configuration interaction (FCI), more commonly known as exact diagonalization in the physics literature, solves for the exact energy, within a basis, by expanding the wavefunction in the set of all possible Slater determinants. A small example is two electrons in four basis functions. The FCI wavefunction, which would give the exact answer in this small basis, would be $c_1|0011\rangle + c_2|0101\rangle + c_3|1001\rangle + c_4|0110\rangle + c_5|1010\rangle + c_6|1100\rangle$. The FCI procedure involves constructing the Hamiltonian matrix (by calculating all matrix elements, H_{ij}) representing the full Slater determinant expansion and diagonalizing that matrix. For two electrons in four orbitals, this is trivial. Interesting quantum systems

have many more than two electrons, and need many more than four basis functions to get close to the complete basis set limit, which represents the true answer. For a system with N_{\uparrow} up-spin electrons and N_{\downarrow} down-spin electrons, and a basis that consists of N_{orb} up-spin and N_{orb} down-spin orbitals, the number of determinants in the FCI wavefunction grows combinatorially with increasing electron count and increasing basis size as ${}^{N_{\text{orb}}}C_{N_{\uparrow}} \times {}^{N_{\text{orb}}}C_{N_{\downarrow}}$, making FCI practical for only very small systems. Where it is practical, though, it is extremely valuable, as it provides benchmark results on which to judge other methods with better scaling. Recently, our group has developed a new selected configuration plus perturbation theory method known as heat-bath configuration interaction (HCI), and has shown that it allows calculations of essentially the FCI energy at a tiny fraction of the cost of traditional FCI and other selected CI methods [10]. HCI creates an intelligent truncation of the FCI wavefunction, including only the most important determinants in the wavefunction. Some of the omitted determinants are included perturbatively via semistochastic second order Epstein-Nesbet perturbation theory (PT2) [11]. Though HCI is much more efficient than FCI and allows problems previously thought to be intractable to be solved, it is still an exponentially scaling algorithm, necessitating careful implementation and parallelization. Whereas FCI can be used at most for Hilbert spaces of size 10^{11} , HCI has been used for molecules with a Hilbert space of 10^{30} , and for the homogeneous electron gas with a Hilbert space of 10^{120} .

The very large number of determinants needed to achieve sufficient accuracy is in large part due the fact that the electron-electron Coulomb interaction is divergent and so there is a cusp in the wavefunction at electron-electron coincidences. The rate of convergence can be dramatically speeded up by separating the Coulomb interaction into a long-range and a short-range component and treating the short-

range part with a density functional. Although this introduces an approximation, the resulting energies are expected to be highly accurate because the density functionals are much more accurate for short-range potentials than for the Coulomb interaction. This approach provides the exciting possibility of extending HCI to larger systems than is currently possible, but will not be discussed in this thesis because this work is in its early infancy.

2.1.1 Brief Overview of Heat-bath Configuration Interaction

The HCI algorithm has been described in recent publications [10, 11]; here, only a brief overview is supplied. HCI is split into two stages: the variational part, where a truncated wavefunction comprising only the most important determinants is constructed iteratively, and the perturbative part where the most important determinants omitted from the variational wavefunction are included via second-order Epstein-Nesbet perturbation theory. Both parts of the algorithm work off of a common observation: most of the exponentially large number of Hamiltonian matrix elements come from double excitations, but the number of distinct matrix elements is only N_{orb}^4 , where N_{orb} is the number of orbitals.

We begin by presenting the criterion used in other selected configuration interaction methods for choosing determinants. They use the perturbative criterion [12]:

$$|c_a^{(1)}| = \left| \frac{\sum_i H_{ai} c_i}{E_0 - E_a} \right| \quad (2.2)$$

is sufficiently large. Here H_{ai} are matrix elements connecting states $|D_i\rangle$ within the current variational space \mathcal{V} , to states $|D_a\rangle$ outside \mathcal{V} , E_0 , is the current variational energy and $E_a = H_{aa}$.

Instead, in HCI the simpler criterion,

$$\max_{i \in \mathcal{V}} |H_{ai}c_i| > \epsilon_1. \quad (2.3)$$

is used, where, ϵ_1 is a user-defined parameter that controls the size of the final variational space [13]. This criterion is much faster because the sum in the numerator of Eq. 2.2 and the diagonal matrix element in the denominator are not needed. More importantly, one can use the observation that then the number of distinct double excitation matrix elements is only N_{orb}^4 to avoid ever looking at any of the connections that do not meet the HCI selection criterion. This is done as follows. At the very beginning of the calculation, for each pair of orbitals an ‘‘HCI array’’ is constructed that contains the indices of all pairs of orbitals that electrons in the first pair of orbitals can excite to, and the magnitude of the corresponding 2-electron integral. This array is sorted in order of decreasing magnitude of the integral. Then, when generating important determinants that are connected to determinant i , all that is necessary is to go down the HCI arrays for every pair of electrons until $|H_{ai}c_i| < \epsilon_1$ for the variational stage, or, $|H_{ai}c_i| < \epsilon_2$ for the perturbative stage, at which point one can exit the loop without ever looking at the vast majority of the determinants that don’t meet the criterion in Eq. 2.3.

One may be concerned that the choice of determinants chosen using the criterion in Eq. 2.3 is much further from optimal than that using the criterion in Eq. 2.2. This is in fact not the case because both the matrix elements H_{ai} and the wavefunction coefficients c_i vary by several orders of magnitude, so the sum in Eq. 2.2 is dominated by just a few terms, and the denominator in Eq. 2.2 is never small after one has included a sufficiently large number of determinants in the wavefunction.

Variational Stage

During any variational iteration, the wavefunction can be written as a sum over the current set of determinants, \mathcal{V} , $\psi = \sum_i^{\mathcal{V}} c_i |D_i\rangle$. From this set, new determinants which satisfy the criterion

$$\max_{i \in \mathcal{V}} |H_{ai} c_i| > \epsilon_1, \quad (2.4)$$

are added to \mathcal{V} . Here, H_{ai} is the matrix element connecting the determinant $|D_i\rangle$, which is in the current variational space, \mathcal{V} , to the determinant $|D_a\rangle$, which is a candidate determinant to be added not in \mathcal{V} . ϵ_1 is the cutoff which controls the truncation error. If $\epsilon_1 = 0$, the FCI wavefunction is recovered. The variational stage continues until the wavefunction has converged for a given ϵ_1 ; the convergence criterion we choose is either based off number of determinants (less than 0.001% new determinants were added in the last iteration) or the energy (the change in energy is less than a nanoHartree).

To begin the variational iterations, a starting determinant must be chosen. Oftentimes, this is the Hartree Fock ground state, though it does not have to be. Excited states of different symmetry groups than the Hartree Fock ground state can be calculated simply by starting in a state with that symmetry [14]. Then all determinants connected to this determinant and satisfying the HCI cutoff criterion, Eq. 2.4, are added to \mathcal{V} . The Hamiltonian for \mathcal{V} is then constructed and diagonalized, giving an updated variational energy and c_i values for the current set of determinants. The following iterations are the same: generate connections, construct the Hamiltonian, and diagonalize, and this continues until convergence. Important implementation details will be discussed later in the thesis.

Perturbative Stage

After converging the variational wavefunction, $|\psi_0\rangle$, an approximate second-order multireference Epstein-Nesbet perturbation theory is then applied to get the perturbative correction to the energy. The approximate second-order energy correction can be written as [11]

$$\Delta E_2 \approx \sum_a \frac{(\sum_i^{(\epsilon_2)} H_{ai} c_i)^2}{E_0 - E_a}, \quad (2.5)$$

where a represents a determinant outside of the variational space connected to at least one determinant in the variational space, $E_a = H_{aa}$, $\sum_i^{(\epsilon_2)}$ is a sum over only terms greater than ϵ_2 ($\epsilon_2 < \epsilon_1$), and E_0 is the variational energy from the variational wavefunction, $|\psi_0\rangle$. Similar to the variational stage, the approximate energy correction includes a sum over only terms larger than a cutoff, greatly accelerating the algorithm by ignoring terms which barely contribute to the final correction. Even with this truncation, one runs into a memory bottleneck because the sum over a involves a very large number of connected determinants and in order to have a fast algorithm one must store the partial sums for each a and square it at the end after all the contributions have been added in. Instead, a stochastic approach that samples the variational determinants is used to overcome the memory bottleneck. Doing this without introducing a bias is not completely straightforward because the average of squared quantities is not the square of the average. The unbiased stochastic method for doing this is described in [11]. A semistochastic approach [11] provides a further improvement in efficiency. An initial deterministic perturbative correction $\Delta E_2^D[\epsilon_2^d]$ is calculated using the smallest value of ϵ_2 that fits in memory, which we denote ϵ_2^d . Then, the stochastic calculation is used to evaluate the bias in the deterministic calculation (due to using an insufficiently small ϵ_2^d) by calculating the two stochastic energies $\Delta E_2(\epsilon_2)$ and $\Delta E_2(\epsilon_2^d)$ with

$\epsilon_2 < \epsilon_2^d$. The total second-order energy is given by the expression

$$\Delta E_2 = (\Delta E_2(\epsilon_2) - \Delta E_2(\epsilon_2^d)) + \Delta E_2^D(\epsilon_2^d). \quad (2.6)$$

Since $\Delta E_2(\epsilon_2)$ and $\Delta E_2(\epsilon_2^d)$ are calculated using the same set of samples, there is considerable cancellation of stochastic error. Furthermore, because these two energies are calculated simultaneously, the incremental cost of performing this calculation, compared to a fully-stochastic summation, is very small. Full details can be found in [11].

2.2 Implementation and Parallelization Details

Even though HCI greatly reduces the cost of obtaining FCI-quality energies, it is still an exponential algorithm. As such, a careful implementation, including parallelization with high parallel efficiency, is important to do calculations on interesting systems. The total number of determinants needed for an interesting system can easily exceed hundreds of millions, and we would potentially like to push to billions of determinants. The basic parallelization strategy involves assigning each determinant to a specific core, via a hash function. Each core applies the various steps of the algorithm to its local set of determinants. This gives a roughly balanced domain decomposition, as long as the hash function is balanced. It is difficult to obtain a perfect balance because even if the distribution of determinants over cores is perfectly balanced, the distribution of the connections of those determinants need not be. Here, we give an overview of the important implementation and parallelization details.

2.2.1 Variational Stage

The variational stage can be broken up into three distinct sections: generating connections (which become new determinants), generating the Hamiltonian, and diagonalizing the Hamiltonian. Generating connections takes far less time than generating or diagonalizing the Hamiltonian.

Generating Connections

Using the HCI criterion of Eq. 2.4 along with the sorted double excitations, each core loops through its local set of reference determinants, generating all connections greater than the cutoff, ϵ_1 . After generating all important connections, each core sorts the list of generated connections, removes duplicates, and then sends the connections to their owners, utilizing the hash function. After receiving the list of remotely generated connections, each core removes duplicates received from different cores, followed by removing connections which were part of its initial reference determinants, leaving each core with a list of all unique connections (spawned by all cores) which belong to it. These lists are then communicated to all other cores, and one core per node stores the global list of variational determinants in shared memory, assigning a unique global index to each determinant in an interleaved fashion. Here, interleaved means that the local lists are combined by putting the first of each list, followed by the second of each list, and so on. For example, if there were three local lists (from cores a , b , and c), each with three determinants (numbered 1, 2, and 3), the resulting list would be $[1_a, 1_b, 1_c, 2_a, 2_b, 2_c, 3_a, 3_b, 3_c]$. The interleaved structure is important for the generation of the Hamiltonian and its diagonalization, as will be described. Each core saves its list of global indices representing its local determinants. This step has a high degree of parallelism, as

each core can independently generate connections. There is communication of the local lists required, but it is a relatively small cost compared to the generation of the connections.

Generating the Hamiltonian

Once the new determinants are generated, the Hamiltonian must be calculated. Making use of the Hermiticity of the matrix, only the upper triangle of the Hamiltonian is stored, and it is stored in compressed sparse row format, saving a large amount of memory. Each core is responsible for calculating and storing the rows of the matrix corresponding to the determinants that it owns. This involves calculating matrix elements between local determinants and, potentially, all other determinants; this involves zero communication, as the list of global, unique determinants is stored after all connections have been generated. The memory required to store this global list is small compared to the memory needed to store the Hamiltonian, and it is only stored once per node. The Hamiltonian matrix elements are stored in memory once calculated; later variational stage iterations only calculate new matrix elements. The matrix elements between most of the determinants is zero, leading to a very sparse matrix. A naive algorithm for generating the matrix elements for a given determinant would involve looping over all other determinants, calculating the matrix element, and storing it, if it is nonzero. We know, due to the structure of the quantum chemistry Hamiltonian, that only determinants which differ by zero, one, or two excitations will have nonzero matrix elements. Utilizing this, one can devise more efficient algorithms that utilize “helper” arrays to skip the obviously zero elements, i.e., they avoid doing a bit string comparison to see if the determinants differ more than two excitations. Our algorithm for doing this has recently been superceded by one from Sandeep Sharma in Colorado and

Junhao Li in our group. The new algorithm is described in Appendix A.1.

The reason that the interleaved structure defined above is important for achieving good parallelism is that only the upper triangle of the Hamiltonian is stored. Each row has a different number of elements; that number decreases as the index of the row increases. For instance, in a dense $N \times N$ matrix the first row would have N elements and the last would have only 1. By interleaving the local rows in the global numbering, a good load balance is achieved. Generating the Hamiltonian requires no communication; the only bottleneck to achieving high parallelism is load balancing, which is controlled by the interleaving and hash function.

Diagonalization

Once the Hamiltonian matrix has been constructed, the next step is to diagonalize the matrix to find the desired eigenvectors and eigenvalues (collectively, eigenpairs). Only the eigenpairs corresponding to the lowest few (often just one) eigenvalue are needed, so iterative solvers can be used to greatly speed up the process. As in many quantum chemistry codes, we utilize the Davidson algorithm with diagonal preconditioning to compute the eigenpairs [15]. Davidson uses fewer iterations than other eigensolvers, such as Lanczos, but suffers from not having as high a degree of parallelism. The most work intensive part of Davidson is the matrix-vector multiply, which is done in parallel. Each core calculates its local part of the resulting vector, which is then transferred to other cores. Norms of the vectors are taken in parallel; the other parts of the Davidson algorithm (such as diagonalizing the small Krylov matrix) are done on a single core. Diagonalization takes a large percentage of the total time for the variational stage, and it gets worse as more cores are used (since it is not as parallel as generating the Hamiltonian). One way to

alleviate the cost of diagonalization is to not fully converge the Davidson algorithm at each HCI iteration. At the end of the variational stage, a final diagonalization is performed until convergence. This greatly reduces the cost of the diagonalization (by up to a factor of 4) and does not affect the final answer noticeably.

2.2.2 Perturbative Stage

The perturbative stage of the code is broken up into two sections, deterministic and stochastic. The size of the deterministic part is chosen by the available memory on the system; the stochastic part calculates the contributions that could not be stored in memory to obtain a final unbiased energy. The stochastic part allows us to get answers on any system, even if the memory is quite limited. The deterministic section's parallelization strategy is very similar to the variational stage; each core loops through its own variational determinants (the same set as in the variational stage) and hashes the generated connections (along with the numerator and denominator values from Eq. 2.5) to their true owner, where the values are summed appropriately. In contrast to the variational section, where the generated connections are only communicated after every core has generated all connections, the communication of the connections and their contributions to the energy are communicated a few times while each core goes through its local list. After each communication, each core sorts and merges its local list and the contributions to the energy in order to reduce the memory requirement. This is done only as often as needed, else the parallel efficiency will suffer.

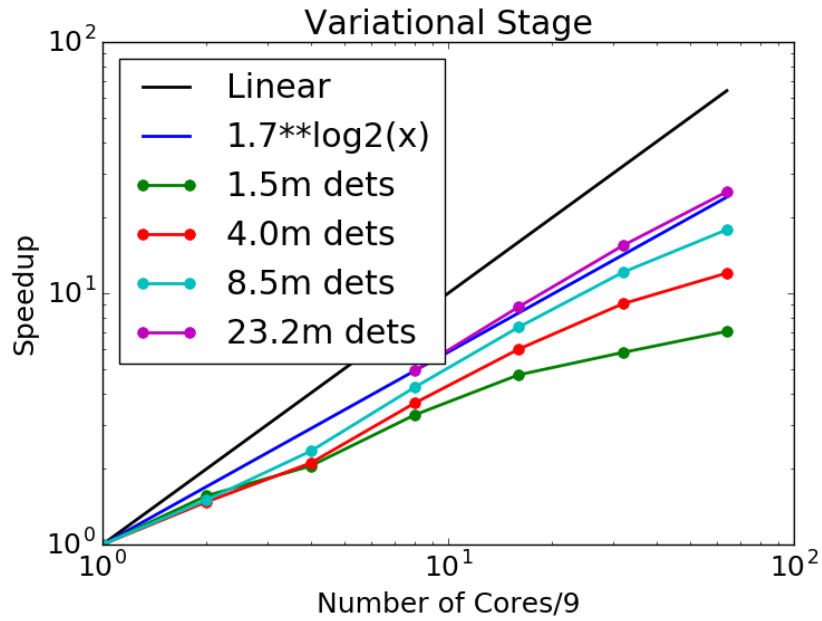
During the stochastic part, each core calculates the connections and energy contributions for a subset of a global sample of the variational determinants in Eq. 2.5. The global sample size is chosen such that all available memory is used

and is smaller (usually by a large factor) than the total number of variational determinants. Using a global sample increases the amount of necessary communication in the algorithm, but greatly reduces the statistical error of each sample (which is not generally true of generic sampling algorithms). Instead of having n_{cores} samples of a given size, it is much more efficient to have one sample that is a factor of n_{cores} larger, even after taking into account the additional communication cost.

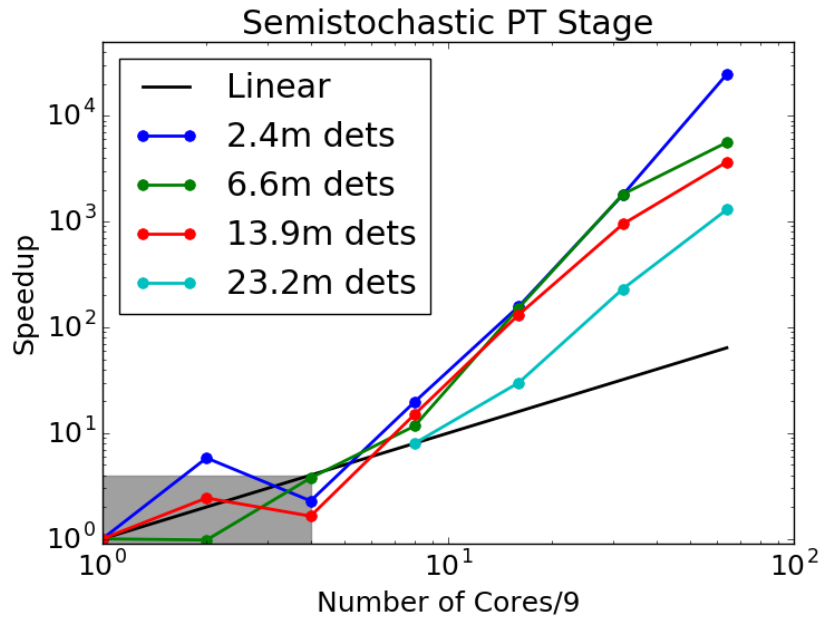
2.2.3 Performance Results

Figure 2.1a shows the parallel performance of the variational stage of our code for multiple determinant counts on a modest number of cores. All runs were done on an Intel Broadwell machine with 36 cores and 128GB of RAM per node, on Cr_2 with 12 correlated electrons and 68 basis functions. As long as there is a sufficient amount of work, doubling the number of cores decreases the runtime of the variational stage by 1.7. The 'strong scale limit' for the code is somewhere around 50000 determinants per core; for all three determinant counts, the scaling drops off around this mark. Note that the 23.2M run could not be run on a single node, due to memory constraints. For this line, the initial point assumes scaling of 1.7 for each of the first three points. For the systems we are interested in targeting (hundreds of millions to one billion determinants), this means we can run on 2000 and 20000 cores and still have good parallel efficiency.

Figure 2.1b shows the scaling of the efficiency of the perturbative stage, calculated as $1/(\epsilon^2 t)$, where ϵ is the stochastic error and t is the total run time of the perturbative stage (including both stochastic and deterministic parts). (The statistical error decreases as $N_s^{-\frac{1}{2}}$ as N_s , the number of samples, is increased.) The shaded area of the graph represents on-node parallelism; that is, increasing



(a) Variational stage parallel efficiency.



(b) Perturbative stage parallel efficiency.

Figure 2.1: HCI parallel efficiency. The variational stage sees a gain of roughly $1.7\times$ when doubling the number of cores. The perturbative stage benefits from both core count and increased memory; increasing the number of nodes increases the memory and leads to superlinear scaling.

the number of cores on one node. This only increases computational power, but does not increase available memory. In this region, the scaling is not consistent; memory contention among the cores is likely to blame, though more investigation is warranted. When additional nodes are added, the available memory increases. This increases the size of the deterministic space and the size of the stochastic sample, leading to a superlinear speedup. The superlinear speedup continues until the whole space is calculated completely deterministically; after that, the speedup would be sublinear, with the communication of the generated connections being the main bottleneck. For large systems, the number of connected determinants is sufficiently large that the perturbative correction cannot be computed with the purely deterministic algorithm. Then the stochastic part of the algorithm is necessary and superlinear scaling provides an efficient use of parallel resources.

2.3 Applications

2.3.1 Benchmarking Other Methods

As an exponentially scaling algorithm, HCI will eventually run out of steam for large, interesting physical systems, such as solids. It can still be useful for these systems by providing a benchmark to measure the error of other, cheaper methods, and in some cases give confidence that using the approximations made in the other methods sufficiently accurate. We applied HCI to a simple four-atom unit cell of silicon with periodic boundary conditions, comprised of 16 valence electrons in 52 basis functions. After obtaining the essentially exact answers within this basis from HCI, We then compared the results to other quantum chemistry methods,

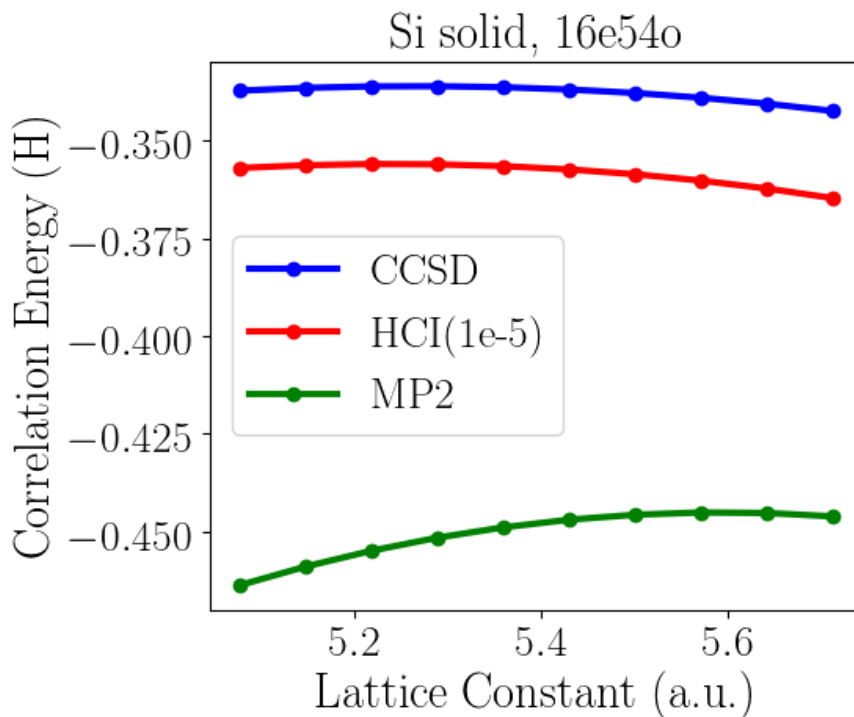


Figure 2.2: Benchmarking quantum chemistry methods using HCI. The HCI curve represents the essentially exact answer; CCSD has a nearly constant error for the different volumes, whereas MP2’s error varies for the different systems.

including second order Moller-Plesset perturbation theory (MP2) and CCSD. The results are plotted in figure 2.2. The HCI results can be considered essentially exact; CCSD and MP2 are approximate. MP2 greatly underestimates the energy (over 100 milliHartree in some places), and the error is different for the different volumes studied. CCSD has a nearly constant error of 20 milliHartree across the different volumes. Though the absolute energies are wrong, the relative energies for the different geometries are good. It is important to understand how the faster, more approximate methods behave so that they can be applied with confidence. In this case, we can claim that CCSD would do well for relative energies, but not for absolute energies. MP2, however, would be poor for both absolute and relative energies. CCSD, with its polynomial scaling could certainly do much larger systems than HCI could. Benchmarking with HCI for these smaller systems gives a good

understanding of the range of applicability and the limits of the better scaling methods.

2.3.2 Chromium Dimer

A prototypical example of a small but computationally challenging molecule is the chromium dimer, whose ground-state potential energy curve is a great challenge to compute with state-of-the-art quantum chemistry methods. Its formal sextuple bond with weak binding energy, short equilibrium length, and an unusual extended “shoulder” region as it is dissociated contribute to the difficulty. It is highly multi-configurational, owing to its sextuple bond, with many configurations required to correctly dissociate the molecule into two high-spin atoms. It exhibits differential electron correlation effects, scalar relativistic effects, and the importance of semi-core valence electron correlation [16]. Due to its complex electronic structure, the chromium dimer has long been the quintessential proving ground for many-body algorithms in quantum chemistry [16–26].

Both static and dynamic correlation are required for an accurate theoretical treatment. Algorithms that address only one of the two, such as Complete Active Space Self-Consistent Field (CASSCF) with 12 electrons in 12 orbitals, and coupled-cluster theory, which only addresses the dynamical correlation, fail to correctly describe the experimental potential energy curve [27]. The experimental potential energy curve itself has an uncertainty of about 0.1 eV.

To date, two of the most accurate algorithms for treating the chromium dimer have been Auxiliary Field Quantum Monte Carlo (AFQMC) [25], and a Density Matrix Renormalization Group Self-Consistent CAS reference (12 electrons

in 22 orbitals) combined with N-electron Valence Perturbation Theory (DMRG-SC-NEVPT2) [26], to put in the dynamical correlation coming not only from the high-lying orbitals but also that from the semi-core states. However, both of these methods have serious drawbacks. In the case of AFQMC, the error bars are large and there is a phaseless approximation. The shoulder region of the resulting potential energy curve is qualitatively too deep, when comparing to the experimental values. With DMRG-SC-NEVPT2, the results depend sensitively on the choice of the CAS space and the precise form of the second-order perturbation theory. Reasonable agreement with the experimental potential energy curve is obtained using the above mentioned carefully chosen active space and perturbation theory after extrapolating to the Complete Basis Set (CBS) limit.

We performed calculations at various points along the Cr_2 potential energy surface using HCI. Scalar relativistic effects were included using the second-order Douglas-Kroll-Hess Hamiltonian. We used Dunning’s double zeta basis sets [28] modified to be appropriate for Douglas-Kroll-Hess calculations, cc-pVDZ-DK.

Calculations with frozen argon cores (12 valence electrons) and with frozen neon cores (28 valence electrons) were performed. As a starting point for both calculations, a CASSCF(12e, 12o) calculation was performed, and the resulting core orbitals were frozen (either Ar cores or Ne cores). After freezing the cores, natural orbitals were obtained using a short HCI run. The one- and two-body integrals were then transformed to this natural orbital basis in order to accelerate convergence of the subsequent HCI calculations to the Full CI limit. All electron integrals were computed using the Molpro quantum chemistry package [29].

Extrapolation to the Full CI limit was performed by fitting a quadratic function of ΔE_2 to the HCI total energy calculations and extrapolating to $\Delta E_2 = 0$.

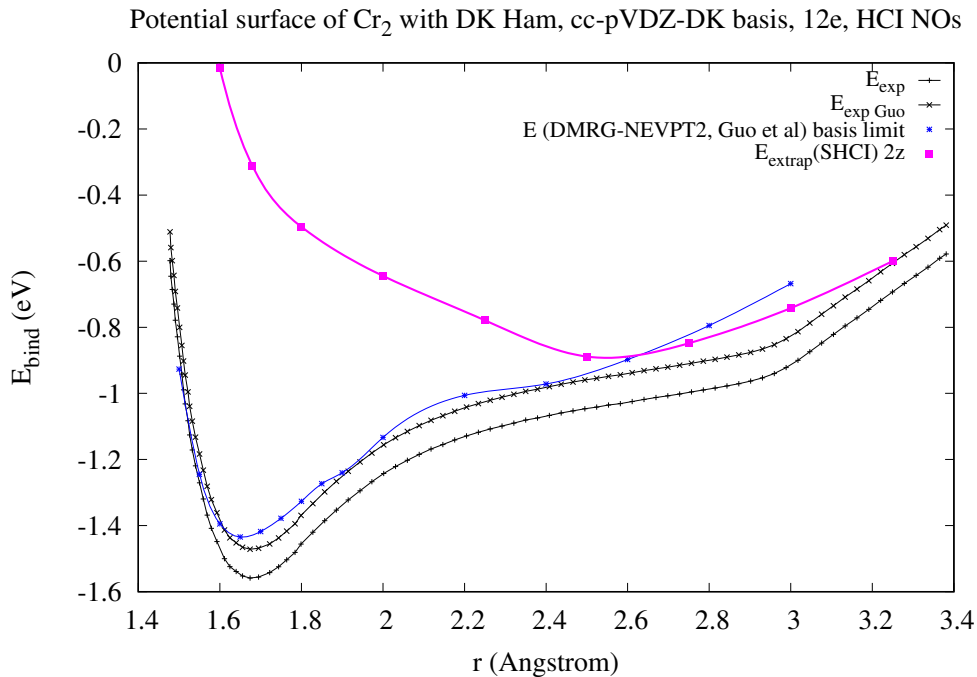


Figure 2.3: HCI calculations and experimental results for Cr₂ in the cc-pVDZ-DK basis set, correlating 12 electrons. E_{bind} represents the binding energy. The HCI curve is qualitatively very far off from the DMRG-NEVPT2 and experimental curves. The two experimental curves differ by about 0.1 eV, reflecting the uncertainty in the experimental dissociation energy.

Frozen Ar core

The Argon-core calculations (12e, 68o) are shown in Fig. 2.3. Although this yields a bound molecule, the binding curve is qualitatively very far from the experimental curve and the DMRG-NEVPT2 curve of [26]. Despite Cr₂'s formal sextuple bond, six electron pairs are not enough to qualitatively characterize the bond in our theoretical calculations, as shown in figure 2.3. Even with more complete basis sets, the curve is still qualitatively wrong; previous calculations at the equilibrium geometry are nowhere near the energies of DMRG-NEVPT2 or experiment [10].

Frozen Ne core

The Neon-core calculations (28e, 76o) are shown in Fig. 2.4. Now, with the inclusion of the semi-core excitations, the binding curve looks qualitatively correct, with a well of nearly the correct depth at nearly the correct geometry, and a “shoulder” structure, as found experimentally. The difference between the frozen Ar core and the frozen Ne core is striking; the former looks nothing like the experimental curve, while the latter is qualitatively correct. Both of these calculations are in the same basis, differing only by the inclusion of the semi-core excitations. There is some error in our computed curve coming from the extrapolation to $\epsilon_1 \rightarrow 0$. Improvements to our algorithm that are currently under way, will allow us to make this error yet smaller. The main reasons for the remaining difference between our curve and experiment are probably basis set incompleteness error and experimental uncertainty. Other contributing factors are higher-order relativistic effects beyond those treated perturbatively by the second-order Douglas-Kroll-Hess Hamiltonian, and the correlation effects of the remaining core electrons, but all of these are likely small. Even with the remaining differences, our calculations will provide essentially exact results for the frozen Ne core, cc-pVDZ-DK basis set energies and can be used to estimate the error in other state-of-the-art methods.

2.4 Conclusion

Heat bath configuration interaction represents a pathway to nearly exact answers of small, interesting systems where other, cheaper methods fail, as well as a way to understand the errors inherent in the other methods. It can still require a large amount of computational power to obtain converged results, though orders

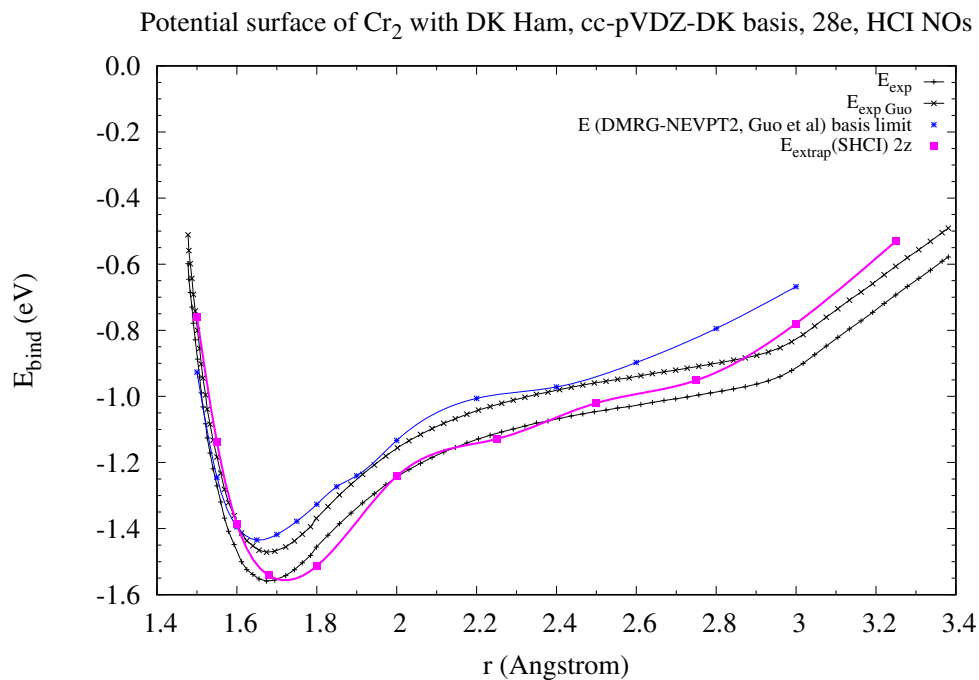


Figure 2.4: HCI calculations and experimental results for Cr_2 in the cc-pVDZ-DK basis set, correlating 28 electrons. E_{bind} represents the binding energy. The HCI curve agrees qualitatively very well with the DMRG-NEVPT2 and experimental curves. The two experimental curves differ by about 0.1 eV, reflecting the uncertainty in the experimental dissociation energy.

of magnitude less than other competing methods. It seems likely that the method can be extended to somewhat larger systems at the price of introducing a small error. One promising approach for doing this is to combine it with a short-range density functional approach, which is expected to be far more accurate than than the usual Kohn-Sham density functional theory.

CHAPTER 3
ENTANGLEMENT OF TWO, THREE, OR FOUR
PLASMONICALLY COUPLED QUANTUM DOTS

Reprinted with permission from M. Otten, R. A. Shah, N. F. Sherer, M. Min, M. Pelton, and S. K. Gray. Entanglement of two, three, or four plasmonically coupled quantum dots. *Phys. Rev. B*, vol. 92, p. 125432, 2015 [30]. Copyright 2015 by the American Physical Society.

3.1 Introduction

Plasmonic nanostructures provide the potential for extremely strong light-matter interactions because of their ability to concentrate optical fields to nanometer-scale dimensions [31]. Such strong interactions could enable the manipulation of quantum states in materials that interact with the confined fields [32–34]. However, plasmon resonances are necessarily associated with strong dissipation, raising the question of whether quantum effects are compatible with such rapid loss of energy and coherence.

On the other hand, it has been realized that controlled interactions between quantum objects and a dissipative environment can lead to the production of stable entangled states [35–37]. Several theoretical studies applied this concept of dissipation-induced entanglement to problems of QDs interacting with plasmonic systems [38–43]. These studies show that effective interactions between pairs of two-level quantum dots (QDs), mediated by dissipative plasmon resonances in metal nanoparticles or waveguides [44], can produce entanglement between QDs, analogous to previous proposals to entangle interacting atoms through common coupling to a lossy cavity [45]. The QDs’ entanglement arises spontaneously due to common coupling to the plasmonic nanostructures, without requiring postselective measurements or “engineering” of the dissipative environment. Since entanglement is a uniquely quantum property that is at the heart of quantum information and computation, this illustrates in principle the potential for true “quantum plasmonics” [46]. Such QD-plasmonic systems are also of relevance because they represent nanoscale structures that do not require atom traps or cryogenic temperatures to operate and can be integrated with other nanophotonic components.

Despite their potential for displaying quantum plasmonics effects, previous pre-

dictions of plasmon-induced entanglement in QDs have been limited to systems of only two QDs, and one of the QDs was required to be initially prepared in its excited state. For systems of two QDs, this can, in principle, be done using single-photon pulses [47], but scaling these schemes up to larger numbers of QDs would require the ability to individually access and control the state of each QD.

In this paper, we propose a system where control over the interaction between objects to be entangled (QDs) and the dissipative environment (plasmonic system) is determined by the nanoscale geometry of the system, and the only external input required is a single, ultrafast laser pulse. Moreover, we show that the method can be scaled to multiple QDs, and thus has the potential to serve as a key resource for quantum information processing at the nanoscale [48, 49].

3.2 Theoretical Methods

Our treatment, detailed in the Supporting Materials, Appendix B, generalizes work on one QD interacting with a plasmonic system [50]. The underlying system basis states are $|q_{N_D}, \dots, q_1\rangle |s\rangle$, where $q_i \in \{0, 1\}$ indexes the exciton in QD i ; i ranges from 1 to N_D (the number of QDs) and s indexes plasmon energy levels. Lowering and raising operator pairs for the QDs and plasmon are $(\hat{\sigma}_i, \hat{\sigma}_i^\dagger)$, and $(\hat{b}, \hat{b}^\dagger)$, respectively. The dipole operators are $\hat{\mu}_i = d_i(\hat{\sigma}_i + \hat{\sigma}_i^\dagger)$, and $\hat{\mu}_s = d_s(\hat{b} + \hat{b}^\dagger)$, where d_i , and d_s denote transition dipole moments of the QDs and plasmon, respectively. The density matrix, $\hat{\rho}(t)$, satisfies:

$$\frac{d\hat{\rho}}{dt} = -\frac{i}{\hbar}[\hat{H}, \hat{\rho}] + L(\hat{\rho}), \quad (3.1)$$

in which \hat{H} is the Hamiltonian for the driven coupled system and $L(\hat{\rho})$ is a Lindblad superoperator providing dephasing and dissipation. More explicitly,

$$\hat{H} = \sum_i \hat{H}_i + \hat{H}_s + \hat{H}_d + \sum_i \hat{H}_{s,i}, \quad (3.2)$$

where $\hat{H}_i = \hbar\omega_i\hat{\sigma}_i^\dagger\hat{\sigma}_i$ are uncoupled exciton Hamiltonian operators, $\hat{H}_s = \hbar\omega_s\hat{b}^\dagger\hat{b}$ is the uncoupled plasmon Hamiltonian, and $\hat{H}_d = -E(t)\hat{\mu}$ is coupling to an applied electric field, $E(t)$. Each QD couples with the plasmon via $\hat{H}_{s,i} = -\hbar g_i(\hat{\sigma}_i^\dagger\hat{b} + \hat{\sigma}_i\hat{b}^\dagger)$. We assume that the distance between QDs is large compared to the separation between QDs and neighboring metal nanoparticles, so that direct through-space coupling among QDs can be neglected. We neglect retardation, which means that our treatment is limited to systems with dimensions small compared to the optical wavelengths. The Supporting Materials discuss the level structure of $\hat{H} - \hat{H}_d$, which provides additional insight into the nature of the problem.

We employ an extension of $L(\hat{\rho})$ that was previously used [50], parameterized by QD population (or spontaneous emission) and environmental dephasing decay constants, γ_{pi} and γ_{di} , and plasmon decay constant γ_s . We consider time scales on the order of the inverse of these decay rates, so that there are no correlated fluctuations in the QD states, and the use of the Lindblad formalism is justified. Although environmental dephasing is explicitly included for the QDs, it is not necessary to do so for the plasmon because the dephasing that arises from its decay, and that is encoded in the corresponding term in $L(\hat{\rho})$, is much larger in magnitude. As in Ref. [50], the rotating wave approximation is applied. We use an efficient solver, based on sparse matrix-matrix multiplication algorithms along with both Runge-Kutta and exponential time integration schemes [51, 52].

The base parameter choices for the model outlined above are similar to those originally used in a single plasmonic-QD system study [50] and correspond to a

gold nanoparticle system interacting with QDs in a polymer matrix. Specifically, for all i , $\hbar\omega_i = \hbar\omega_s = 2.05$ eV; $\mu_i = 13$ D, $\mu_s = 4000$ D; $\hbar\gamma_{pi} = 190$ neV, $\hbar\gamma_{di} = 2$ meV, $\hbar\gamma_s = 0.15$ eV. We assume the system is embedded in a dielectric medium of $\epsilon_{med} = 2.25$, typical of a polymer.

Electrodynamic simulations give a realistic estimate for the plasmon-QD coupling factor of $\hbar g_i \approx 10$ meV for a system of two ellipsoidal gold nanoparticles, each of length 30 nm and width 20 nm, and with a 6 nm gap between them and a QD centered in the gap [50]. Larger coupling factors could be obtained for silver nanoparticles as compared to gold [53], for particles with larger aspect ratios or different shapes, or for smaller gaps. While such systems will exhibit different resonance frequency, linewidth, and dipole moments of the plasmon resonances, we keep those and all other parameters constant in the present calculations in order to isolate the effect of changing only the coupling constants. Calculations have been performed for coupling constants $\hbar g_i$ from 5 meV to 45 meV.

3.3 Results

3.3.1 Entanglement in the dark

We begin by exploring a situation similar in spirit to that reported in Refs. [38,40]: one of the quantum dots (labeled “QD1”) is initially in its excited state, all others are initially in their ground states, and there is no applied electromagnetic field. Unlike the previous results, however, we also consider systems with more than two QDs coupled to the plasmonic system. We quantify the degree of entanglement as a function of time using Wootters’ concurrence [54] (see also Supporting Materials,

Appendix B). Results are presented in Figs. 3.1(b)–(d). For the two-QD case, as previously reported [38–40], the concurrence reaches a value of 0.45 as the system evolves. The emergence of entanglement can be understood by considering the symmetric and antisymmetric QD states,

$$|S\rangle = \frac{1}{\sqrt{2}}(|q_2 = 1, q_1 = 0\rangle + |q_2 = 0, q_1 = 1\rangle) \quad (3.3)$$

and

$$|A\rangle = \frac{1}{\sqrt{2}}(|q_2 = 1, q_1 = 0\rangle - |q_2 = 0, q_1 = 1\rangle) \quad , \quad (3.4)$$

and their associated expectation values, or populations, $P_S(t)$ and $P_A(t)$, also displayed as a function of time in Fig. 1(b). The initial state, with only QD1 excited, corresponds to $P_S = P_A = 0.5$. The symmetric state, analogous to a bright singlet state, decays more rapidly than the antisymmetric state [39], analogous to a dark triplet state. After a certain time, the population of the antisymmetric state is much larger than the population of the symmetric state, and the entanglement reaches a maximum. The results shown in Fig. 1 correspond to $\hbar g_i = 30$ meV. However, we find that entanglement, with a maximum concurrence of 0.2, can occur even for $\hbar g_i = 10$ meV (Supporting Materials). In practice the QDs may not have exactly the same energy, which could diminish the entanglement effects. However, the Supporting Materials also show that, for QDs with transition energies varying within the 2 meV dephasing width, the entanglement effects remain.

In the cases of three and four QDs, bipartite concurrence can occur between QDs that are *not* initially excited, i.e., the concurrence between QD2 and QD3, denoted 2:3, in the three-QD case (Fig. 3.1(c)) and the 4:3, 4:2, 3:2 concurrences of the four-QD case (Fig. 3.1(d)). Both the three-QD and four-QD cases show degeneracies in the bipartite concurrence, as the system is completely symmetric

except for the one initially excited QD. All bipartite concurrences that include the initially excited QD (QD1) have a much larger peak than do the bipartite concurrences that exclude the initially excited QD.

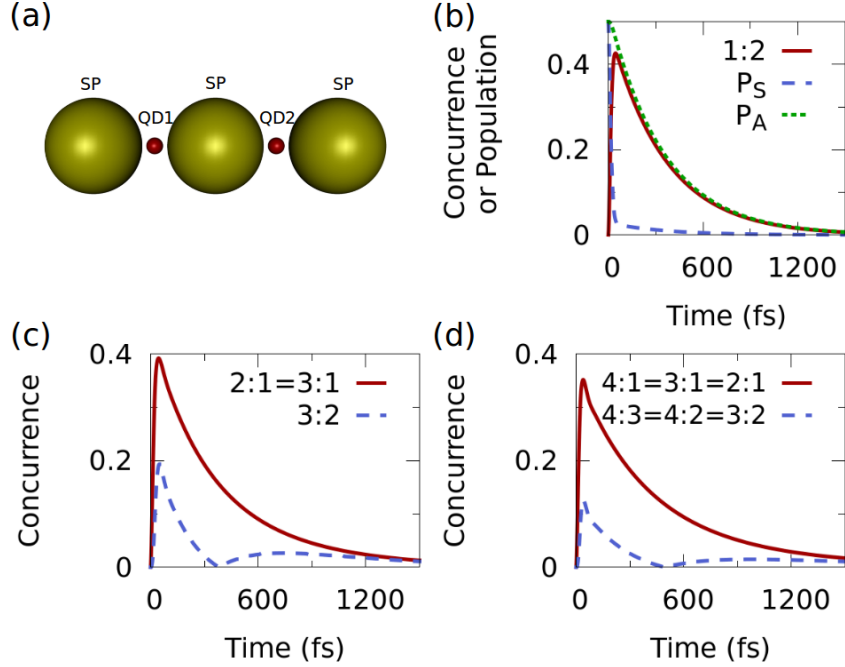


Figure 3.1: (a) Diagram of a plasmonic-two-QD system composed of three metal nanoparticles (the plasmonic system, labeled ‘SP’) with QDs (labeled ‘QD1’ and ‘QD2’) in the interparticle gaps. Bipartite concurrence of two (b), three (c), and four (d) QD systems where one of the QDs (QD1) is initially excited, with $\hbar g_i = 30$ meV in all cases. $i:j$ refers to the concurrence between QD i and QD j . Part (b) also shows the population of the symmetric state $|S\rangle$, P_S , and of the antisymmetric state $|A\rangle$, P_A .

3.3.2 Entanglement with optical pulses

So far, we have imagined that exactly one of the QDs could somehow be initially prepared in its excited state, and allowed the system to evolve from that initial state in order to generate entanglement. A more experimentally relevant situation would involve the entire plasmon-QD system starting in its ground state and

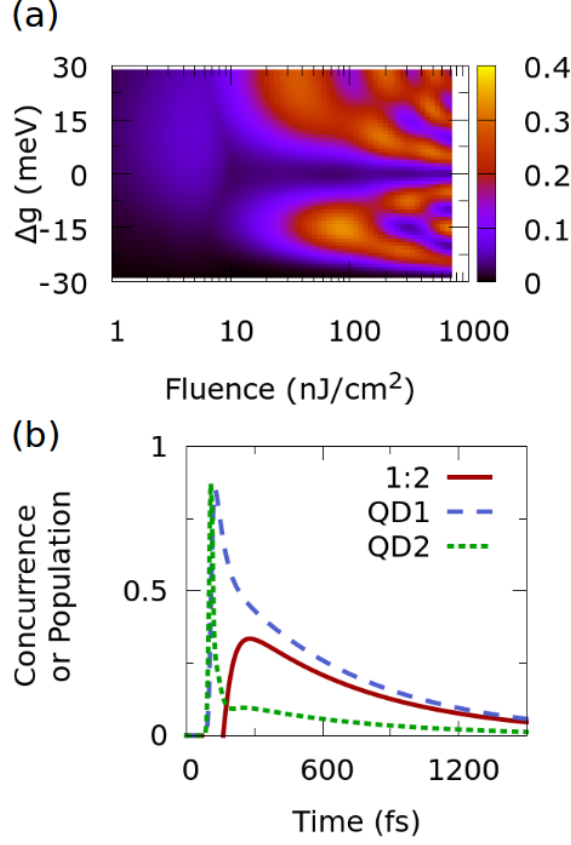


Figure 3.2: Maximum concurrence when a plasmon-two-QD system initially in its ground state is exposed to a 20-fs laser pulse. (a) Concurrence as a function of laser-pulse fluence and plasmon-QD coupling coefficient for one of the QDs ($g_1 = g_2 + \Delta g$) relative to the other ($\hbar g_2 = 30$ meV). (b) Concurrence as a function of time, for coupling coefficients $\hbar g_1 = 15$ meV ($\Delta g = -15$ meV) and $\hbar g_2 = 30$ meV, and laser-pulse fluence 81 nJ/cm², that produce the largest concurrence. The populations of QD1 and QD2 are also plotted.

being exposed to a short laser pulse. To simulate this situation, we take $E(t) = G(t)E_0 \cos(\omega_0 t)$. The carrier frequency, ω_0 , is taken to be on resonance with the QD transitions and the plasmon resonance: $\hbar\omega_0 = 2.05$ eV. The pulse envelope function, $G(t)$ is taken to be a Gaussian function with full-width at half-maximum of 20 fs, and E_0 is adjusted to achieve the desired fluence. Figure 3.2(a) displays the maximum concurrence that results in this case, as a function of pulse fluence (i.e., time integral of $\sqrt{\epsilon_{med}} c \epsilon_0 E^2(t)$) and plasmon-QD coupling constant for one

of the QDs ($g_1 = g_2 + \Delta g$) relative to the other ($\hbar g_1 = 30$ meV). Significant parameter regions exist where the concurrence is comparable to that obtained in the dark case of Fig. 3.1. We should note that laser fluences up to 1000 nJ/cm² are both experimentally accessible and reasonable in the sense that they should not lead to sample degradation.

High concurrence occurs only when there is an asymmetry in the couplings of the QDs to the plasmonic system. This asymmetry could be achieved in practice by fabricating a system where the two QDs are at different distances from the metal nanoparticles. The asymmetry can allow one QD to be significantly more excited than the other QD by the end of the laser pulse. As a result the laser pulse then creates a QD state similar to the $|q_2 = 0, q_1 = 1\rangle$ state that was the starting point of the dark case that, as we have seen, led to a rise in concurrence. The largest concurrence for the pulsed two-QD system, ≈ 0.35 , is obtained for $\hbar g_1 = 15$ meV and $\hbar g_2 = 30$ meV. The dynamics of the concurrence and QD populations for this case are shown in Fig. 3.2(b). One might expect that this combination of coupling coefficients would lead to larger initial population for QD2, since it is more strongly coupled to the plasmonic system. However, the population of QD2 spikes and decays rapidly as the incident laser pulse passes through the system, while the population of QD1 rises and decays more slowly. The result is that there is eventually larger population for QD1 than QD2. This somewhat counterintuitive result, which appears to be quite general, is a consequence of the Purcell effect [50]: while the QD with the larger coupling coefficient experiences a larger local field, leading to a fast initial rise in its excited-state population, its emission rate is also increased (to $\gamma_{pi} + 4g_i^2/\gamma_s \approx 4g_i^2/\gamma_s$), leading to rapid depopulation. The QD with the smaller coupling coefficient undergoes a delayed but more sustained partial Rabi oscillation, leading to its larger initial population.

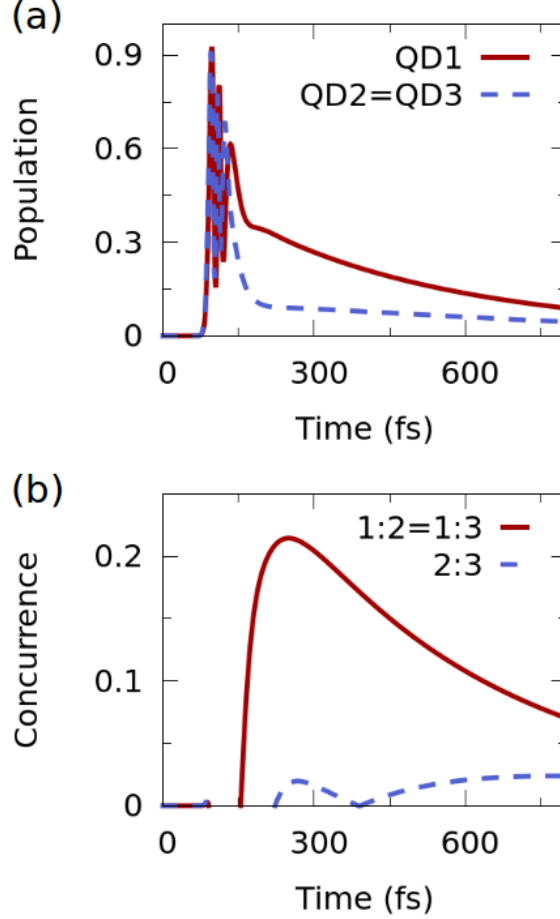


Figure 3.3: Results for a plasmon-three-QD system with laser-pulse fluence of 500 nJ/cm², and coupling coefficients $\hbar g_1 = 30$ meV and $\hbar g_2 = \hbar g_3 = 35$ meV. (a) Excited-state populations for the three QDs. (b) Bipartite concurrences.

An extensive optimization such as the one we carried out for the plasmon-two-QD system is computationally challenging for larger systems. We therefore selectively examine portions of the parameter space in the three-QD case. Figure 3.3 depicts promising results. They are similar in spirit to the optimal two-QD result, with only one QD having a coupling different from that of the other two: $\hbar g_1 = 30$ meV, and $\hbar g_2 = \hbar g_3 = 35$ meV. Figure 3.3 depicts the time evolution of the populations of the three QDs and of the bipartite concurrences. Having one QD less strongly coupled to the plasmonic system than the others allows the populations to grow and decay at different rates, so that an initial state is created with

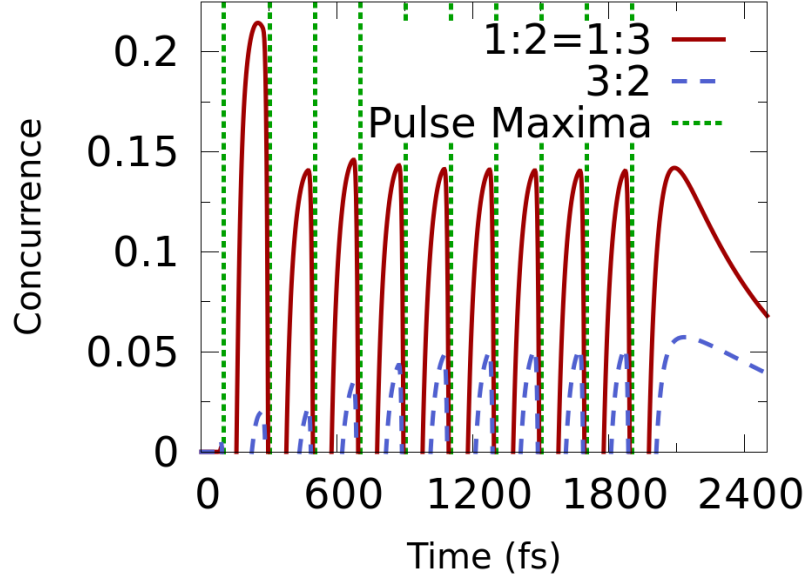


Figure 3.4: Concurrences for a plasmon-three-QD system with a repeating 500 nJ/cm² pulse. Coupling coefficients are $\hbar g_1 = 30$ meV, $\hbar g_2 = \hbar g_3 = 35$ meV. The dotted vertical lines represent the times associated with the maxima of the pulses.

larger population in the excited state of QD1 than of QD2 or QD3. Oscillations are seen in the population of QD1 over the duration of the laser pulse, and rapid decay of the populations of QD2 and QD3 are seen due to their larger Purcell factors. Significant but smaller concurrences are found in other pulsed two-QD and three-QD systems with much smaller coupling constants, g_i , and somewhat larger fluences (see Appendix B). Initial studies of analogous pulsed four-QD systems also indicate that such systems can be driven into entangled states, although to a degree lesser, for comparable parameters, than the two-QD and three-QD cases. In general, a more thorough investigation of the parameter space, varying other parameters such as the dephasing and decay rates, could lead to larger concurrences.

In all cases, large concurrence is achieved for only a brief period after the laser pulse has excited the system, before the population of the entangled state decays.

However, entanglement can be restored to the system by applying a repeated series of pulses, as shown for a plasmon-three-QD system in Figure 3.4. Each incoming pulse initially destroys the entanglement and reduces concurrence to zero, because both $|A\rangle$ and $|S\rangle$ are excited. However, $|S\rangle$ decays quickly, and concurrence rapidly grows back to its peak value. For the concurrence between the pairs of inequivalent QDs, this peak value is somewhat smaller than the maximum value reached for a single pulse, but the peak concurrence between the two equivalent QDs is much larger than the single-pulse case. Continuous-wave excitation of the system could not induce a high degree of entanglement, as it would continually excite both the $|A\rangle$ and $|S\rangle$ states; to be entangled, the population of $|A\rangle$ needs to be large while the population of $|S\rangle$ is small.

Fabricating coupled plasmon-QD systems is a significant challenge. Our scheme requires the ability to assemble metal nanoparticles and QDs with nanometer-scale control over each interparticle separation. Nonetheless, rapid improvements in nanofabrication [55] and chemically-driven nanoparticle assembly [56–59] may make it feasible in the near future. DNA self-assembly methods have recently been used, for example, to fabricate colloidal gold nanoparticles with numerous QDs surrounding them [60], and strong plasmon-emitter coupling has been experimentally demonstrated in other systems [61].

Once a system is fabricated, there is the challenge of demonstrating entanglement. It has recently been proposed that nanoparticle plasmons could be entangled by excitation with entangled photons, and the plasmonic entanglement read out through the characteristics of the radiated far field [62]. It may be possible to use a similar scheme in our case: plasmons would be entangled through their coupling to entangled QDs, serving as a interface between the QD states and the radiated

field.

3.4 Concluding Remarks

In summary, we propose a scheme involving exposure to a single or repeated optical pulses, that makes it possible to create and maintain entanglement between all pairs of QDs when two, three, or four closely spaced QDs are coupled to a common plasmonic nanostructure. This contrasts with previous schemes based on plasmonic waveguides, which can entangle spatially separated dots, but which are limited to two QDs. Moreover, in our scheme, the entire system begins in its ground state and is excited by a common laser pulse or series of pulses. Tuning the degree of coupling between each QD and the plasmonic nanostructure enables generation of an excited state that evolves spontaneously, driven by dissipation of the plasmons, towards an entangled state. Entanglement is achieved without the need for the QDs to be individually addressable, and without the need for controlled quantum gates.

There are a number of considerations for achieving good concurrences. First, in general, it appears that larger magnitude QD-plasmon couplings, g_i are advantageous; here, we have restricted consideration to coupling strengths that may be achievable in practice. As noted above, engineering a system with one QD more weakly coupled to the plasmon than the others can be effective, i.e. if that QD is labeled “1” then $g_1 < g_2, g_3$, etc. For the concurrences to be maintained for appreciable lengths of time beyond the pulse, the dephasing rates should be small in comparison to the Purcell decay rates, $\gamma_{di} < 4g_i^2/\gamma_s$. Future work will involve more extensive parameter searches to discover optimal conditions than those currently

found for the cases with three and more QDs coupled to a plasmonic system, as well as consideration of more sophisticated pulse shapes and sequences. Finally, we should note that the present paper focused on achieving bipartite concurrences among systems with two and more QDs. Future work will be devoted to exploration of the possibility of generating maximally entangled multi-qubit states, including what are termed GHZ and W states for three qubits [49, 63].

CHAPTER 4
ORIGINS AND OPTIMIZATION OF ENTANGLEMENT IN
PLASMONICALLY COUPLED QUANTUM DOTS

Reprinted with permission from M. Otten, J. Larson, M. Min, S. M. Wild, M. Pelton, and S. K. Gray. Origins and optimization of entanglement in plasmonically coupled quantum dots. *Phys. Rev. A*, vol. 94, no. 2, p. 022312, 2016 [64]. Copyright 2016 by the American Physical Society.

4.1 Introduction

Hybrid systems composed of plasmonic nanostructures and quantum emitters/absorbers (e.g., semiconductor quantum dots or other gain media) are currently of much interest. This is due to the plasmonic element's ability to interact strongly with light, leading to subwavelength control and confinement, and the possibility of the quantum element introducing nonlinear optical (as well as more general quantum) responses that may be enhanced by its proximity to the plasmonic element. For example, theoretical predictions of certain Fano resonance phenomena [50,65,66] in such systems exist, and experiments are approaching the ability to measure such features [67] and have already demonstrated novel lasing action [68] and quantum coherences [69]. The studies of such hybrid systems can also be viewed as steps in the emerging field of “quantum plasmonics,” [46,62,70] which aims to realize quantum-controlled devices relevant to quantum sensing, single-photon sources, and nanoscale electronics.

Features relevant to quantum information, such as the entanglement among the quantum dots (QDs), can also be achieved in hybrid plasmonic/QD systems. This ability may seem surprising given the dissipative (or lossy) aspect of plasmonic structures. However, interactions between quantum objects and a dissipative environment lead to the production of stable entangled states [35–37]. Several pioneering theoretical studies have shown that dissipation-induced entanglement is relevant to systems of QDs interacting with plasmonic nanostructures [38–44].

We previously explored methods for generating entanglement in QD-plasmon systems, using both systems in which only one QD is initially prepared in its excited state and the system evolves without external excitation and systems in which all the QDs are initially in their ground states and the entire system is excited by an

ultrafast laser pulse [30]. This latter work, as well as the present work, models the QDs as two-level systems with occupation of the (electronically) excited state being the relevant degree of freedom. (The QD parameters are chosen to be consistent with CdSe nanocrystals as discussed in greater detail in earlier work on single QD/plasmon interactions. [50, 53]) Reference [30] showed that either a single or repeated optical pulse entangled the QDs and that the amount of entanglement can be tuned by controlling the coupling of the QDs to the plasmonic nanostructure. Furthermore, the whole system can be excited with a single pulse, without the need to individually address each subsystem. That work and the present work allow for asymmetric coupling of the QDs to the plasmonic system; for example, one can imagine the QDs to be configured to be at different distances from the plasmonic system or in some other way that can lead to asymmetry.

To allow dissipation-induced entanglement to be an effective candidate for quantum information applications, one must thoroughly understand how the entanglement is generated. Furthermore, constraining parameter sets in experimentally viable regions of the parameter space and knowing the sets' associated degrees of entanglement are important for engineering such systems within any larger quantum information platform. In this paper, we seek to determine system features that maximize the degree of entanglement between the QDs. To accomplish this objective, we employ analysis based on solutions of limiting forms of the problem and optimization based on numerical solutions to the complete cavity quantum electrodynamics equations. We show that for any number of QDs, simple initial conditions and parameter guidelines generate systems where all pairs of QDs share some degree of entanglement.

4.2 Theoretical Methods

We consider a cavity quantum electrodynamics (CQED) model of a system of N quantum dots in proximity to a plasmonic system. The underlying system's basis states are

$$|q_N, q_{N-1}, \dots, q_1; s\rangle = |q_N\rangle |q_{N-1}\rangle \dots |q_1\rangle |s\rangle, \quad (4.1)$$

where $q_i \in \{0, 1\}$ represents the exciton of the i th QD and $s \in \{0, 1, 2, \dots, N_s\}$ represents the plasmon energy levels. Using a simplified notation $q = q_N, \dots, q_1$, we can write the density operator as

$$\hat{\rho}(t) = \sum_{qs} \sum_{q's'} C_{qs, q's'}(t) |q; s\rangle \langle q'; s'|. \quad (4.2)$$

Then our governing equation describing the CQED model is defined as

$$\frac{d\hat{\rho}}{dt} = -\frac{i}{\hbar} [\hat{H}, \hat{\rho}] - \frac{i}{\hbar} [\hat{H}_d, \hat{\rho}] + L(\hat{\rho}), \quad (4.3)$$

where \hat{H} , \hat{H}_d , and L are the operators for the Hamiltonian, the driving term, and the Lindblad, respectively. The Hamiltonian \hat{H} for the coupled dot-plasmon system is

$$\hat{H} = \sum_i \hat{H}_i + \hat{H}_s + \sum_i \hat{H}_{s,i}. \quad (4.4)$$

Defining the lowering and raising operator pairs for both the QDs and the plasmon, $(\hat{\sigma}_i, \hat{\sigma}_i^\dagger)$ and $(\hat{b}, \hat{b}^\dagger)$, in the usual manner as in [30, 50], we have the isolated dot and plasmon Hamiltonian terms

$$\hat{H}_i = \hbar\omega_i \hat{\sigma}_i^\dagger \hat{\sigma}_i \quad \text{and} \quad \hat{H}_s = \hbar\omega_s \hat{b}^\dagger \hat{b}, \quad (4.5)$$

respectively, and the dot-plasmon coupling terms

$$\hat{H}_{s,i} = -\hbar g_i (\hat{\sigma}_i^\dagger \hat{b} + \hat{\sigma}_i \hat{b}^\dagger). \quad (4.6)$$

Equation (4.6) represents the simplest possible dot-plasmon coupling term corresponding to a QD gaining (losing) a quantum of energy when the plasmon loses (gains) a quantum of energy.

For the system exposed to a time-dependent electric field $E(t)$, we have

$$\hat{H}_d = -E(t) \left[\sum_i d_i (\hat{\sigma}_i + \hat{\sigma}_i^\dagger) + d_s (\hat{b} + \hat{b}^\dagger) \right], \quad (4.7)$$

where d_i and d_s denote the transition dipole moments of the QDs and plasmon, respectively.

We assume that the distance between the QDs is large compared with the separation between QDs and neighboring metal nanoparticles, so that direct through-space coupling among the QDs can be neglected. We also neglect retardation; hence, our treatment is limited to systems with physical dimensions that are small compared with optical wavelengths.

The Lindblad superoperator $L(\hat{\rho})$ in (4.3) describes the dephasing and dissipation effects. We employ a previously developed [50] extension of $L(\hat{\rho})$ that is parameterized by the QD population decay γ_p , the QD dephasing rate γ_d , and the plasmon decay constant γ_s . We consider time scales on the order of the inverse of these rates, so that there are no correlated fluctuations in the QDs' states and so that the use of the Lindblad superoperator is justified. Although environmental dephasing is explicitly included for the QDs, it is not necessary to do so for the plasmon because the dephasing that arises from its decay (encoded in the corresponding term in $L(\hat{\rho})$) is much larger in magnitude. As in Ref. [50], the rotating wave approximation is applied.

We use Woottter's concurrence [54] to measure the entanglement of the system. An alternative representation of the density operator (4.2) is the density matrix ρ

with its elements defined by

$$\rho_{qs,q's'} = \langle q; s | \hat{\rho} | q'; s' \rangle. \quad (4.8)$$

Let ρ' be the reduced density matrix associated with one particular pair of QDs, A and B , obtained by tracing the full density matrix ρ over the plasmon quantum numbers s and the quantum numbers for all other QDs. The AB pairwise concurrence is then given by

$$C_{A,B} = \max\{0, \lambda_1 - \lambda_2 - \lambda_3 - \lambda_4\}, \quad (4.9)$$

where λ_i are the square roots of the eigenvalues of $\rho' \tilde{\rho}'$ with $\lambda_i \geq \lambda_{i+1}$ (in descending order). The matrix $\tilde{\rho}'$ corresponds to the spin-flipped density matrix [54]

$$\tilde{\rho}' = (\sigma_y \otimes \sigma_y)(\rho')^*(\sigma_y \otimes \sigma_y), \quad (4.10)$$

where

$$(\sigma_y \otimes \sigma_y) = \begin{bmatrix} 0 & 0 & 0 & -1 \\ 0 & 0 & 1 & 0 \\ 0 & 1 & 0 & 0 \\ -1 & 0 & 0 & 0 \end{bmatrix}. \quad (4.11)$$

4.2.1 Approximate Analysis

We define the “dark” evolution to be how a QD-plasmon system evolves given some initial QD excitation with everything else in the system initially in the ground state. In the limit of low total excitation energy one can develop an exact analytical solution for the problem of an arbitrary number of quantum dots interacting with the plasmon if QD dephasing is neglected. This procedure is discussed in Appendix C.1. We discuss some predictions from this analysis first for two QDs and then briefly for larger numbers of QDs. Also of interest is the case of pulsed

excitation, where the system is initially cold and then subjected to a laser pulse. We follow the discussion of the dark evolution with analysis of this pulsed case using simple Rabi flopping ideas.

In the case of two QDs coupled to a plasmon, we are concerned with determining QD-plasmon coupling factors (g_1 and g_2) that maximize entanglement. For two QDs in particular, it is convenient to consider the two entangled QD states

$$|S; s\rangle = \frac{1}{\sqrt{2}} \left[|q_2 = 0\rangle |q_1 = 1\rangle + |q_2 = 1\rangle |q_1 = 0\rangle \right] |s\rangle \quad (4.12)$$

and

$$|A; s\rangle = \frac{1}{\sqrt{2}} \left[|q_2 = 0\rangle |q_1 = 1\rangle - |q_2 = 1\rangle |q_1 = 0\rangle \right] |s\rangle \quad (4.13)$$

in our calculations instead of the direct product of primitive QD states as in (4.1). For two QDs, Appendix C.1 discusses in detail a three-state Hamiltonian model involving the basis states $|q_2 = 0, q_1 = 0; s = 1\rangle$, $|S; s = 0\rangle$, and $|A; s = 0\rangle$ that neglects QD dephasing and spontaneous emission but allows for plasmon dissipation by introducing an appropriate complex diagonal matrix element to the Hamiltonian matrix. The initial state of relevance to the dark limit calculations is one with an excited QD1, an unexcited QD2, and a plasmon; this state is represented by $|0, 1; 0\rangle = \frac{1}{\sqrt{2}}(|S; 0\rangle + |A; 0\rangle)$. This initial state is interesting because although it is a separable, unentangled state, it is a nonstationary state of the full system that has been shown to evolve into a state with a possibly significant transient degree of entanglement [30, 38, 39]. With no plasmon dissipation ($\gamma_s = 0$) and for short times t , the probabilities of states $|0, 0; 1\rangle$, $|S; 0\rangle$, and $|A; 0\rangle$ are given by the respective squares of $a_0(t)$, $a_S(t)$, and $a_A(t)$, where

$$\begin{bmatrix} a_0(t) \\ a_S(t) \\ a_A(t) \end{bmatrix} \approx \begin{bmatrix} -ig_1 t \\ \frac{1}{\sqrt{2}} - \frac{g_1(g_1+g_2)t^2}{2\sqrt{2}} \\ \frac{1}{\sqrt{2}} + \frac{g_1(g_2-g_1)t^2}{2\sqrt{2}} \end{bmatrix}. \quad (4.14)$$

When $\gamma_s > 0$, the limit as $t \rightarrow \infty$ is of interest because the system can then reach a steady state in the populations. Appendix C.1 shows that for the initial condition with one excited QD and the rest of the system unexcited,

$$a_S(\infty) = \frac{1}{\sqrt{2}(1+x^2)}x(1-x) \quad (4.15)$$

and

$$a_A(\infty) = \frac{1}{\sqrt{2}(1+x^2)}(1-x), \quad (4.16)$$

where $x = \frac{g_1 - g_2}{g_1 + g_2}$. Remarkably, these results are valid for any positive value of γ_s (although it must be remembered that no QD dephasing has been allowed). The concurrence in this asymptotic limit is simply $|a_A(\infty)|^2 - |a_S(\infty)|^2$ and can be readily maximized to yield the optimum ratio of coupling strengths: $x = -2 + \sqrt{3}$ or

$$\frac{g_2}{g_1} = \sqrt{3}. \quad (4.17)$$

Appendix C.1 also develops an *exact* procedure for constructing the corresponding dark dynamics of N QDs interacting with a plasmon, without QD dephasing. This system is then described by an effective $(N+1) \times (N+1)$ complex effective Hamiltonian model. For the scenario of one QD initially excited, it can be used to get an idea of how the entanglement results scale with increasing N .

We are also interested in the case when the system is initially unexcited and an optical pulse is used to generate transient entanglement. Assuming the pulse is relatively simple and resonant with the QDs' transition frequencies, a simple question to ask is what values of g_1 and g_2 will lead to the two-QD system being close to the $|0, 1; 0\rangle$ state. We know from previous work [30, 38, 39] that such a system will evolve into a state with some degree of entanglement. On resonance, the QDs undergo Rabi oscillations as they are excited by the laser pulse. The time

for QD*i* to undergo one Rabi oscillation (i.e., to go from the ground state to the excited state and then back to the ground state) is $2\pi/\Omega_R(i)$, where

$$\Omega_R(i) = \frac{\mu_i E_0^{\text{loc}}(i)}{\hbar} = \frac{2g_i \mu_s E_0}{\hbar \gamma_s}, \quad (4.18)$$

with $E_0^{\text{loc}}(i)$ being the amplitude of the sinusoidal electric field experienced locally by QD*i*. The final term in (4.18) is obtained by using the expression for E_0^{loc} derived in Appendix C.2, which relates this local electric field to the incident field E_0 . (Other phenomena, such as the Purcell effect, are also occurring; the Rabi formulae (4.18) discussed here should be construed as approximate indicators of the dynamics.) In order to achieve a highly entangled state, one QD, say QD1, must undergo $m - \frac{1}{2}$ Rabi oscillations (with $m = 1, 2, \dots$) so that it is left in the excited state. The time for this process to occur is $2\pi(m - \frac{1}{2})/\Omega_R(1)$. The other dot, QD2, must undergo $n = 1, 2, \dots$ full oscillations so that it is left in its ground state. The time for this process to occur is $2\pi n/\Omega_R(2)$. Equating these two Rabi times leads to the simple result that

$$\frac{g_2}{g_1} = \frac{n}{m - \frac{1}{2}}. \quad (4.19)$$

We see that the condition (4.19) on the couplings for achieving one QD excited via pulsed excitation is not the same as the condition (4.17) on the couplings for that excited state to evolve to an entangled state. Nonetheless, for $m = n = 1$, (4.19) predicts $g_2/g_1 = 2$, in approximate accord with (4.17) where $g_2/g_1 \approx 1.73205$. Although this restricts the parameter space for the pulsed case somewhat, many parameters (especially those describing the pulse) can still be varied freely.

4.2.2 Concurrence Optimization

To find the set of system parameters that maximize the sum of the pairwise concurrences, we employ a numerical optimization framework that samples the parameter space in a uniformly random fashion, evaluating the concurrence at each point. The parameters in question include the N QD-plasmon coupling coefficients ($g_i, i = 1, 2, \dots, N$), environmental aspects such as the QD dephasing and plasmon decay constants (γ_d and γ_s , respectively), and applied laser pulse features such as its fluence (F) and duration (τ). (See Sec. 4.2.3 for definitions of the laser pulse parameters.) Since the sum of the pairwise concurrences is a nonconvex function of these parameters, several isolated local maxima are likely to exist. Our approach follows that in Ref. [71], clustering evaluated points in the parameter space into basins of attraction for different maxima. Clusters are formed by using the points' function values (sum of pairwise concurrences) and their proximity to points with better function values. Points that do not have a better point within a distance d are considered the best points in their cluster. The distance d can be adjusted so a reasonable number of clusters are identified. (One also can dynamically adjust d as the parameter space is explored [71, 72].) Local optimization runs are then started from the best point in each cluster.

The local optimization problem of maximizing the sum of pairwise concurrences is solved by minimizing the figure of merit

$$\sum_{i < j} (1 - C_{i,j})^2, \quad (4.20)$$

where $C_{i,j}$ depends on the system parameters being optimized over (see (4.9)). This form is appropriate because the pairwise concurrences in (4.20) are bounded above by 1. Depending on the context, $C_{i,j}$ might be the maximum concurrence achieved over time or a long-time asymptotic limit. When viewed as a function

of the parameters, (4.20) defines a nonlinear least-squares problem. We solve this problem with the Practical Optimization Using No Derivatives for sums of Squares (POUNDERs) algorithm [73,74]. For a system with N QDs, POUNDERs iteratively builds local quadratic surrogates of each of the $\binom{N}{2}$ residual functions $\{1 - C_{i,j}\}$ and combines this information in a master surrogate model. In each iteration of the algorithm, this surrogate model is minimized within a trust-region framework to generate candidate solutions.

4.2.3 Simulation Details

We consider the time evolution of the density operator in (4.3), with the choices of the parameters corresponding to a gold nanoparticle system interacting with QDs in a polymer matrix with a dielectric constant $\epsilon_{med} = 2.25$; these choices are similar to those originally used in a single plasmonic-QD system study [50]. For QD i , we choose $\hbar\omega_i = \hbar\omega_s = 2.05$ eV, assuming the QD and plasmon transition energies are equal. We set the QD dipole moments to be $d_i = 13$ D and the plasmon dipole moment to be $d_s = 4000$ D. The QDs are assumed to have the same spontaneous decay rate, $\hbar\gamma_p = 190$ neV. In some of our calculations we vary or consider several values for the QD dephasing rate, γ_d , and plasmon decay rate, γ_s . Consistent with our earlier work, base values are $\hbar\gamma_d = 2$ meV and $\hbar\gamma_s = 100$ meV. We utilize coupling factors, $\hbar g_i$, in the 0–30 meV range; and unlike all the other QD parameters, we do allow QDs to have different coupling constant values. Previous calculations show that a realistic approximation for the plasmon-QD coupling is approximately 10 meV for a system such as the one we study here [50]. Other systems, such as silver nanoparticles or particles with different geometries, could exhibit larger coupling factors than does gold [53]. For

calculations that include a laser pulse $E(t)$, we assume it has the form (in the nonrotating frame) $E(t) = G(t)E_0 \cos(\omega_0 t)$, where $\omega_0 = \omega_s = \omega_i$ and $G(t)$ is a Gaussian envelope function such that the full width at half maximum of $E^2(t)$ is τ . The pulse fluence is $F = \int_{-\infty}^{+\infty} dt \sqrt{\epsilon_{med}} c \epsilon_0 E^2(t)$.

We formulate a density matrix equation from (4.3) using (4.8), and we solve the density matrix equation consisting of a set of M^2 ordinary differential equations for the time-dependent complex amplitudes $C_{qs,q's'}(t)$, with $M = 2^N N_s$ where N is the number of QDs and N_s is the number of plasmon energy levels. We solve these ODEs numerically using an efficient parallel solver that employs sparse matrix-matrix multiplication algorithms with either a Runge-Kutta or exponential time integration scheme [51, 52].

4.3 Results

We now detail our quantum dynamics results corresponding to a system of QDs interacting with a plasmonic system as modeled in Sec. 4.2. We analyze such systems for both free evolution of some particular excitation (what we refer to as “dark” evolution) and in the presence of a laser pulse.

4.3.1 Two Quantum Dots in the Dark

We first consider two QDs (QD1 and QD2) interacting with a plasmonic system under the assumption that the initial state $|q_2 = 0, q_1 = 1; s = 0\rangle$ has been prepared and evolves in the absence of any external pulses, that is, “in the dark.” With one QD excited and the other QD in its ground state, this initial condition rep-

resents an equal superposition of symmetric and antisymmetric states, $|S; s = 0\rangle$ and $|A; s = 0\rangle$ (Eqs. (12) and (13)). While each of these latter two states is entangled, their superposition is not entangled at all. As shown previously, [30, 38, 39], however, the system evolves into a state with a high degree of concurrence. The reason is that the $|S; s = 0\rangle$ state rapidly decays while the $|A; s = 0\rangle$ undergoes a much slower decay leading to a more purely entangled state. Moreover, when we start from a completely cold system and apply a pulse and optimize couplings to maximize concurrence, the resulting transitory dynamics can involve just one QD being excited before evolving to a more entangled state. Unlike cases studied in previous work [30, 38, 39], the possibility of asymmetric dot-plasmon couplings ($g_1 \neq g_2$) can lead to new features in the time-dependent concurrence.

When the QDs are symmetrically distributed within the plasmonic system so that $g_1 = g_2$, the $|A; s\rangle$ state is an eigenstate of the Hamiltonian (4.4) and decays with a relatively slow dephasing rate (γ_d) due only to the Lindblad term in (4.3). With finite (but still symmetric) coupling, the $|S; 0\rangle$ state mixes with the $|S; 1\rangle$ state [30] and is no longer an eigenstate of the Hamiltonian. The probability of being in $|S; 0\rangle$ is $\frac{1}{2} \cos^2(\sqrt{2}gt)$, leading to an increased initial decay of the $|S; 0\rangle$ state. The plasmon decay (γ_s) damps out any additional oscillations of the $|S; 0\rangle$ population. As shown previously [30], starting a system in the $|0, 1; 0\rangle$ state then leads to a high degree of concurrence, since the $|S; 0\rangle$ state quickly decays, while the $|A; 0\rangle$ state undergoes a much slower decay. With $\gamma_d = 0$, the maximum concurrence for such a symmetric system is therefore 0.5. We describe here a method to achieve larger degrees of concurrence by forcing the $|S; 0\rangle$ state to evolve into $|A; 0\rangle$ rather than into $|0, 0; 1\rangle$.

By breaking the symmetry of the couplings between the two QDs, we mix

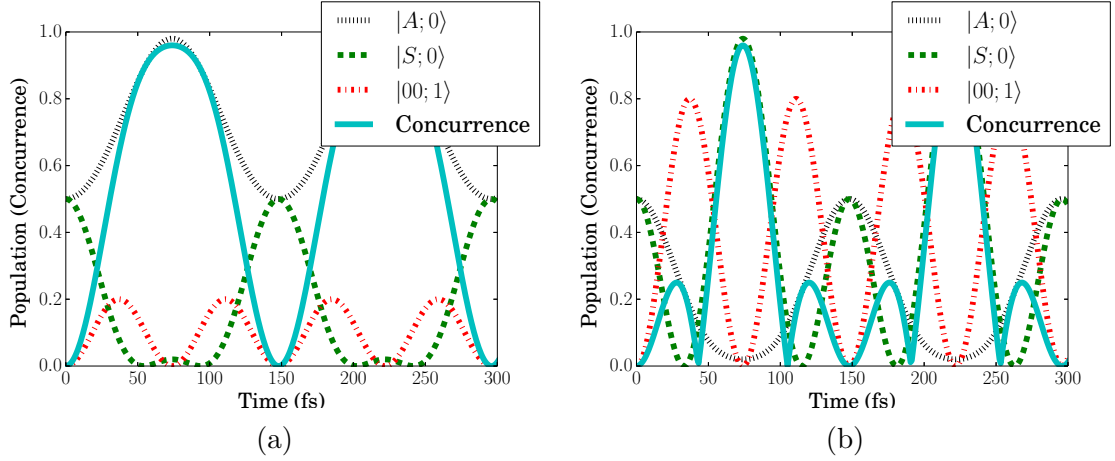


Figure 4.1: Time dependence of the populations of the states $|S; s = 0\rangle$, $|A; s = 0\rangle$, and $|q_2 = 0, q_1 = 0; s = 1\rangle$, and the concurrence, for a two-QD system initially in the $|q_2 = 0, q_1 = 1; 0\rangle$ state, with no surface plasmon decay or QD dephasing, i.e., $\hbar\gamma_s = \hbar\gamma_d = 0$ meV. (a) A case with $g_1 < g_2$ corresponding to the initially excited QD1 not being as strongly coupled to the surface plasmon as QD2: $\hbar g_1 = 12.5$ meV, $\hbar g_2 = 25$ meV. (b) A case with $g_1 > g_2$: $\hbar g_1 = 25$ meV, $\hbar g_2 = 12.5$ meV.

the $|S; 0\rangle$ state with the $|A; 0\rangle$ state, through the $|0, 0; 1\rangle$ state. This approach follows the analysis in Appendix C.1 where a three-state model is discussed and solved analytically in certain limits. When $g_1 = g_2$, no coupling occurs between $|S; 0\rangle$ and $|A; 0\rangle$; but when $g_1 \neq g_2$, the two states are indirectly coupled through the $|0, 0; 1\rangle$ state (to which both states are directly coupled). Starting in the $|0, 1; 0\rangle = (|A; 0\rangle + |S; 0\rangle)/2$ state and setting $\hbar\gamma_s = \hbar\gamma_d = 0$ meV lead to a cyclic evolution between a completely unentangled state and a highly entangled state.

We follow the convention that QD1 is the QD that is initially in its excited state. If $g_1 < g_2$, then the $|A; 0\rangle$ state reaches a population approaching 1 (Fig. 4.1a); if $g_1 > g_2$, then the $|S; 0\rangle$ state reaches a population approaching 1 (Fig. 4.1b). The dynamics of these two examples are similar; the $|A; 0\rangle$ (resp. $|S; 0\rangle$) state evolves into the $|0, 0; 1\rangle$ state, which evolves into the $|S; 0\rangle$ (resp. $|A; 0\rangle$) state and back through the $|0, 0; 1\rangle$ state into its initial state. Where the $|S; 0\rangle$ (resp. $|A; 0\rangle$) state reaches its maximum, the concurrence does as well, reaching a value of nearly

1. Using the explicit three-state system described in (C.9) in Appendix C.1, we find the ratio $g_1/g_2 = \sqrt{2} - 1 \approx 0.414$ gives an $|A;0\rangle$ state population of unity, which also maximizes the concurrence for the $g_1 < g_2$ case. A similar analysis can be done for the $|S;0\rangle$ state, giving $g_1/g_2 = \sqrt{2} + 1 \approx 2.414$. Note that these optimal ratios for achieving large, instantaneous concurrences when there is no dissipation are different from those of Sec. 4.2.1. The latter concern either an asymptotic concurrence that can be reached in the case of dissipation or the couplings conducive to a pulsed laser generating a particular excited state that can then evolve to a state with significant concurrence.

For short times t , the approximation (4.14) applies. When $g_1 < g_2$ in this case, the second term of $a_A(t)$ is positive, which leads to a boost in the population of the $|A\rangle$ state. When $g_1 > g_2$, the second term is negative, and the population of the $|A\rangle$ state initially declines. In both cases, $a_S(t)$ initially declines; but when $g_1 > g_2$, it reaches 0 much faster and then rises to nearly 1. Both effects can be seen in Fig. 4.1.

When the Lindblad terms describing dissipation and dephasing are added, the results of the two simulations $(\hbar g_1, \hbar g_2) = (12.5 \text{ meV}, 25 \text{ meV})$ or $(25 \text{ meV}, 12.5 \text{ meV})$ in Fig. 4.1 become very different. In Fig. 4.2 we consider simply adding plasmon dissipation ($\gamma_s > 0$) to the simulations, while keeping the QD dephasing term γ_d at zero. This case also has a closed-form solution (see Appendix C.1 and Sec. 4.2.1). We see from Figs. 4.2a and 4.2b that the initial state evolves and begins to populate the first excited plasmon state, but the plasmon population quickly decays and the system reaches a steady state. The steady-state concurrence for the case with $g_1 < g_2$, Fig. 4.2a, is larger than the case with $g_1 > g_2$, Fig. 4.2b. This trend might be expected on the basis of the dynamics without plasmon de-

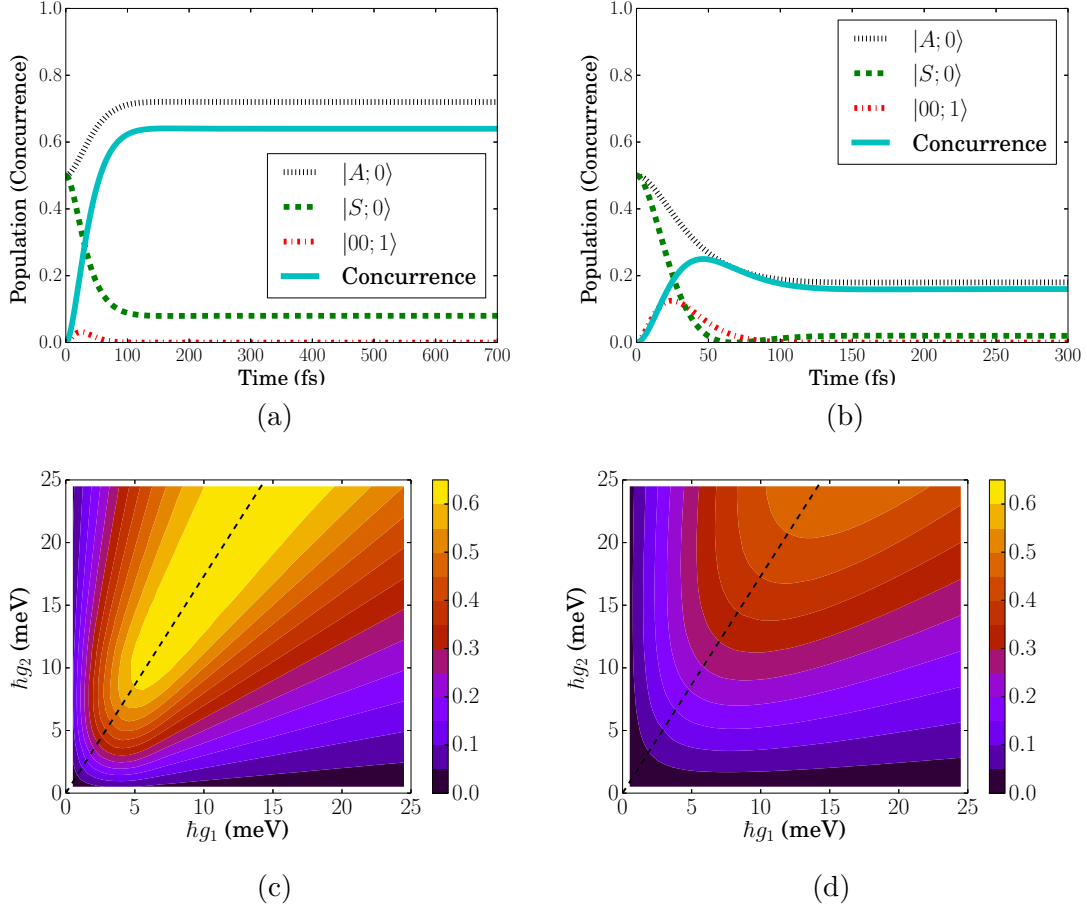


Figure 4.2: Results for a surface plasmon decay width $\hbar\gamma_s = 100$ meV. Upper two panels (a) and (b) show the time-dependence of the the $|S; s = 0\rangle$, $|A; s = 0\rangle$, $|q_2 = 0, q_1 = 0; s = 1\rangle$ state populations and concurrence for a two-QD system, initially in the $|q_2 = 0, q_1 = 1; 0\rangle$ state, and with no QD dephasing, i.e., $\hbar\gamma_d = 0$ meV. The cases with (a) $\hbar g_1 = 12.5$ meV, $\hbar g_2 = 25$ meV and (b) $\hbar g_1 = 25$ meV, $\hbar g_2 = 12.5$ meV are displayed. The lower two panels (c) and (d) are the maximum concurrences found as a function of the QD/plasmon coupling factors, g_1 and g_2 . Panel (c) corresponds to no QD dephasing, $\gamma_d = 0$, and contains within it the concurrence maxima from the particular cases (a) and (b) above. Panel (d) is the corresponding maximum concurrence when the QD dephasing is set to $\hbar\gamma_d = 2.0$ meV. The dashed lines in (c) and (d) represent $g_2 = \sqrt{3}g_1$.

cay, Figs. 4.1a and 4.1b, wherein a smooth rise of concurrence from 0 to 1 occurs over initial times for the case $g_1 < g_2$, Fig. 4.1a, but a more complicated behavior involving a small local maximum in concurrence occurs for the case $g_1 > g_2$, 4.1b. In a realistic system, the $g_1 > g_2$ case will not create concurrences as large as those seen when $g_1 < g_2$; the best case is that the plasmon decay is sufficiently large to stop the $|A;0\rangle$ state from evolving into the $|S;0\rangle$ state. Figure 4.2c shows the maximum concurrence (for each time trajectory) for many different values of g_1 and g_2 . There is a clear area of large concurrence when $g_2 \approx \sqrt{3}g_1$ in accordance with the expectation from (4.17) in Sec. 4.2.1. Small discrepancies with respect to (4.17) can exist because this equation pertains to the asymptotic concurrence and we are considering the maximum concurrence achieved over a finite window of time.

Note that the isolated QD population decay rates γ_p (discussed in Sec. 4.2.3) are sufficiently small and are generally overwhelmed by the Purcell decays that result from finite γ_s and plasmon-dot coupling factors, g_i . Thus, the inclusion of decay in the QD populations has no significant effect on the results presented here for the other parameter values considered. The QD dephasing terms γ_d , however, can have a more significant effect. Figure 4.2d (similar to Fig. 4.2c but with $\hbar\gamma_d = 2.0$ meV) shows the maximum concurrence for many values of g_1 and g_2 . Naturally, the maximum concurrence is not as large as the $\hbar\gamma_d = 0$ meV case. Furthermore, the clear peak around the line $g_2 \approx \sqrt{3}g_1$ has been distorted, although the line still has some significance. Including QD dephasing effects causes the QD populations to decay before significant entanglement can occur, unless the QDs are strongly coupled. At small values of g_i , the optimal point is far from the $\sqrt{3}$ line; but as the couplings are increased, the optimal points again fall upon the $\sqrt{3}$ line. As mentioned above, this derivation pertains to the asymptotic values of

the concurrence, but the dephasing does not allow the system to approach that value without larger values of g_i .

4.3.2 $N > 2$ Quantum Dots in the Dark

We have used the analytical solution for N QDs interacting with a plasmonic system with no QD dephasing (Appendix C.1) to explore how the dark entanglement dynamics scales with increasing N beyond $N = 2$. As noted in Sec. 4.3.1, introducing dephasing can lead to smaller concurrences and shifts in the optimal g_j/g_i ratios, but our results should indicate what to qualitatively expect as N increases. As in our $N = 2$ dark calculations, the initial condition corresponds to QD1 being initially excited.

For the $N = 3$ case, Fig. 4.3 shows a contour map of the asymptotic figure of merit (4.20) as a function of g_2/g_1 and g_3/g_1 . The results in this case do not depend on either g_1 or the plasmon decay rate γ_s , provided that the latter is positive. (The transient dynamics do depend on both g_1 and γ_s and can also be of interest.) We see that the optimal concurrences are reached at $g_2/g_1 = g_3/g_1 \approx 1.05$, which is somewhat smaller than the $g_2/g_1 = \sqrt{3}$ ratio found for the $N = 2$ case. The optimal values of the concurrence are $C_{1,2} = C_{1,3} \approx 0.450$ and $C_{2,3} = 0.215$. At 0.450, the “direct” concurrence between the initially excited dot and the other two dots is slightly smaller than the result for the two-QD system.

Although we have not derived an explicit formula, we can evaluate the exact asymptotic dynamics of the N QD case using the procedure described in Appendix C.1. We find that for the initial condition in question, two distinct concurrence values always exist: a major one (C^{maj}), associated with all the QD pairs

that involve the initially excited QD, and a smaller one (C^{\min}), associated with all the indirectly excited pairs. Evaluation of the results for N up to $N = 150$ shows that $C^{\text{maj}} \approx 0.54/\sqrt{N}$, for $N > 100$; that is, the major concurrence tends to zero, although it does so slowly, with an increasing number of QDs. In this limit, the minor concurrence decays somewhat faster, with $C^{\min} \approx 0.50/N$. Also, the optimal concurrence figure of merit is achieved with just one unique ratio for all the couplings, $g_{i>1}/g_1 = x$. We find that $x \approx 1.09/\sqrt{N}$ for $N > 100$.

The optimal value of g_2 becomes less than g_1 when $N = 4$, in contrast to the two- and three-QD systems, where $g_1 < g_2$. This can be explained by looking at the relative fraction of QD pairs, $2/N$, which have $C_{i,j} = C^{\text{maj}}$. When $N < 4$, the fraction of QD pairs that have $C_{i,j} = C^{\text{maj}}$ is greater than $1/2$. As N becomes larger, more and more QD pairs have $C_{i,j} = C^{\min}$. When $g_1 > g_2$, there is a boost in C^{maj} , possibly at the cost of C^{\min} . When N is large, the solution from minimizing the figure of merit (4.20) no longer favors boosting C^{maj} ; instead it increases the (more numerous) C^{\min} .

The state created by this mechanism, where all QDs share bipartite entanglement (possibly weakly) with all other QDs, is similar to a generalized W-state [75]. In the W-state, all pairs of qubits have the same value of concurrence, and that value is as large as possible. Thus, the W-state is the optimal state, given our figure of merit. According to an idea known as the monogamy of entanglement [76], there is an upper bound on the possible sum of bipartite entanglement. When $N > 2$, each qubit pair can no longer be fully entangled. As N increases, the maximum bipartite concurrence for each pair in the W-state decreases as $2/N$. This represents a fundamental limit on the entanglement that we can achieve in our system. The decay of the concurrence with increasing N in our QD-plasmon

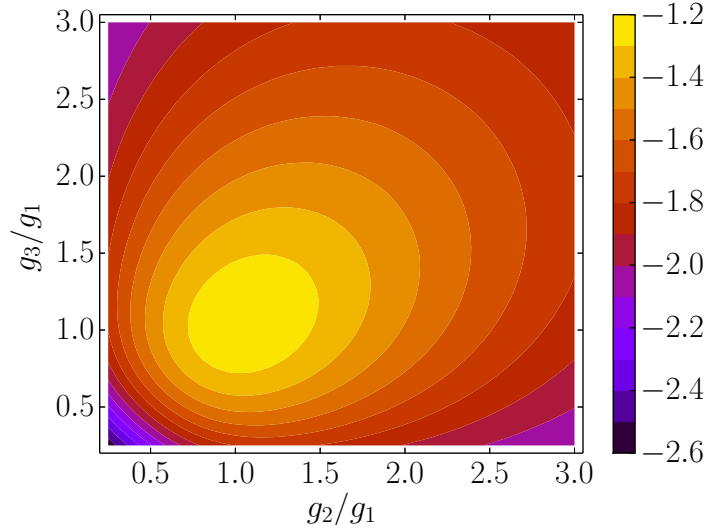


Figure 4.3: Asymptotic figure of merit, Eq. (4.20) for a three-QD system, with one QD initially excited, $\gamma_s > 0$, and $\gamma_d = 0$, as a function of the ratios of the QD/plasmon coupling parameters.

system is similar to that of the W-state. Furthermore, if we measure the initially excited QD, we can project onto a state where QD pairs share a small degree of entanglement with each other. Taking a ratio of the asymptotic value of C^{\min} in the projected state to the W-state concurrence shows that each QD pair will have only 1/4 of the concurrence of the W-state. While this may be a small fraction, it is a constant fraction with increasing N , allowing a (low-fidelity) approximate W-state to be easily created for any number of QDs. The addition of decay in the QD populations will further decrease the fidelity; but, as shown in the two-QD case, the entanglement still persists, although at a smaller value.

Table 4.1: Constraints for optimization parameters.

Parameter	Lower Bound	Upper Bound
$\hbar g_i$ (meV)	0	25
F (nJ/cm ²)	0	700
τ (fs)	10	200
$\hbar\gamma_d$ (meV)	0	5
$\hbar\gamma_s$ (meV)	100	300

4.3.3 Two Quantum Dots Subjected to Ultrafast Laser Pulses

Preparing a system in the initial state $|0, 1; 0\rangle$ can create high degrees of entanglement, but it does not represent a simple experimental setup. A simpler setup is to prepare a system and excite it with a single optical pulse. Introducing a laser pulse to a system increases the number of parameters that the system depends on and can have a large effect on the value of the concurrence [30]. For the two-QD system, the parameters varied include the laser fluence (F), laser duration (τ), coupling strengths (g_1 and g_2), QD dephasing (γ_d), and plasmon dephasing (γ_s); ω_i , ω_s , d_i , d_s , and γ_p remain fixed. We also constrained the parameter values in a physically reasonable part of the parameter space; see Table 4.1.

We used POUNDerS to find optimal parameters in different parts of the parameter space defined in Table 4.1. We optimized the sum of the maximum value of the pairwise concurrence over the time horizon; other figures of merit (such as the sum of the integral of the pairwise concurrences over the time window) will be investigated in future work.

The evolution of the pairwise concurrence and the states' populations for a locally optimal result are given in Fig. 4.4a and are seen to behave similarly to the

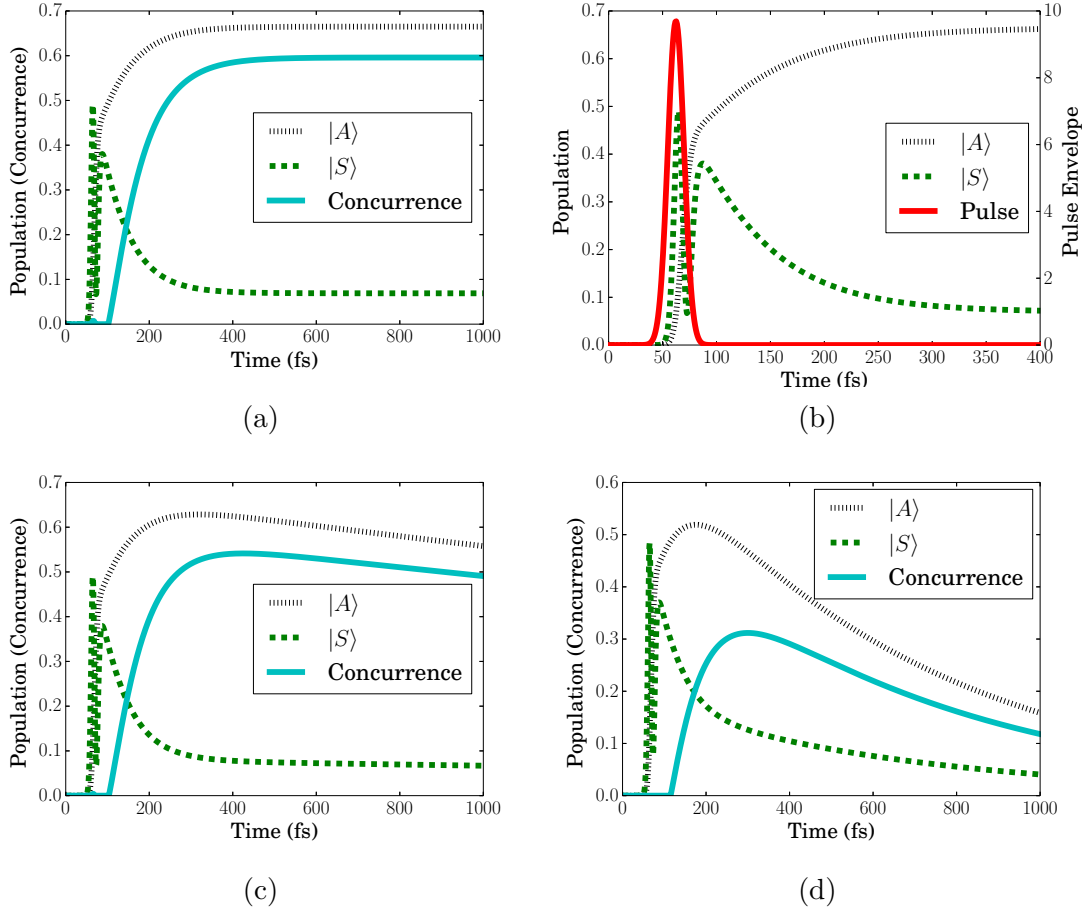


Figure 4.4: Panels (a) and (b) show the time-dependence of the populations of the $|A\rangle$ and $|S\rangle$ states (traced over all $|s\rangle$) and concurrence for pulsed excitation of an initially cold two-QD/surface plasmon system with parameters $\hbar g_1 = 12.8$ meV, $\hbar g_2 = 24.9$ meV, $F = 263.4$ nJ/cm², $\tau = 12.5$ fs, $\hbar\gamma_s = 186$ meV, and $\hbar\gamma_d = 0$ meV. These parameters are the result of a local optimization run. Panels (c) and (d) keep these same parameter values except for the QD dephasing, which is either (c) $\hbar\gamma_d = 0.2$ meV or (d) $\hbar\gamma_d = 2$ meV.

dark case with one initially excited QD shown in Fig. 4.2a. In contrast to that system, the plasmon population (not shown) reaches a much higher value of nearly 10 in this system. (The $|A\rangle$ and $|S\rangle$ state populations shown in Fig. 4.4 result from tracing the density matrix over all plasmon quantum numbers.) We previously discovered that we had to allow g_1 and g_2 to differ in order to create large amounts of concurrence because doing so allowed the system to approximate the $|0, 1\rangle$ state,

creating a highly entangled state, with the proper parameter choices [30]. We noted there that the less-strongly coupled QD achieved a higher population after the pulse concluded. The boost in the $|A; s = 0\rangle$ population we describe in this paper for the case $g_1 < g_2$ (see discussion of Fig. 4.1) is also present, helping raise the concurrence higher and thereby allowing the pulsed case to reach levels of concurrence similar to those for the dark case. This is clearly seen in Fig. 4.4b, where the initial time scale has been expanded and the pulse envelope is also displayed. After the pulse ends, the $|S\rangle$ state begins to decline, but the $|A\rangle$ state grows, because of their indirect coupling. This boost of the $|A\rangle$ state is the same as seen in the dark case. Figures 4.4c–4.4d also show this same parameter set with larger values of γ_d . The maximum value of the pairwise concurrence strongly depends on the QD dephasing, γ_d . This dependence is not surprising because longer coherence times are almost always associated with larger degrees of (and longer-lived) entanglement. Figure 4.4c shows the system at $\hbar\gamma_d = 0.2$ meV (approximately liquid helium temperatures), while Fig. 4.4d shows the system at $\hbar\gamma_d = 2.0$ meV (approximately liquid nitrogen temperatures). The loss in concurrence from $\hbar\gamma_d = 0$ meV to $\hbar\gamma_d = 0.2$ meV is only about 10%, but it is almost 50% when $\hbar\gamma_d$ is raised to 2.0 meV. Generally, the concurrence increases with decreasing γ_d .

Figure 4.5 shows the maximum concurrence over our time window as g_1 and F vary, for fixed pulse duration (τ) and coupling strength of the second QD (g_2). An interesting consequence of the Rabi oscillations is bifurcations of the areas of high concurrence. At small laser fluences, given $g_1 < g_2$, there is only one region of high concurrence corresponding to one QD undergoing a half Rabi oscillation and the other undergoing one oscillation; that is, the $m = n = 1$ case from Sec. 4.2.1 that was predicted to maximize entanglement. As the laser fluence is increased, the region of high concurrence splits into two regions, as the more-strongly coupled

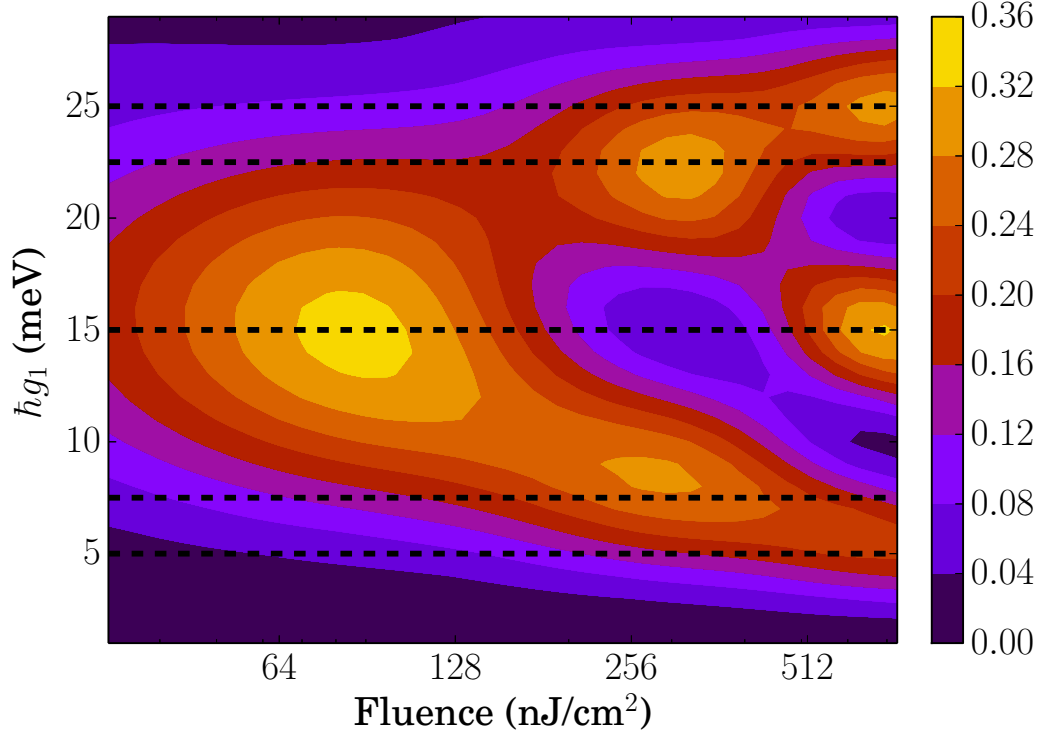


Figure 4.5: Maximum concurrence for a parameter sweep of the two-QD system, with $\hbar g_2 = 30$ meV, $\tau = 20$ fs, $\hbar \gamma_s = 150$ meV, $\hbar \gamma_d = 2$ meV. The dashed lines represent coupling ratios obeying Eq. (4.19).

QD approaches two full Rabi oscillations. The less-strongly coupled QD can now go through either one half or one-and-a-half Rabi oscillations to end up in the excited state. This region bifurcates again, as the second dot approaches three Rabi oscillations. This analysis works for the two-QD and three-QD systems we present in this paper, but it gives a relationship only between two of the parameters, g_1 and g_2 . Since we have many other parameters to optimize over, POUNDerS is used to find local optima of the maximum concurrence.

4.3.4 Three Quantum Dots Subjected to Ultrafast Laser Pulses

Since the QDs are assumed to be coupled to the plasmon but not to each other, adding a QD increases the number of parameters only by one (g_3 , the new QD's coupling to the plasmon). More important, the size of the Hilbert space needed for the simulation increases by a factor of 2, more than quadrupling the simulation's run time and making the optimization algorithm's ability to quickly find locally optimal solutions even more important. Here we present two locally optimal points for a three-QD system. The QD dephasing, $\hbar\gamma_d$, is fixed to 0.2 meV, since this approximates a physically realizable system at liquid helium temperatures.

Figure 4.6 shows the populations of the QDs and their pairwise concurrences for the system parameters returned from a local optimization run. This system is analogous to the two-QD systems discussed above, since $g_2 = g_3$. QD2 and QD3 undergo two Rabi flops, and QD1 undergoes one-and-a-half Rabi flops. Accordingly, $g_2/g_1 = g_3/g_1 = 1.322 \approx \frac{4}{3}$, as predicted by (4.19). The boost of the population of the $|A\rangle$ state is also apparent in this system. Shortly after the pulse has concluded, the $|A\rangle$ state is still rising, while the $|S\rangle$ state decays. The boost of the $|A\rangle$ state eventually finishes, and the $|S\rangle$ and $|A\rangle$ states then decay at similar rates. Aside from having a much larger concurrence than presented previously, the pulsed three QD simulations presented in this paper are interesting because their coupling parameters are smaller and represent a more physically reasonable system than do our previous results [30].

Figure 4.7 shows the populations and concurrences for a system with the best parameters from a different local optimization run. The QDs in this system all

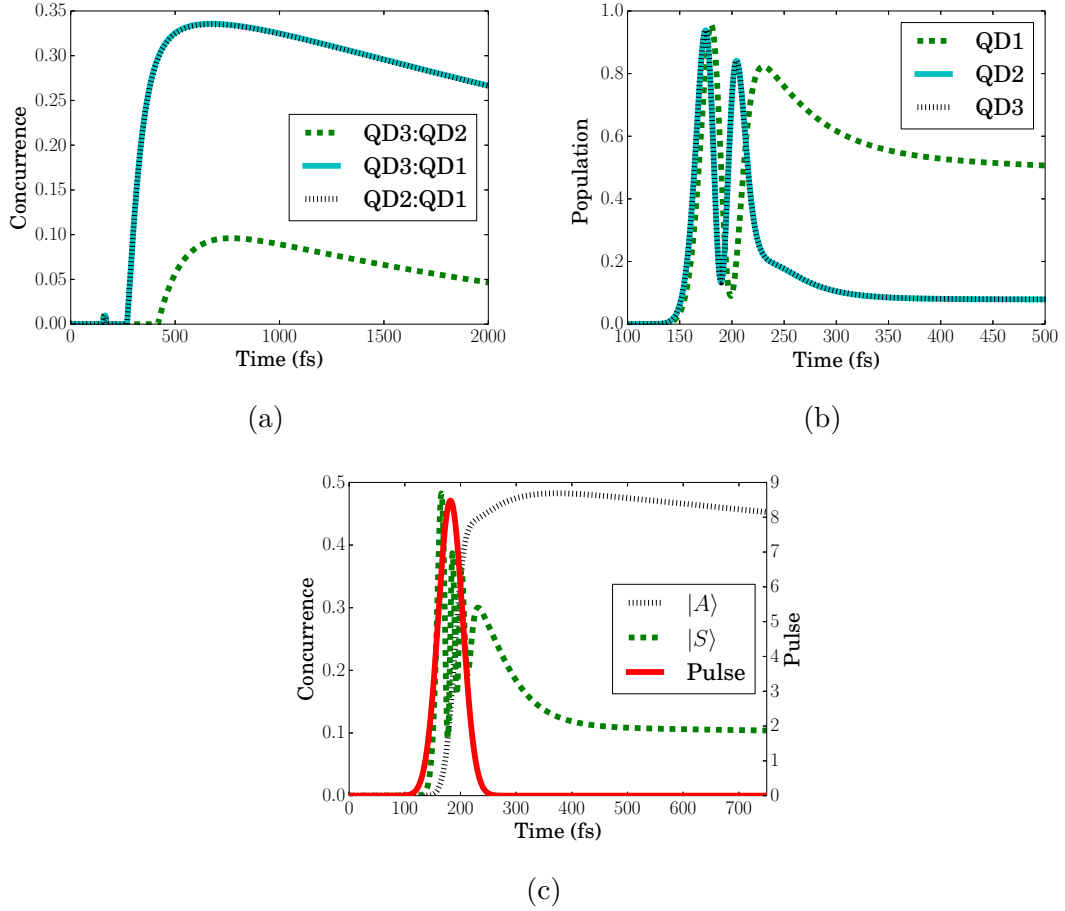


Figure 4.6: Populations and concurrences for the final parameters from a local optimization run on the three-QD system with $\hbar\gamma_d$ fixed at 0.2 meV. The final parameters are $\hbar g_1 = 14.6$ meV, $\hbar g_2 = 19.3$ meV, $\hbar g_3 = 19.3$ meV, $F = 587.0$ nJ/cm², $\tau = 36.4$ fs, and $\hbar\gamma_s = 180.4$ meV (with $\hbar\gamma_d$ fixed at 0.2 meV). Panel (a) shows the various bipartite concurrences, and panel (b) shows the QD excitation probabilities. Because $g_2 = g_3$, the QD3:QD1 and QD2:QD1 concurrences are identical, as are the QD2 and QD3 excitation probabilities. Panel (c) shows the time-dependent probabilities of the $|S\rangle$ and $|A\rangle$ states associated with either the QD3:QD1 or QD2:QD1 subsystems and the pulse envelope.

have different coupling values (as opposed to the previous example where $g_2 = g_3$), leading to three different pairwise concurrences, even though the populations of QD2 and QD3 are similar in value. QD3 undergoes four Rabi flops, while QD1 undergoes three-and-a-half Rabi flops, leading to $g_3/g_1 = 1.142 \approx \frac{8}{7}$. Additionally, QD2 undergoes three Rabi flops, leading to $g_2/g_1 = 0.858 \approx \frac{6}{7}$. Both these pairs

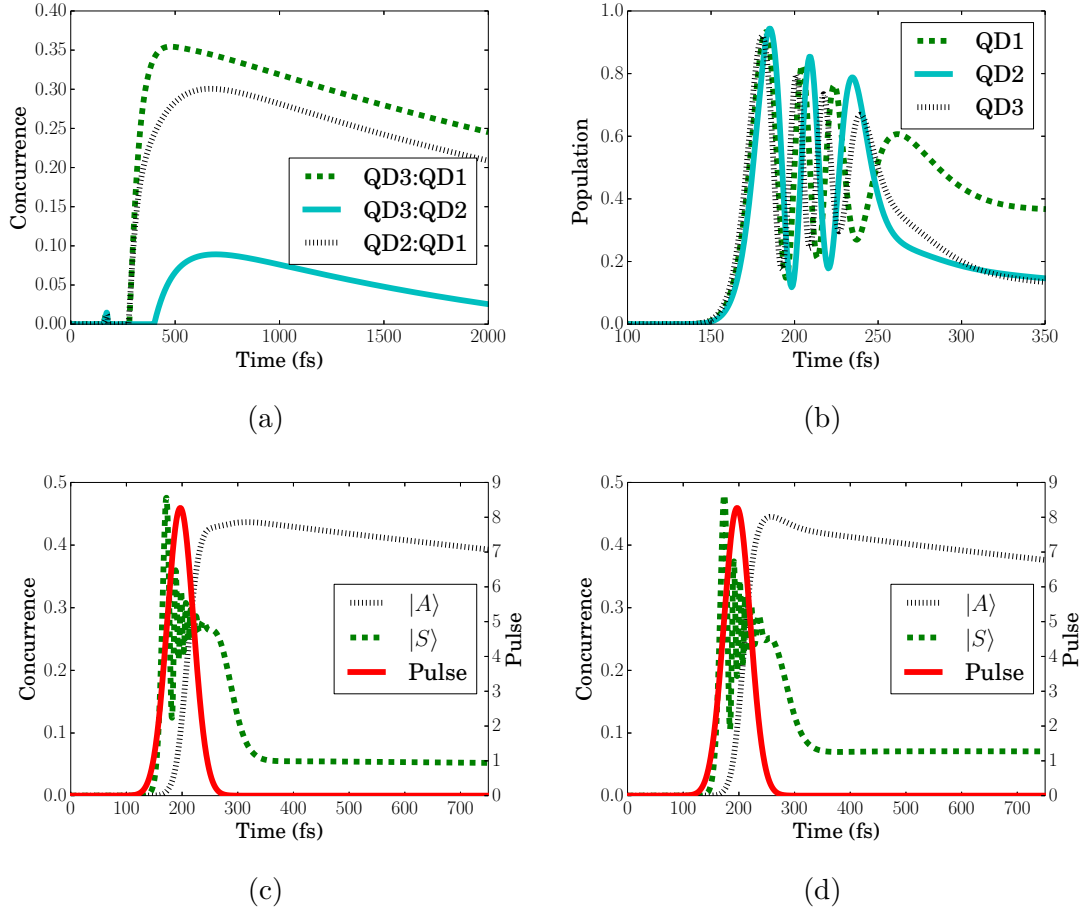


Figure 4.7: Populations and concurrences for the final parameters from a second local optimization run on the three-QD system with $\hbar\gamma_d$ fixed at 0.2 meV. The final parameters are $\hbar g_1 = 19.0$ meV, $\hbar g_2 = 16.3$ meV, $\hbar g_3 = 21.7$ meV, $F = 603.4$ nJ/cm², $\tau = 39.4$ fs, and $\hbar\gamma_s = 107.7$ meV (with $\hbar\gamma_d$ fixed at 0.2 meV). Panel (a) shows the various bipartite concurrences, and panel (b) shows the QD excitation probabilities. The pulse envelope and the populations of the $|S\rangle$ and $|A\rangle$ states are shown for the QD3:QD1 pair in panel (c) and the QD2:QD1 pair in panel (d).

agree with (4.19). The QD3:QD1 subsystem, where the excited QD has a smaller coupling value, exhibits the boost of the population of the $|A\rangle$ state described previously, as shown in Fig. 4.7c. Contrast this with the QD2:QD1 subsystem, Fig. 4.7d, which does not experience the boost, since the excited QD has a larger coupling. After the pulse concludes, the $|S\rangle$ state undergoes a similar evolution, but the $|A\rangle$ state is different. In the QD3:QD1 subsystem the $|A\rangle$ state increases after the

Table 4.2: Summary of optimization run results for a laser pulse interacting with a system composed of two and three quantum dots. An “ f ” denotes that the parameter value was fixed and therefore not optimized over.

	Two QDs	Three QDs, (1)	Three QDs, (2)
$\hbar g_1$ (meV)	12.8	14.6	19.0
$\hbar g_2$ (meV)	24.9	19.3	16.3
$\hbar g_3$ (meV)	—	19.3	21.7
F (nJ/cm ²)	263.4	587.0	603.4
τ (fs)	12.5	36.4	39.4
$\hbar\gamma_d$ (meV)	0	0.2 ^{<i>f</i>}	0.2 ^{<i>f</i>}
$\hbar\gamma_s$ (meV)	186	180	108
Figure	Fig. 4.4	Fig. 4.6	Fig. 4.7
Max. bipartite conc.	0.60	0.34	0.35

pulse has concluded, but in the QD2:QD1 subsystem the $|A\rangle$ state only decreases. As a result, the QD3:QD1 concurrence ends up greater than the QD2:QD1 state, even though the populations of QD2 and QD3 end up at similar values.

We note that the Rabi-flop mechanism of Eq. (4.19) singles out one QD (the one undergoing $m - \frac{1}{2}$ Rabi flops) to become strongly entangled with all other QDs, while the other two QDs become strongly entangled only with the excited QD and become weakly entangled with each other. This is an inherent limit of the prescription described. Remarkably, entanglement between the two approximate ground state QDs reaches the level that it does, even for identical QDs (i.e., a concurrence of 0.1 in Fig. 4.6), but the entanglement is still much smaller than the entanglement they share with the excited QD. Since the pulse approximately prepares the same state studied in Sec. 4.3.2 and the Rabi-flop mechanism can be used for N quantum dots, we can again project onto a (low-fidelity) approximate W-state, where all pairs of QDs share the same amount of bipartite entanglement. This approach is more experimentally feasible than having a previously excited QD, but the bipartite concurrence values will be lower than those of Sec. 4.3.2.

4.4 Concluding Remarks

We provide a detailed explanation of the origins and optimization of bipartite (or pairwise) entanglement in two, three, and an arbitrary number of QDs coupled to a plasmonic system. We analyze systems with an initially excited state as well as initially unexcited systems excited by a laser pulse. We vary the QD-plasmon coupling values (which represent a QD's distance from the plasmonic system), as well the femtosecond pulse parameters and dephasing rates, in order to explore entanglement generation. By utilizing the full density matrix master equation, we are able to study the entanglement (via concurrence) of many different systems.

In the case of two QDs, two mechanisms are identified as the source of the entanglement generation: the differing decay rates of the $|S\rangle$ and $|A\rangle$ states (previously identified) [30] and a new mechanism involving an indirect coupling between the $|S\rangle$ and $|A\rangle$ states that leads to a boost in the $|A\rangle$ state population. With no dephasing or decay, high degrees of entanglement can be generated by having near-unity populations of either the $|A\rangle$ or $|S\rangle$ states. When plasmon decay is added, however, the entanglement generated from $|A\rangle$ is much higher than that of $|S\rangle$. A simple analysis including plasmon decay but neglecting QD dephasing predicts that the asymptotic concurrence is maximized when $g_2/g_1 = \sqrt{3}$ in the dark case; calculations show that this relation is still useful when QD dephasing is considered.

The two entanglement-generating mechanisms are most apparent when the system is initially prepared with equal amounts of $|S;0\rangle$ and $|A;0\rangle$, which is most easily achieved by having one excited QD and the other QD in the ground state. This dark case may be contrasted with attempts to generate entanglement in initially unexcited systems by using laser pulses. On the basis of optimization, we

find that only certain sets of parameters generate an analog to the dark case. In particular, certain rational values of the ratio of the QD-plasmon couplings, g_i/g_j , lead to results comparable to the dark case. These ratios can be understood by analyzing the underlying Rabi flops of the component QDs; the target final state, after the pulse, consists of one QD excited and the other QD in the ground state. To achieve this, one QD undergoes $m - \frac{1}{2}$ Rabi oscillations, leaving it in an approximate excited state, while the other QD undergoes n full oscillations, leaving it in an approximate ground state. This method will work for any pair of QDs, even if that pair is part of a larger system of N QDs.

In the case of three QDs, we optimize the sum of the bipartite concurrences among all of the pairs. Several local maxima corresponding to different sets of system parameters are obtained, and we present two in this paper. One (“solution 1”) was analogous to the two-QD systems discussed above, with $g_1 < g_2 = g_3$, while the other (“solution 2”) had $g_2 < g_1 < g_3$; both exhibited the entanglement generation mechanisms described above. The parameters for all three optimal systems are listed in Table 4.2. The ratios of the g_i values in the highly entangled pairs of these three-QD systems follow the simple rules derived from the Rabi-flop analysis.

We also extended our results to N QDs, with some simplifying assumptions, such as no QD population decay and a single initially excited QD. For any number of QDs, all pairs of QDs will become entangled. However, since this mechanism relies on one QD being in the excited state and the rest of the QDs being in the ground state, these mechanisms can strongly entangle only a fraction ($2/N$) of the pairs of QDs. Using the simple rules laid out in this paper for a large number of QDs results in the excited QD being strongly entangled with all other QDs, but all

the ground state QDs will be strongly entangled only with the excited QD and only weakly entangled with each other. Since all QDs share some amount of bipartite entanglement with all other QDs, the resulting state is similar to a generalized W-state and, with a measurement of the excited QD, can be projected to a state where all pairs of QDs share the same amount of bipartite concurrence (though this projected state only has 1/4 of the bipartite concurrence of a true W-state).

Additionally, this procedure could generate certain types of cluster states. A cluster state is a graph in which qubits are represented by nodes on a graph, and an edge between two nodes represents entanglement between the two qubits [77]. The W-state would be a cluster state represented by a complete, fully connected graph. An important subclass of cluster states is the star state, where a central node is connected to all other nodes (or, a single qubit is entangled to all other qubits but the other qubits are not entangled with each other). A four-qubit star cluster can be used for universal quantum computing [78]. In our model, we have an approximate star cluster for N QDs, since the initially excited QD is strongly entangled with all other QDs. Although we show N QD results only for a specific initial starting condition, we also show how this state can be prepared for N QDs from a single, ultrafast laser pulse. The rules for the ratios of the coupling strengths based on the number of Rabi flops can be used to define an appropriate set of parameters to prepare an approximate form of the specific initial starting condition studied.

The ability to fabricate systems with specific QD/plasmon coupling factors or ratios is necessary in order to realize the results discussed in this paper. These factors are related to the distances between the QDs and the plasmonic system, which are ideally less than 10 nm. While challenging, rapid progress continues in

the area of nanofabrication, e.g., in the use of DNA-based assembly methods [60,79] to generate metal nanoparticle-DNA-linker-QD systems, and so the systems we envision may well be experimentally feasible in the near future. We note that here we are not envisioning dynamical control of the QD/plasmon coupling factors during an entanglement experiment, but rather clever experimental fabrication to achieve a fixed and generally asymmetric configuration of QDs about the plasmonic system that exhibits the couplings and coupling ratios consistent with the optimal structures deduced in this paper.

Further studies of such systems that better approximate the W-state are planned, as are studies of the entanglement between all qubits of the system (rather than just pairs), which would be similar to the GHZ-state [75], which represents entanglement where all the qubits are mutually entangled with each other (rather than just sharing bipartite entanglement with other qubits). The W- and GHZ-states represent two mutually exclusive examples of multipartite entanglements and allow entanglement to be used as a quantum information resource in different ways [75]. The model presented here is reasonably general; and, while our numerical applications focused on a parameter regime and thus phenomena consistent with semiconductor nanocrystal/plasmonic systems, the approach may be relevant to other systems such as QDs coupled to other types of resonators or even nitrogen vacancies in diamond [80] and superconducting qubits [81].

CHAPTER 5
CONCLUSION

Quantum mechanics was one of the marquee achievements of 20th century physics. Even though the theory is reaching a century in age, there are still many interesting problems to be investigated, both experimentally and theoretically. The use of computers for solving problems and quantum mechanics has greatly increased its scope. Previously, clever theoretical approximations were necessary to solve problems. With computers, previously intractable problems became accessible with clever computational techniques.

Heat bath configuration interaction represents a fast algorithm capable of obtaining the exact answer for the time independent Schrödinger equation for certain small, interesting problems. In some systems, like Cr₂, this accuracy is necessary to fully describe the physics.

The Lindblad master equation allows for the solution of the time dynamics of open quantum systems. Many of these lossy systems can have interesting dynamics that exist solely because of the dissipative nature of the system. One such case is plasmonically coupled quantum dots, where the dissipation in the plasmonic system leads to an entangled state in the quantum dots.

In both the fields of electronic structure and quantum dynamics of open systems, computers have been fundamental in solving interesting problems. In many cases, clever approximations can allow access to the interesting physics at a reasonable cost. There are systems, however, where those approximations can fail, requiring expensive, exponential algorithms; in those cases, careful implementation and understanding of the underlying physics can allow access to problems previously seen as inaccessible. Further advancements in algorithms, classical computers, and even the rise of quantum computers, will allow problems which seem impractical today to be done with relative ease.

APPENDIX A
APPENDIX FOR “PARALLELIZATION AND APPLICATIONS OF
HEAT-BATH CONFIGURATION INTERACTION”

A.1 Efficient Generation of Hamiltonian Matrix

The elements, $\langle i|\hat{H}|j\rangle$, of the Hamiltonian matrix must be calculated where i and j are determinants. Due to the structure of the quantum chemistry Hamiltonian, determinants which differ by more than two excitations will have 0 as the matrix element. Though checking every determinant against every other determinant would eventually construct the Hamiltonian, it would be slow, since most pairs of determinants differ by more than two excitations. To avoid checking all pairs of determinants, we developed an algorithm in which we first construct some auxiliary arrays that enable us to check a much smaller number of determinant pairs. Recently, Sandeep Sharma at Colorado and Junhao Li in our group have developed a way of constructing auxiliary arrays which further speeds up the generation of the Hamiltonian, so it is this new algorithm that is described here.

A.1.1 Key Variables

The auxiliary arrays or “helpers” consist of look up tables (which can be either binary search trees or hash maps) and arrays of arrays. `alpha(beta)ToId` is the lookup table from an α or β string to a unique id representing it. `alphaIdToDetIds` and `alphaIdToBetaIds` are arrays of arrays going from an α id to the ids of the determinants with that alpha and the corresponding beta ids respectively. `alphaMinusOneToIds` is a lookup table from an $(\alpha - 1)$ string, an α string with one electron missing, to the ids of other α string that can give that $(\alpha - 1)$. `alphaIdToSingleIds` is an array of arrays from an α id to other α ids that connect to it by single excitations. The β strings are similarly defined.

In this section, we describe the algorithm in the format of pseudocode for fast

hamiltonian generation during the variational stage. The algorithm is as follows:

A.1.2 Setup

```
// Generate helper lists.
for each det of new variational dets:
  let alpha/beta be the up/down spin part of the det
  let detId be the id of the det.

  // Update alphaToId if new.
  if alpha exists in alphaToId:
    set alphaId = alphaToId[alpha]
  else
    set alphaId = number of items in alphaToId
    set alphaToId[alpha] = alphaId
  // Update betaToId similarly.
  ...

  // Update alphaIdToBetaIds and alphaIdToDetIds.
  add betaId to the alphaIdToBetaIds[alphaId] list
  add detId to the alphaIdToDetIds[alphaId] list
  add alphaId to the updatedAlphaIds set.
  // Update betaIdToAlphaIds and betaIdToDetIds similarly.
  ...

  // Update alphaMinusOneToIds.
  for each alphaMinusOne from alpha (by removing one electron from
  ):
    add alphaId to alphaMinusOneToIds[alphaMinusOne]
  // Update betaMinusOneToIds similarly.
  ...

for each alphaId in the updatedAlphaIds set:
  sort alphaIdToBetaIds[alphaId] and alphaIdToDetIds [alphaId] together
  by alphaIdToBetaIds[alphaId] into ascending order of beta ids.
clear updatedAlphaIds.
// Do the same thing for updatedBetaIds.
...

for each det of all variational dets (loop in reverse order):
  let alpha/beta be the up/down spin part of the det
  set alphaId = alphaToIds[alpha]
  set betaId = betaToIds[beta]

  // Construct alphaIdToSingleIds.
  if updatedAlphaIds set does not have alphaId:
    for each alphaMinusOne from alpha (by removing one electron from
    alpha):
      for each alphaSingleId from alphaMinusOneToIds[alphaMinusOne]:
```

```

        if alphaSingleId equals alphaId, go to the next alphaSingleId.
        if det is new and alphaSingleId exists in updatedAlphaIds:
            go to the next alphaSingleId.
        add alphaSingleId to alphaIdToSingleIds[alphaId]
        add alphaId to alphaIdToSingleIds[alphaSingleId]
        add alphaId into updatedAlphaIds.
    // Construct betaIdToSingleIds similarly.
    ...

for each alphaId in the updatedAlphaIds set:
    sort alphaIdToSingleIds[alphaId] into ascending order.
clear updatedAlphaIds.
// Do the same thing for updatedBetaIds
...

clear alphaMinusOneToIds and betaMinusOneToIds

```

A.1.3 Constructing the Hamiltonian

```

// Generate sparse hamiltonian.
for each det of all the variational dets:
    let alpha/beta be the up/down spin part of the det
    let detId be the id of the det
    set alphaId = alphaToIds[alpha]
    set betaId = betaToIds[beta]

    if det is a new determinant:
        let compute diagonal hamiltonian matrix element H of det
        add (detId, H) into sparseHamiltonian[detId].

    set startId to detId + 1 if it is a new determinant,
        otherwise set it to previous number of determinants.

    // Find single or double alpha excitation.
    for each connectedDetId in betaIdToDetIds[betaId]:
        if connectedDetId < startId) go to the next connectedDetId.
        let connectedDet be the determinant with id connectedDetId.
        compute hamiltonian matrix element H between det and connectedDet
        if H is not 0, add (connectedDetId, H) into sparseHamiltonian[detId
        ].
    // Find single or double beta excitation similarly.
    ...

    // Find mixed double excitations.
    for each alphaSingleId from alphaIdToSingleIds[alphaId]:
        let relatedBetaIds = alphaIdToBetaIds[alphaSingleId]
        let relatedDetIds = alphaIdToDetIds[alphaSingleId]
        set ptr = 0

```

```

for each betaSingleId from betaIdToSingleIds[betaId]:
  let relatedBetaId = relatedBetaIds[ptr]
  while ptr < length of relatedBetaIds and relatedBetaId <
betaSingleId:
    increase ptr by one
  if ptr equals length of relatedBetaIds:
    exit the loop and go to the next alphaSingleId
  if relatedBetaId equals betaSingleId:
    let relatedDetId = relatedDetIds[ptr]
    increase ptr by one
    if relatedDetId < startId, go to the next betaSingleId.
    let relatedDet be the determinant at id relatedDetId
    compute hamiltonian matrix element H between det and relatedDet
    if H is not 0, add (relatedDetId, H) into sparseHamiltonian[
detId].

```

```

clear alphaIdToSingleIds and betaIdToSingleIds

```

APPENDIX B

SUPPORTING MATERIAL FOR “ENTANGLEMENT OF TWO,
THREE, OR FOUR PLASMONICALLY COUPLED QUANTUM
DOTS”

B.1 Quantum Master Equation

We model N_D quantum dots in close proximity to a plasmonic system following a formalism directly generalized from previous work on just one QD interacting with a plasmonic system [50]. The quantum dot states are given by $|q\rangle = |q_{N_D}, \dots, q_1\rangle$, where $q_i \in \{0, 1\}$ indexes the exciton in QD i and i ranges from 1 to N_D . The plasmon states are given by $|s\rangle$ where $s \in \{0, 1, 2, \dots, N_s\}$ indexes plasmon energy levels. We truncate the set of plasmon quanta at a value N_s beyond which there is no significant occupancy during the dynamics. N_s depends on the fluence; we have found, heuristically, that using $N_s \geq 0.11F$, where F is the fluence in nanojoules, provides converged results. Results presented both here and in the main text used at least two times more than the heuristic minimum. At any time t , the system is described by the density operator $\hat{\rho}(t)$, which may be decomposed as

$$\hat{\rho}(t) = \sum_{qs} \sum_{q's'} \rho_{q,s,q',s'}(t) |q\rangle |s\rangle \langle q'| \langle s'| \quad . \quad (\text{B.1})$$

The density matrix ρ is formed from the matrix elements $\rho_{qs,q',s'} = \langle q; s | \hat{\rho} | q'; s' \rangle$ in Eq. B.1. The density matrix describes a quantum system in a mixed state; that is a statistical ensemble of pure quantum states. In this Letter we consider a single quantum system; in this case, the statistical ensemble corresponds to repeated measurements on the same system initialized each time in the same starting state.

The density operator satisfies the quantum master or Liouville equation

$$\frac{d\hat{\rho}}{dt} = -\frac{i}{\hbar} [\hat{H}\hat{\rho}] + L(\hat{\rho}) \quad (\text{B.2})$$

in which \hat{H} is the Hamiltonian for the driven coupled system and $L(\hat{\rho})$ is a Lindblad superoperator providing dephasing and dissipation. More explicitly

$$\hat{H} = \sum_i \hat{H}_i + \hat{H}_s + \hat{H}_d + \sum_i \hat{H}_{si} . \quad (\text{B.3})$$

In terms of the lowering and raising operator pairs for the QDs and plasmon ($\hat{\sigma}_i, \hat{\sigma}_i^\dagger$), and (\hat{b}, \hat{b}^\dagger), the uncoupled QD and plasmon Hamiltonian operators given above are

$$\hat{H}_i = \hbar\omega_i \hat{\sigma}_i^\dagger \hat{\sigma}_i \quad \hat{H}_s = \hbar\omega_s \hat{b}^\dagger \hat{b} . \quad (\text{B.4})$$

The driving term or coupling to the electric field $E(t)$ is given by

$$\hat{H}_d = -E(t)\hat{\mu} \quad (\text{B.5})$$

where the total dipole operator is $\hat{\mu} = \sum_i \hat{\mu}_i + \hat{\mu}_s$ and the individual dipole operators are $\hat{\mu}_i = d_i(\hat{\sigma}_i + \hat{\sigma}_i^\dagger)$ and $\hat{\mu}_s = d_s(\hat{b} + \hat{b}^\dagger)$ with d_i , and d_s denoting transition dipole moments of the QDs and plasmon respectively. Each QD couples with the plasmon via

$$\hat{H}_{si} = -\hbar g_i (\hat{\sigma}_i^\dagger \hat{b} + \hat{\sigma}_i \hat{b}^\dagger) , \quad (\text{B.6})$$

which is consistent with dipole-dipole coupling between the QD and plasmon. We assume that the distance between QDs is large compared to the separation between QDs and neighboring metal nanoparticles so that direct through-space coupling among the QDs can be neglected.

The Lindblad superoperator is taken to be the N_D extension of the $N_D = 1$ case of Ref. [50]; it is parameterized by QD population (or spontaneous emission) and dephasing decay constants γ_{pi} and γ_{di} , and the plasmon decay constant γ_s .

$L(\hat{\rho}) = \sum_i L_i(\hat{\rho}) + L_s(\hat{\rho})$ treats dissipation in the system. Dissipation in QD i is described by

$$L_i(\hat{\rho}) = -\frac{\gamma_{pi}}{2}(\hat{\sigma}_i^\dagger \hat{\sigma}_i \hat{\rho} + \hat{\rho} \hat{\sigma}_i^\dagger \hat{\sigma}_i - 2\hat{\sigma}_i \hat{\rho} \hat{\sigma}_i^\dagger) - \gamma_{di}(\hat{\sigma}_i^\dagger \hat{\sigma}_i \hat{\rho} + \hat{\rho} \hat{\sigma}_i^\dagger \hat{\sigma}_i - 2\hat{\sigma}_i^\dagger \hat{\sigma}_i \hat{\rho} \hat{\sigma}_i^\dagger \hat{\sigma}_i) \quad (\text{B.7})$$

which describes exciton population relaxation and dephasing with rates $\gamma_{pi} = T_1^{-1}$ and $\gamma_{di} = T_2^{-1}$ respectively. Plasmon dissipation with rate γ_s is described by

$$L_s(\hat{\rho}) = -\frac{\gamma_s}{2}(\hat{b}^\dagger \hat{b} \hat{\rho} + \hat{\rho} \hat{b}^\dagger \hat{b} - 2\hat{b} \hat{\rho} \hat{b}^\dagger) \quad (\text{B.8})$$

which does not include a pure dephasing term such as the Lindblad superoperators for the QDs because plasmons have such a short lifetime that additional thermal dephasing is negligible.

While rather abstract in appearance the matrix elements of the Lindblad operators above are readily constructed using raising and lowering operators and take on relatively simple forms; see e.g., the Supplementary Material of Ref. [50].

The Hamiltonian $\hat{H} - \hat{H}_d$ i.e., Eq. (3) in the absence of driving laser field, has a relatively simple energy level structure in the case of two QDs interacting with a plasmon, as shown in Fig. B.1. In this case we can define coupled QD states $|S\rangle = \frac{1}{\sqrt{2}}(|q_2 = 1, q_1 = 0\rangle + |q_2 = 0, q_1 = 1\rangle)$ and $|A\rangle = \frac{1}{\sqrt{2}}(|q_2 = 1, q_1 = 0\rangle - |q_2 = 0, q_1 = 1\rangle)$, as in the main text. The full QD-plasmon states of this Hamiltonian may be expanded in terms of product states of the form $|QDs\rangle |s\rangle$ where $|s\rangle$ denotes the surface plasmon states $s = 0, 1, \dots$, and $|QDs\rangle = |q_2 = 0, q_1 = 0\rangle, |S\rangle |A\rangle$, and $|q_2 = 1, q_1 = 1\rangle$. It turns out that then the $|A\rangle |s\rangle$ states are already eigenstates of this Hamiltonian. Hence when the full-density-matrix dynamics are considered, these states decay at the relatively slow dephasing rate γ_d , due to loss of mutual coherence between the two QDs. The $|S\rangle |s\rangle$ states are degenerate with the $|A\rangle |s\rangle$ states in the limit of $g = 0$ i.e., no QD-plasmon coupling. However, for finite

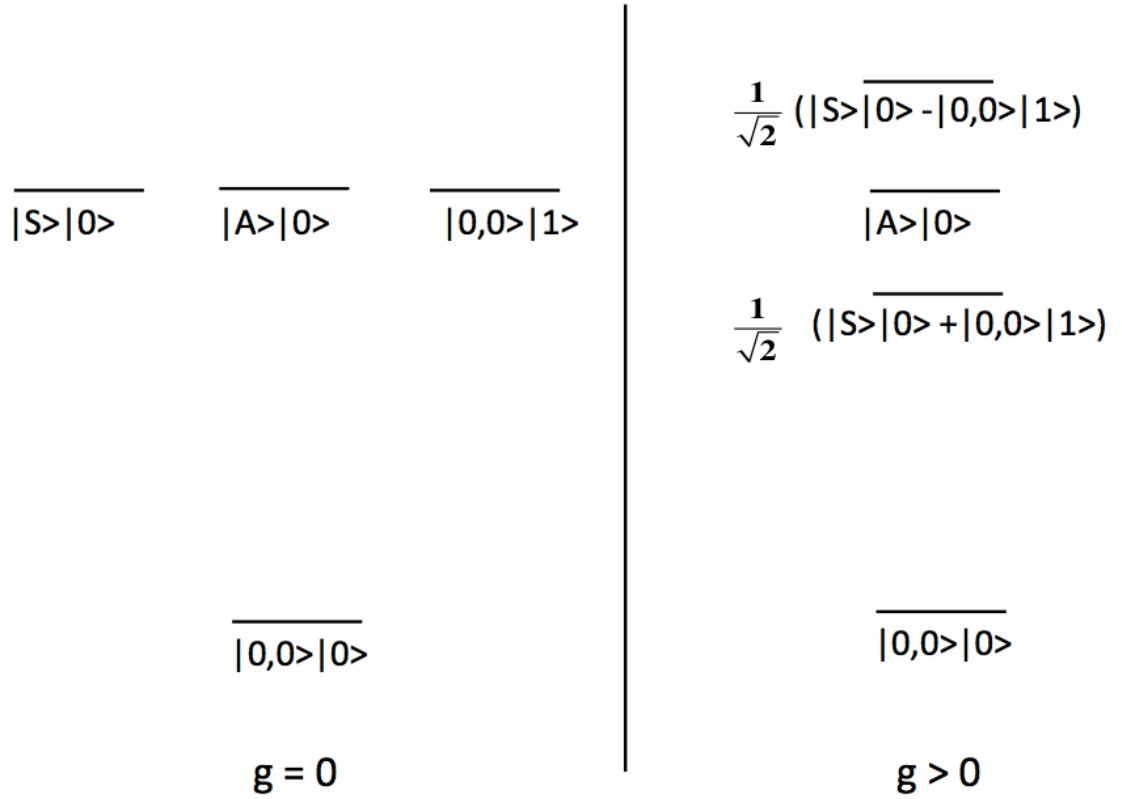


Figure B.1: Uncoupled ($g = 0$) and coupled ($g > 0$) QD/plasmon level structure for the case of two QDs interacting with a plasmon. The kets correspond to products of two-QD ($|0, 0\rangle$, $|S\rangle$, $|A\rangle$) and plasmon ($|0\rangle$, $|1\rangle$) states. The $|S\rangle|0\rangle$ and $|0, 0\rangle|1\rangle$ states mix and split relative to the $|A\rangle|0\rangle$ state, by energies $\pm \sqrt{2}\hbar g$.

g the $|S\rangle|s\rangle$ states interact with $|q_2 = 0, q_1 = 0\rangle|s + 1\rangle$ and $|q_2 = 1, q_1 = 1\rangle|s - 1\rangle$ states, leading to eigenstates with energies above and below the $|A\rangle|s\rangle$ state. For $s = 0$ only the $|S\rangle|0\rangle$ and $|00\rangle|1\rangle$ states mix, leading to eigenstates $|\psi_+\rangle = \frac{1}{\sqrt{2}}(|S\rangle|0\rangle + |00\rangle|1\rangle)$ and $|\psi_-\rangle = \frac{1}{\sqrt{2}}(|S\rangle|0\rangle - |00\rangle|1\rangle)$, with energies $-\sqrt{2}\hbar g$ and $+\sqrt{2}\hbar g$ respectively, relative to the energy of the $|A\rangle|0\rangle$ eigenstate.

This simple energy-level structure can provide some additional insight particularly into the dark state dynamics. For example if one considers one excited quantum dot as an initial condition i.e. $|q_2 = 0, q_1 = 1\rangle|0\rangle$, it follows that subsequent evolution of the state is into a superposition of $|A\rangle|s = 0\rangle$, $|\psi_+\rangle$ and $|\psi_-\rangle$.

The probability of being in the symmetric state $|S\rangle|0\rangle$ is then readily found to be $\frac{1}{2}\cos^2(\sqrt{2}gt)$ which leads to a significantly faster initial decay than the Purcell lifetime and is approximately consistent with P_S in Fig. 1(b) of the main text. Adding plasmon decay to the analysis will damp out any subsequent oscillations.

B.2 Concurrence

In the main text we quantify the degree of entanglement at any particular instant in time using Wootters' concurrence, C [54]. The concurrence is an entanglement measure based on generalization of the entropy of entanglement. Unlike entropy of entanglement however, concurrence can be used to characterize mixed states and not only pure quantum states. The concurrence satisfies the conditions required for a measure of entanglement. For example $C = 1$ implies perfect entanglement whereas $C = 0$ implies complete separability (i.e. that ρ' can be decomposed as the product of density matrices of two subsystems). In addition, concurrence does not increase under local operations with classical communication. A system with larger values of C can thus be said to be “more entangled” than a system with smaller C . Other entanglement measures could equally well be used and would provide essentially the same physical information.

Let ρ' be a reduced density matrix associated with just one particular pair of quantum dots A and B . It is obtained by tracing over the plasmon quantum numbers s and those for all other QDs. Explicitly, ρ' has matrix elements

$$\rho'_{mn,m',n'} = \sum_q \sum_s \langle q_D \dots, q_1 \text{ s.t. } q_A = m, q_B = n; s | \hat{\rho} | q_D \dots, q_1 \text{ s.t. } q_A = m', q_B = n'; s \rangle \quad (\text{B.9})$$

where the prime on the first summation implies a sum over all QD quantum numbers except those for QDs A and B that are fixed at the appropriate values indicated in the bra and ket vectors. The AB pairwise concurrence is then

$$C = \max[0, \lambda_1 - \lambda_2 - \lambda_3 - \lambda_4] \quad , \quad (\text{B.10})$$

where λ_i are the square roots (in descending order) of the eigenvalues of $\rho' \tilde{\rho}'$. The matrix $\tilde{\rho}'$ corresponds to the spin-flipped density matrix [54]

$$\tilde{\rho}' = (\sigma_y \otimes \sigma_y) (\rho')^* (\sigma_y \otimes \sigma_y) \quad (\text{B.11})$$

with

$$(\sigma_y \otimes \sigma_y) = \begin{pmatrix} 0 & 0 & 0 & -1 \\ 0 & 0 & 1 & 0 \\ 0 & 1 & 0 & 0 \\ -1 & 0 & 0 & 0 \end{pmatrix} . \quad (\text{B.12})$$

B.3 Numerical Aspects

The matrix representation of Eq. B.2 $\langle q | \langle s | d\hat{\rho}/dt | q' \rangle | s' \rangle = d\rho_{qs,q',s'}/dt$, is a set of $n \times n$ complex differential equations with $n = 2^{N_D} N_s$. As in Ref. [50], the

rotating wave approximation is applied, which removes the stiff character of these equations. High intensities of the incident field $E(t)$ cause N_s to become large, which can make the number of equations prohibitively large. We use an efficient solver based on sparse matrix-matrix multiplication algorithms along with both Runge-Kutta (RK45) and exponential time integration schemes [51,52]. Typically this corresponds to the solution of tens of thousands of coupled ordinary differential equations for the cases considered here.

B.4 Concurrence Results for Different Parameter Choices

B.4.1 Dark Results with Smaller Couplings

Fig. B.2 shows the results of simulations analogous to those of Fig. (1) in the main text but with weaker coupling strengths. Even with couplings far weaker than the 30 meV coupling presented in the main text the concurrence still reaches significant values, though the maximum concurrence does decrease with decreasing $\hbar g$.

B.4.2 Pulsed Results with Smaller Couplings

Fig. B.3 shows simulations of several different systems with couplings smaller than those in the text. These results show that significant concurrence can be obtained with smaller coupling strengths than the results presented in the main text for both two-QD and three-QD systems. Furthermore, additional parameters such as the pulse duration and the QD dephasing rate, could be varied in order to obtain larger values of concurrence while keeping the coupling strengths small; this is part

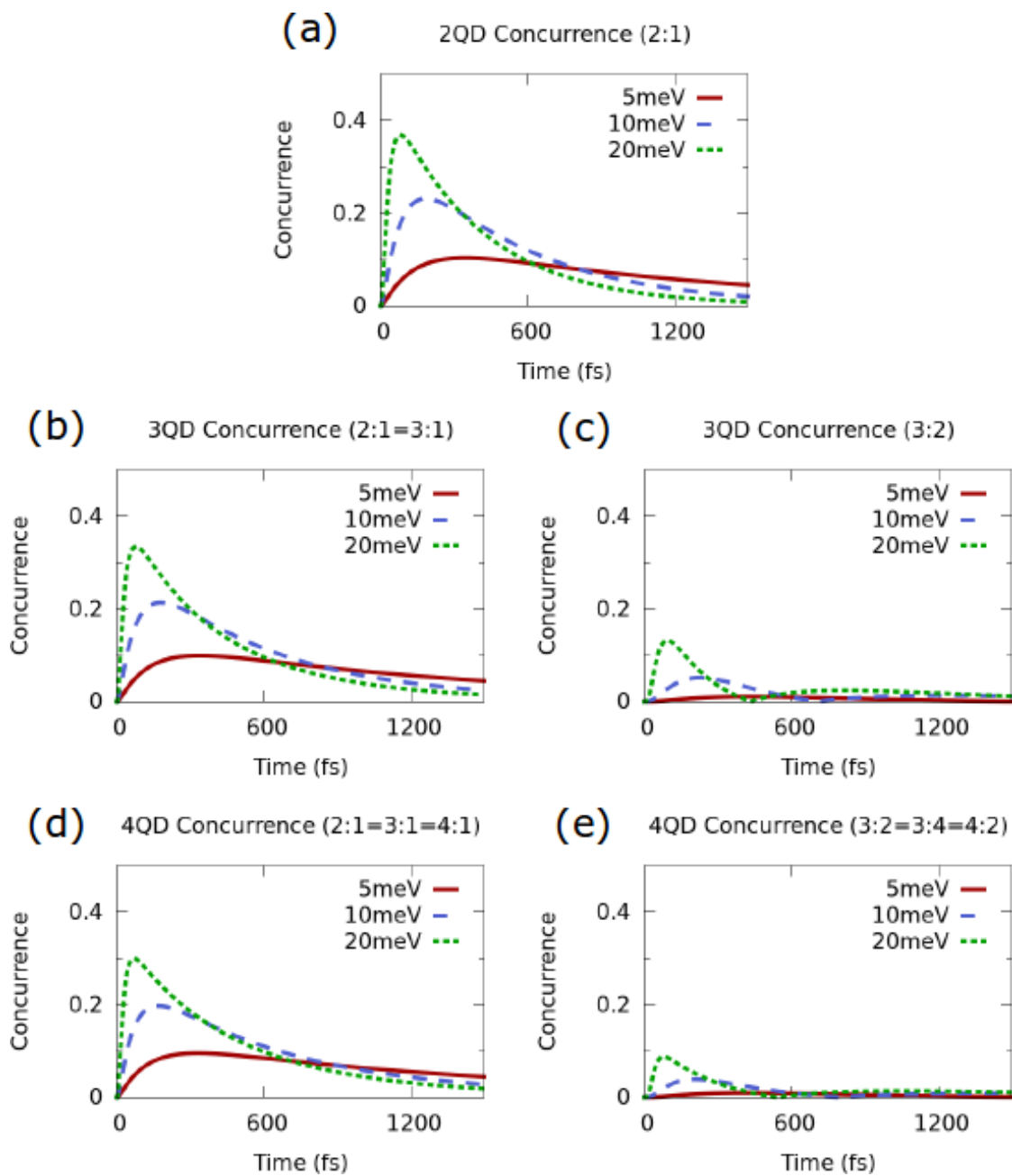


Figure B.2: Concurrence as a function of time with QD1 initially excited, no laser, and various exciton-plasmon coupling strengths $\hbar g$, for different numbers of quantum dots. $i:j$ refers to the concurrence between QD i and QD j .

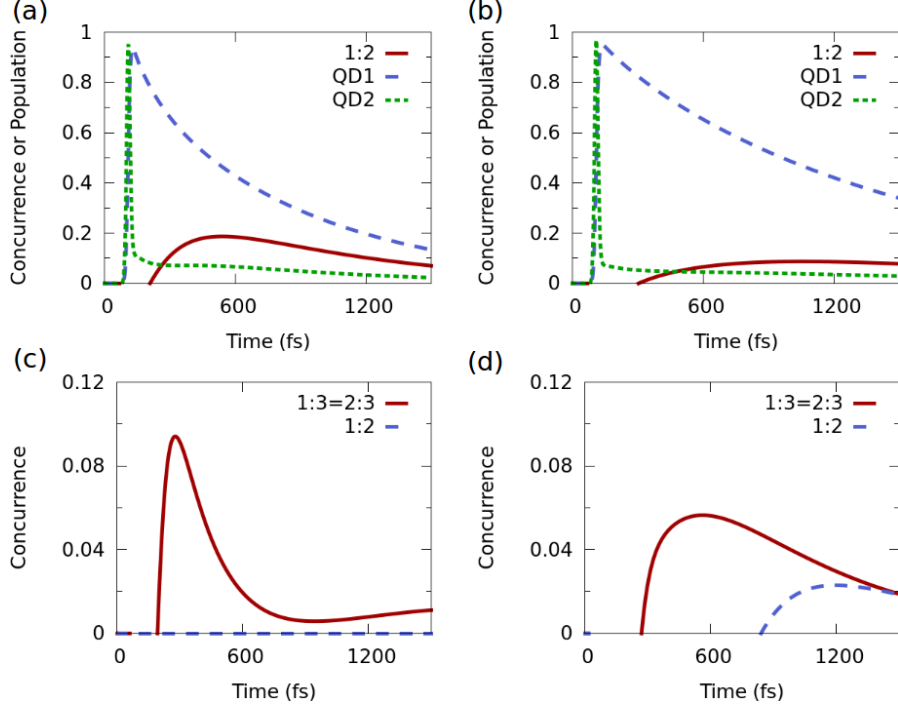


Figure B.3: Concurrence as a function of time with various coupling strengths and laser intensities. (a) Concurrence for a two-QD system with $\hbar g_1 = 8$ meV, $\hbar g_2 = 15$ meV, and a laser fluence of 298 nJ/cm². (b) Concurrence for a two-QD system with $\hbar g_1 = 5$ meV, $\hbar g_2 = 10$ meV, and a laser fluence of 662 nJ/cm². (c) Concurrence for a three-QD system with $\hbar g_1 = \hbar g_2 = 10.4$ meV, $\hbar g_3 = 24.8$ meV, and a laser fluence of 124 nJ/cm². (d) Concurrence for a three-QD system with $\hbar g_1 = \hbar g_2 = 14.8$ meV, $\hbar g_3 = 20$ meV, and a laser fluence of 293 nJ/cm². Note that in (c) and (d) both QD1 and QD2 play the role of the excited quantum dot.

of our ongoing work.

B.4.3 Quantum Dots with Different Energy Levels

Fig. B.4 shows the concurrence as a function of time for the optimal two-QD case presented in the main text (Fig. 2(b)) but with different amounts of detuning in the energy levels of the quantum dots. The optimal case where $\hbar\omega_1 = \hbar\omega_2 = 2.05$ eV, achieves a max concurrence of around 0.35. Small differences in $\hbar\omega$ on the order of

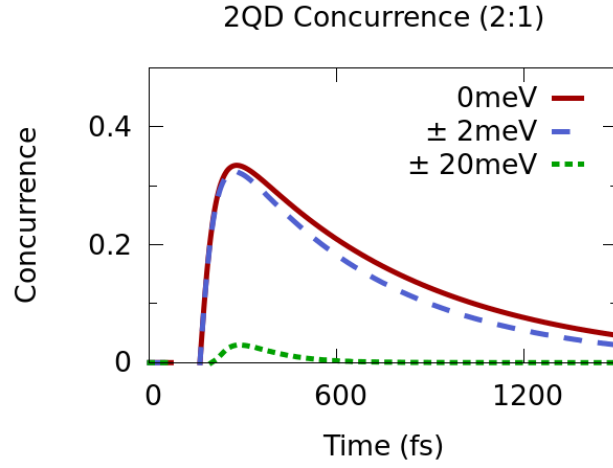


Figure B.4: Concurrence as a function of time for the coupling coefficients, $\hbar g_1 = 15$ meV and $\hbar g_2 = 30$ meV the laser-pulse fluence, 81 nJ/cm^2 and various differences in energy levels ($\hbar\omega$) for each QD.

the dephasing-induced linewidth (2 meV) have minimal effect on the concurrence profile. As the detuning grows past this point (20 meV), the maximum concurrence rapidly decreases.

APPENDIX C

SUPPORTING MATERIAL FOR “ORIGINS AND OPTIMIZATION
OF ENTANGLEMENT IN PLASMONICALLY COUPLED
QUANTUM DOTS”

C.1 Three and $N + 1$ State Models

The “dark” problem, namely, to determine the dynamics of N QDs and a plasmonic system that results from a given initial condition without any applied laser pulse, can be solved analytically if the initial condition is not too energetic and QD dephasing is neglected. An example is a system in which there is just one quantum of excitation within the QD manifold and a cold plasmonic system. The analytical solution is made possible because under such conditions a time-dependent Schrödinger equation involving an effective, non-Hermitian Hamiltonian can be employed and the latter can be represented by an $(N + 1) \times (N + 1)$ matrix with a simple structure. We first illustrate such a solution in detail for the case of $N = 2$. We then present the general $N + 1$ state solution.

For two QDs interacting with a plasmonic system, we wish to solve for the time evolution of $|\Psi(t)\rangle$ satisfying

$$i\hbar \frac{\partial}{\partial t} |\Psi(t)\rangle = \hat{H} |\Psi(t)\rangle, \quad (\text{C.1})$$

where

$$\begin{aligned} |\Psi(t)\rangle = & c_0(t) |q_2 = 0, q_1 = 0; s = 1\rangle \\ & + c_S(t) |S; s = 0\rangle + c_A(t) |A; s = 0\rangle. \end{aligned} \quad (\text{C.2})$$

We refer to the three states $|q_2 = 0, q_1 = 0; s = 1\rangle$, $|S; s = 0\rangle$, and $|A; s = 0\rangle$ as the zero-order basis. This limited basis is adequate for describing an initial condition that involves any superposition of these three states, such as the case of one QD being excited and the plasmonic system and other QD being cold. With the definitions of the basis states in the text, (4.1), (4.12), and (4.13), and the Hamiltonian operator, (4.4), the corresponding 3×3 Hamiltonian matrix of the zero-order basis

representation is

$$\mathbf{H} = \hbar \begin{bmatrix} \omega_0 & \alpha & \beta \\ \alpha & \omega_0 - i\epsilon & 0 \\ \beta & 0 & \omega_0 \end{bmatrix}. \quad (\text{C.3})$$

The QD and plasmon transition frequencies are assumed to be equal, $\omega_1 = \omega_2 = \omega_s$, the coupling between $|0, 0; 1\rangle$ and $|S; 0\rangle$ is

$$\alpha = \frac{1}{\sqrt{2}}(g_1 + g_2), \quad (\text{C.4})$$

and the coupling between $|0, 0; 1\rangle$ and $|A; 0\rangle$ is

$$\beta = \frac{1}{\sqrt{2}}(g_1 - g_2). \quad (\text{C.5})$$

We assume no direct coupling between $|S; 0\rangle$ and $|A; 0\rangle$. Notice that in (C.3), we have added an imaginary part $-i\epsilon$ to the diagonal matrix element associated with $|0, 0; 1\rangle$. With $\epsilon = \gamma_s/2$ this term represents the dissipative loss of the plasmonic system.

Introducing the more slowly varying coefficient vector

$$\begin{bmatrix} a_0(t) \\ a_S(t) \\ a_A(t) \end{bmatrix} = \exp(i\omega_0 t) \begin{bmatrix} c_0(t) \\ c_S(t) \\ c_A(t) \end{bmatrix}, \quad (\text{C.6})$$

(C.1) leads to

$$\frac{d}{dt} \begin{bmatrix} a_0(t) \\ a_S(t) \\ a_A(t) \end{bmatrix} = -i\mathbf{W} \begin{bmatrix} a_0(t) \\ a_S(t) \\ a_A(t) \end{bmatrix}, \quad (\text{C.7})$$

where

$$\mathbf{W} = \begin{bmatrix} 0 & \alpha & \beta \\ \alpha & 0 & 0 \\ \beta & 0 & 0 \end{bmatrix}. \quad (\text{C.8})$$

The solution of (C.7) is thus

$$\begin{bmatrix} a_0(t) \\ a_S(t) \\ a_A(t) \end{bmatrix} = \exp(-i\mathbf{W}t) \begin{bmatrix} a_0(0) \\ a_S(0) \\ a_A(0) \end{bmatrix}. \quad (\text{C.9})$$

In the limit (assuming no plasmon dissipation, $\epsilon = 0$), expanding the exponential and re-grouping terms, (C.9) can be written more explicitly as

$$\begin{bmatrix} a_0(t) \\ a_S(t) \\ a_A(t) \end{bmatrix} = \begin{bmatrix} a_0(0) \\ a_S(0) \\ a_A(0) \end{bmatrix} + \left(\begin{bmatrix} \eta^2 & 0 & 0 \\ 0 & \alpha^2 & \alpha\beta \\ 0 & \alpha\beta & \beta^2 \end{bmatrix} \frac{F(t)}{\eta^2} - i\mathbf{W} \frac{G(t)}{\eta} \right) \begin{bmatrix} a_0(0) \\ a_S(0) \\ a_A(0) \end{bmatrix}, \quad (\text{C.10})$$

where

$$\eta = \sqrt{\alpha^2 + \beta^2} \quad (\text{C.11})$$

and

$$F(t) = \cos(\eta t) - 1, \quad G(t) = \sin(\eta t). \quad (\text{C.12})$$

Note that for the initial condition corresponding to $|\Psi(t=0)\rangle = |q_2 = 0, q_1 = 0; s = 0\rangle$ or $a_0(0) = 0, a_S(0) = a_A(0) = \frac{1}{\sqrt{2}}$, the above exact solution (for $\epsilon = 0$) is such that $a_0(t)$ is a purely imaginary number for all times and that $a_S(t)$ and $a_A(t)$ are purely real numbers for all times. Equation (C.10), can be approximated to various orders in time by expanding $F(t)$ and $G(t)$ defined in (C.12) appropriately. Thus, with the initial condition $|\Psi(t=0)\rangle = |q_2 = 0, q_1 = 1; s = 0\rangle$,

the approximate solution, accurate to second order in time, is

$$\begin{bmatrix} a_0(t) \\ a_S(t) \\ a_A(t) \end{bmatrix} \approx \begin{bmatrix} -i\frac{(\alpha+\beta)t}{\sqrt{2}} \\ \frac{1}{\sqrt{2}} - \frac{(\alpha^2+\alpha\beta)t^2}{2\sqrt{2}} \\ \frac{1}{\sqrt{2}} - \frac{(\beta^2+\alpha\beta)t^2}{2\sqrt{2}} \end{bmatrix}, \quad (\text{C.13})$$

or, in terms of g_1 and g_2 ,

$$\begin{bmatrix} a_0(t) \\ a_S(t) \\ a_A(t) \end{bmatrix} \approx \begin{bmatrix} -ig_1t \\ \frac{1}{\sqrt{2}} - \frac{g_1(g_1+g_2)t^2}{2\sqrt{2}} \\ \frac{1}{\sqrt{2}} + \frac{g_1(g_2-g_1)t^2}{2\sqrt{2}} \end{bmatrix}. \quad (\text{C.14})$$

Of course, another way to obtain (C.10) is to determine the eigenvalues and eigenvectors of \hat{W} , w_k and $|\phi_k\rangle$, $k = 1, 2, 3$, and represent (C.9) with them. This procedure can be carried out exactly even when plasmonic dissipation is allowed ($\epsilon > 0$). The eigenvalues of \mathbf{W} are easily found to be

$$\begin{aligned} w_1 &= 0 \\ w_2 &= \frac{1}{2}(-i\epsilon - \sqrt{4\alpha^2 + 4\beta^2 - \epsilon^2}) \\ w_3 &= \frac{1}{2}(-i\epsilon + \sqrt{4\alpha^2 + 4\beta^2 - \epsilon^2}), \end{aligned} \quad (\text{C.15})$$

and the associated (unnormalized) eigenvectors projected onto the zero-order basis are

$$\begin{bmatrix} \langle 0, 0; 1 | \phi_1 \rangle \\ \langle S; 0 | \phi_1 \rangle \\ \langle A; 0 | \phi_1 \rangle \end{bmatrix} = \begin{bmatrix} 0 \\ -\beta/\alpha \\ 1 \end{bmatrix}, \quad (\text{C.16})$$

$$\begin{bmatrix} \langle 0, 0; 1 | \phi_2 \rangle \\ \langle S; 0 | \phi_2 \rangle \\ \langle A; 0 | \phi_2 \rangle \end{bmatrix} = \begin{bmatrix} \frac{-i\epsilon - \sqrt{4\alpha^2 + 4\beta^2 - \epsilon^2}}{2\beta} \\ \alpha/\beta \\ 1 \end{bmatrix}, \quad (\text{C.17})$$

and

$$\begin{bmatrix} \langle 0, 0; 1 | \phi_3 \rangle \\ \langle S; 0 | \phi_3 \rangle \\ \langle A; 0 | \phi_3 \rangle \end{bmatrix} = \begin{bmatrix} \frac{-i\epsilon + \sqrt{4\alpha^2 + 4\beta^2 - \epsilon^2}}{2\beta} \\ \alpha/\beta \\ 1 \end{bmatrix}. \quad (\text{C.18})$$

The propagator may then be written as

$$\exp(-i\hat{W}t) = \sum_k |\phi_k\rangle \langle \phi_k^*| \exp(-iw_k t) / n_k, \quad (\text{C.19})$$

where

$$n_k = \langle \phi_k^* | \phi_k \rangle = \sum_{j=0,S,A} \langle j | \phi_k \rangle^2. \quad (\text{C.20})$$

The bra vectors we employ, $\langle c|$ (as is most common), are defined to be the transpose of the complex conjugates of the coefficients representing their corresponding kets, $|c\rangle$. Thus $\langle c|d\rangle = \sum_j c_j^* d_j$, where $c_j = \langle j|c\rangle$, $d_j = \langle j|d\rangle$. An expression such as (C.20), which involves an additional complex conjugate in the argument of the bra vector, implies that n_k is the sum of the (complex) squares of the components of $|\phi_k\rangle$, as opposed to being the more familiar sum of the squares of the magnitudes of the components. This necessary peculiarity arises from \mathbf{W} being symmetric but not Hermitian. (In particular the symmetry of \mathbf{W} implies for eigenvalues $w_a \neq w_b$ that $\langle \phi_a^* | \phi_b \rangle = 0$, which ultimately leads to an expression for the unity operator involving a sum of $|\phi_k\rangle \langle \phi_k^*|$ terms instead of the more familiar sum of $|\phi_k\rangle \langle \phi_k|$ terms.)

We note that for $\epsilon = \gamma_s/2 > 0$, w_2 and w_3 *always* have negative imaginary components. As $t \rightarrow \infty$, only the $k = 1$ contribution to (C.19) survives because only w_1 has no decay (or negative imaginary) component. If we initiate the system with one QD excited, then

$$\begin{bmatrix} a_0(0) \\ a_S(0) \\ a_A(0) \end{bmatrix} = \begin{bmatrix} 0 \\ \frac{1}{\sqrt{2}} \\ \frac{1}{\sqrt{2}} \end{bmatrix}. \quad (\text{C.21})$$

The asymptotic amplitude for a_S is then

$$\begin{aligned}
a_S(\infty) &= \langle S | \Psi(\infty) \rangle \\
&= \langle S | \phi_1 \rangle \langle \phi_1 | \Psi(0) \rangle \\
&= \frac{1}{\sqrt{2}(1+x^2)} x(1-x),
\end{aligned} \tag{C.22}$$

where

$$x = \frac{\beta}{\alpha} = \frac{g_1 - g_2}{g_1 + g_2}, \tag{C.23}$$

and we have used the fact that $n_1 = 1 + x^2$. In a similar fashion we find

$$a_A(\infty) = \frac{1}{\sqrt{2}(1+x^2)} (1-x). \tag{C.24}$$

The asymptotic concurrence in this case is simply [39]

$$\begin{aligned}
C(\infty) &= | P_A(\infty) - P_S(\infty) | \\
&= | |a_A(\infty)|^2 - |a_S(\infty)|^2 |.
\end{aligned} \tag{C.25}$$

Since the magnitude of x in (C.23) is always less than 1 when g_1 and g_2 are positive, $P_A > P_S$, and one can ignore the outer absolute signs. The concurrence then reduces to

$$C(\infty) = \frac{1}{2(1+x^2)^2} (1-x)^2 (1+x^2). \tag{C.26}$$

Viewed as a function of x , the maximum of (C.26) is found to be at $x = -2 + \sqrt{3}$, and corresponds to $g_2/g_1 = \sqrt{3}$, consistent with the results in the text. For this value of x , $C(\infty) \approx 0.6495$.

The three-state model above involving the states $|q_1 = 0, q_2 = 0; s = 1\rangle$, $|S; s = 0\rangle$, and $|A; s = 0\rangle$ is convenient because it led directly to simple analytical expressions for the asymptotic concurrence. However, the same result can be obtained, with a little more work, by employing the basis $|q_1 = 0, q_2 = 0; s = 1\rangle$, $|q_1 = 0, q_2 = 1; s = 0\rangle$ and $|q_1 = 1, q_2 = 0; s = 0\rangle$. In fact this approach is advantageous because it then is easily generalizable to $N > 2$ QDs. Assume we have N

QDs, with each QD k interacting only with the dissipative plasmon via a Hamiltonian coupling term $\hbar g_k$. If the basis is taken to be $|q_1 = 0, q_2 = 0, q_3 = 0, \dots; s = 1\rangle$, $|q_1 = 1, q_2 = 0, q_3 = 0, \dots; s = 0\rangle$, $|q_1 = 0, q_2 = 1, q_3 = 0, \dots; s = 0\rangle$, \dots , then one has an $(N + 1) \times (N + 1)$ Hamiltonian matrix representation $\mathbf{H} = \hbar \mathbf{W}$ with

$$\mathbf{W} = \begin{bmatrix} -i\epsilon & g_1 & g_2 & \cdots & g_N \\ g_1 & 0 & 0 & \cdots & 0 \\ g_2 & 0 & 0 & \cdots & 0 \\ \vdots & & & \ddots & \\ g_N & 0 & 0 & \cdots & 0 \end{bmatrix}. \quad (\text{C.27})$$

The characteristic equation for the eigenvalues of \mathbf{W} is then $w^{N-1}(w^2 + i\epsilon w - G) = 0$, where $G = \sum_{k=1}^N g_k^2$. It implies that there are $N - 1$ degenerate eigenvalues $w_1 = w_2 = \dots = w_{N-1} = 0$ and two complex eigenvalues,

$$\begin{aligned} w_N &= (-i\epsilon - \sqrt{4G - \epsilon^2})/2 \\ w_{N+1} &= (-i\epsilon + \sqrt{4G - \epsilon^2})/2. \end{aligned} \quad (\text{C.28})$$

Let $\mathbf{v}^{\mathbf{k}}$ denote the eigenvector corresponding to the k th eigenvalue, and let v_j^k denote the j th component of this eigenvector. One can easily see that the $k = 1, 2, \dots, N - 1$ degenerate eigenvectors must all have $v_1^k = 0$; that is, they contain no component in the basis state $|q_1 = 0, q_2 = 0, \dots; s = 1\rangle$. The remaining components must satisfy

$$\sum_{j=2}^{N+1} g_{j-1} v_j^k = 0. \quad (\text{C.29})$$

Although one can easily solve (C.29) for low N in various ways, a systematic procedure for obtaining $N - 1$ linearly independent and orthogonal eigenvectors is as follows. Notice that (C.29) implies that each of the desired vectors $\mathbf{v}^{\mathbf{k}}$ must be orthogonal to the vector $\mathbf{g} = (0, g_1, \dots, g_N)^T$. Thus one can initially set $N -$

1 vectors with random coefficients and use a Gram-Schmidt procedure initiated with the vector \mathbf{g} , orthogonalizing all subsequent vectors against \mathbf{g} and previously generated vectors.

The final two eigenvectors for $k = N$ and $k = N + 1$ are easily found to have the $j = 1$ components $v_1^N = w_N/g_N$ and $v_1^{N+1} = w_{N+1}/g_N$. Their $j = 2, \dots, N$ components are $v_j^N = v_j^{N+1} = g_{j-1}/g_N$ and, finally, for the $j = N + 1$ components, $v_{N+1}^N = v_{N+1}^{N+1} = 1$. These two eigenvectors are orthogonal to each other and the previous $N - 1$ eigenvectors associated with the degenerate eigenvalue, and we find it convenient to employ them in this way with normalization considerations entering into the propagator representation, (C.19).

With the systematic procedure above for evaluating all the eigenvectors, and introducing the time-dependent amplitudes $b_j(t)$ corresponding to states $j = 1, 2, \dots, N+1$ within the basis $|0, 0, 0, 0, \dots; 1\rangle, |0, 1, 0, 0, \dots; 0\rangle, \dots, |0, \dots, 0, 1; 0\rangle$, one can use (C.19) (extended to $N + 1$ states, of course) to show

$$b_j(t) = \sum_{k=1}^{N+1} \exp(-iw_k t) K_{j,k}, \quad (\text{C.30})$$

where

$$K_{j,k} = \sum_i v_j^k v_i^k b_i(0)/n_k. \quad (\text{C.31})$$

The probabilities for QDs $1, 2, \dots, N$ to be excited are $P_1 = \|b_2\|^2$, $P_2 = \|b_3\|^2$, $\dots, P_N = \|b_{N+1}\|^2$. While obtaining bipartite concurrences may appear arduous, if $b_1(0) = 0$ (i.e., no amplitude in the state corresponds to the plasmon excited with all QDs cold) and all the other amplitudes are real, one can show that the bipartite concurrences are simply $C_{i,j} = 2\sqrt{P_i P_j}$. As with the three-state example, we note that as $t \rightarrow \infty$, only the $k = 1, 2, \dots, N - 1$ eigenvector contributions survive and one could use (C.30), setting the exponential to one and carrying the sum out to

only $k = N - 1$, to evaluate the asymptotic populations.

C.2 Local Field Enhancement

To estimate Rabi-flop frequencies for the QDs, we need an estimate of the local electromagnetic field they experience, which is enhanced relative to the incident field due to the presence of the plasmonic system. To this end, we consider the interaction of one QD with a plasmonic system and employ a classical coupled dipole picture, as in Ref. [50] and associated supplementary material. The time-dependent dipoles for the plasmon ($\mu_s(t)$) and QD ($\mu_q(t)$), in the presence of an incident field with frequency ω satisfy the equations of motion

$$\ddot{\mu}_s(t) + \omega_s^2 \mu_s(t) + \gamma_s \dot{\mu}_s(t) = A_s [E_0 \cos \omega t + \mu_q(t) J] \quad (\text{C.32})$$

$$\ddot{\mu}_q(t) + \omega_q^2 \mu_q(t) + \gamma_q \dot{\mu}_q(t) = A_q [E_0 \cos \omega t + \mu_s(t) J]. \quad (\text{C.33})$$

The parameters ω_s , ω_q , and γ_s are the same as those in the CQED model of Sec. 4.2. The other parameters in these classical equations are related to those in the CQED model as follows:

$$\begin{aligned} J &= \frac{\hbar g}{d_s d_q} \\ A_s &= 2d_s^2 \omega_s / \hbar \\ A_q &= 2d_q^2 \omega_q / \hbar \\ \gamma_q &= 2\gamma_d. \end{aligned} \quad (\text{C.34})$$

Several comments are in order regarding these relations. The relation for J was derived in Ref. [50]. The relations for A_s and A_q reflect exactly solving (C.32) and (C.33) in the limit of the dipoles not interacting ($J = 0$) and equating the resulting amplitudes of oscillation of the dipoles with the corresponding quantum expressions (in the linear or low E_0 limit). These expressions are twice as small as

the previously inferred ones, which were less accurate because they were based on an approximate solution of the classical equations. The classical decay factor γ_q is taken to be twice the corresponding quantum dephasing factor, γ_d . This ensures that the full-width-at-half-maximum of the isolated QD spectrum, inferred from the classical expression with γ_q , is equal to the corresponding quantum result in the low E_0 limit.

We can identify the term $\mu_s(t)J$ in (C.33) as the local electric field the QD experiences because of the plasmon, that is,

$$E^{loc}(t) = \mu_s(t)J. \quad (\text{C.35})$$

For estimating E^{loc} , one can approximate $\mu_s(t)$ by the expression that results from the exact solution of (C.32) in the uncoupled ($J = 0$) and on resonance ($\omega = \omega_s$) limits. This solution is readily obtained by complexifying the equation, that is, by replacing $\cos(\omega t)$ by $\exp(-i\omega t)$, which leads to an equation that is easy to solve exactly. The real part of the complex solution then solves the original, real equation. Thus,

$$\mu_s(t) \approx \frac{A_s E_0}{\omega_s \gamma_s} \sin(\omega t). \quad (\text{C.36})$$

Insertion of (C.36) into (C.35) leads to

$$E^{loc}(t) \approx E_0^{loc} \sin(\omega t), \quad (\text{C.37})$$

where

$$E_0^{loc} = 2 \frac{d_s}{d_q} \frac{g}{\gamma_s} E_0, \quad (\text{C.38})$$

where the expressions in (C.34) have also been used.

BIBLIOGRAPHY

- [1] R. G. Parr, “Density functional theory of atoms and molecules,” in *Horizons of Quantum Chemistry*, pp. 5–15, Springer, 1980.
- [2] M. P. Nightingale and C. J. Umrigar, *Quantum Monte Carlo methods in physics and chemistry*. No. 525, Springer Science & Business Media, 1998.
- [3] G. D. Purvis III and R. J. Bartlett, “A full coupled-cluster singles and doubles model: the inclusion of disconnected triples,” *J. Chem. Phys.*, vol. 76, no. 4, pp. 1910–1918, 1982.
- [4] S. R. White and A. E. Feiguin, “Real-time evolution using the density matrix renormalization group,” *Physical review letters*, vol. 93, no. 7, p. 076401, 2004.
- [5] P. Knowles and N. Handy, “A new determinant-based full configuration interaction method,” *Chemical physics letters*, vol. 111, no. 4-5, pp. 315–321, 1984.
- [6] D. I. Schuster, *Circuit quantum electrodynamics*. Yale University, 2007.
- [7] B. W. Shore and P. L. Knight, “The jaynes-cummings model,” *Journal of Modern Optics*, vol. 40, no. 7, pp. 1195–1238, 1993.
- [8] H.-J. Werner, P. J. Knowles, G. Knizia, F. R. Manby, M. Schütz, P. Celani, W. Györffy, D. Kats, T. Korona, R. Lindh, A. Mitrushenkov, G. Rauhut, K. R. Shamasundar, T. B. Adler, R. D. Amos, A. Bernhardsson, A. Berning, D. L. Cooper, M. J. O. Deegan, A. J. Dobbyn, F. Eckert, E. Goll, C. Hampel, A. Hesselmann, G. Hetzer, T. Hrenar, G. Jansen, C. Köppl, Y. Liu, A. W. Lloyd, R. A. Mata, A. J. May, S. J. McNicholas, W. Meyer, M. E. Mura, A. Nicklass, D. P. O’Neill, P. Palmieri, D. Peng, K. Pflüger, R. Pitzer, M. Reiher, T. Shiozaki, H. Stoll, A. J. Stone, R. Tarroni, T. Thorsteinsson, and M. Wang, “Molpro, version 2015.1, a package of ab initio programs,” 2015. see <http://www.molpro.net>.
- [9] Q. Sun, T. C. Berkelbach, N. S. Blunt, G. H. Booth, S. Guo, Z. Li, J. Liu, J. McClain, S. Sharma, S. Wouters, *et al.*, “The python-based simulations of chemistry framework (pyscf),” *arXiv preprint arXiv:1701.08223*, 2017.
- [10] A. A. Holmes, N. M. Tubman, and C. Umrigar, “Heat-bath configuration interaction: An efficient selected configuration interaction algorithm inspired

- by heat-bath sampling,” *Journal of chemical theory and computation*, vol. 12, no. 8, pp. 3674–3680, 2016.
- [11] S. Sharma, A. A. Holmes, G. Jeanmairet, A. Alavi, and C. J. Umrigar, “Semistochastic heat-bath configuration interaction method: selected configuration interaction with semistochastic perturbation theory,” *Journal of Chemical Theory and Computation*, vol. 13, no. 4, pp. 1595–1604, 2017.
- [12] B. Huron, J. Malrieu, and P. Rancurel, “Iterative perturbation calculations of ground and excited state energies from multiconfigurational zeroth-order wavefunctions,” *J. Chem. Phys.*, vol. 58, no. 12, pp. 5745–5759, 1973.
- [13] In practice the selection of determinants is improved by using a larger ϵ_1 during the early HCI iterations.
- [14] A. A. Holmes, C. Umrigar, and S. Sharma, “Excited states using semistochastic heat-bath configuration interaction,” *arXiv preprint arXiv:1708.03456*, 2017.
- [15] E. R. Davidson, “The iterative calculation of a few of the lowest eigenvalues and corresponding eigenvectors of large real-symmetric matrices,” *Journal of Computational Physics*, vol. 17, no. 1, pp. 87–94, 1975.
- [16] T. Müller, “Large-scale parallel uncontracted multireference-averaged quadratic coupled cluster: The ground state of the chromium dimer revisited,” *Journal of Physical Chemistry A*, vol. 113, no. 45, pp. 12729–12740, 2009.
- [17] H. Dachsel, R. J. Harrison, and D. A. Dixon, “Multireference Configuration Interaction Calculations on Cr₂: Passing the One Billion Limit in MRCI/M-RACPF Calculations,” *The Journal of Physical Chemistry A*, vol. 103, no. 1, pp. 152–155, 1999.
- [18] C. Angeli, R. Cimiraglia, S. Evangelisti, T. Leininger, and J.-P. Malrieu, “Introduction of n-electron valence states for multireference perturbation theory,” *J. Chem. Phys.*, vol. 114, no. 23, p. 10252, 2001.
- [19] P. Celani, H. Stoll, H. J. Werner, and P. J. Knowles, “The CIPT2 method: Coupling of multi-reference configuration interaction and multi-reference perturbation theory. Application to the chromium dimer,” *Molecular Physics*, vol. 102, no. 21-22, pp. 2369–2379, 2004.

- [20] C. Angeli, B. Bories, A. Cavallini, and R. Cimiraglia, “Third-order multireference perturbation theory: the n-electron valence state perturbation-theory approach.,” *J. Chem. Phys.*, vol. 124, no. 5, p. 054108, 2006.
- [21] M. Mirzaei, “A computational NMR study of boron phosphide nanotubes,” *Zeitschrift fur Naturforschung - Section A Journal of Physical Sciences*, vol. 65, no. 10, pp. 844–848, 2010.
- [22] Y. Kurashige and T. Yanai, “Second-order perturbation theory with a density matrix renormalization group self-consistent field reference function: theory and application to the study of chromium dimer.,” *J. Chem. Phys.*, vol. 135, no. 9, p. 094104, 2011.
- [23] F. Ruip, F. Aquilante, J. M. Ugalde, and I. Infante, “Complete vs Restricted Active Space Perturbation Theory Calculation of the Cr₂ Potential Energy Surface,” pp. 1640–1646, 2011.
- [24] S. Seiffert and J. Sprakel, “Physical chemistry of supramolecular polymer networks,” *Chem. Soc. Rev.*, vol. 41, no. 2, pp. 909–930, 2012.
- [25] W. Purwanto, S. Zhang, and H. Krakauer, “An auxiliary-field quantum Monte Carlo study of the chromium dimer,” *J. Chem. Phys.*, vol. 142, no. 6, p. 064302, 2015.
- [26] S. Guo, M. A. Watson, W. Hu, Q. Sun, and G. K.-L. Chan, “N-Electron Valence State Perturbation Theory Based on a Density Matrix Renormalization Group Reference Function, with Applications to the Chromium Dimer and a Trimer Model of Poly(p-Phenylenevinylene).,” *J. Chem. Theory Comput.*, vol. 12, no. 4, pp. 1583–91, 2016.
- [27] C. W. Bauschlicher and H. Partridge, “Cr₂ revisited,” *Chem. Phys. Lett.*, vol. 231, no. 2-3, pp. 277–282, 1994.
- [28] T. H. Dunning Jr, “Gaussian basis sets for use in correlated molecular calculations. i. the atoms boron through neon and hydrogen,” *J. Chem. Phys.*, vol. 90, no. 2, pp. 1007–1023, 1989.
- [29] H.-J. Werner, P. J. Knowles, G. Knizia, F. R. Manby, and M. Schütz, “Molpro: a general-purpose quantum chemistry program package,” *Wiley Interdiscip. Rev.: Comput. Mol. Sci.*, vol. 2, no. 2, pp. 242–253, 2012.
- [30] M. Otten, R. A. Shah, N. F. Scherer, M. Min, M. Pelton, and S. K. Gray,

- “Entanglement of two, three, or four plasmonically coupled quantum dots,” *Phys. Rev. B*, vol. 92, p. 125432, 2015.
- [31] M. Pelton and G. Bryant, *Introduction to Metal-Nanoparticle Plasmonics*. Wiley, 2013.
- [32] Z.-R. Lin, G.-P. Guo, T. Tu, H.-O. Li, C.-L. Zou, J.-X. Chen, Y.-H. Lu, X.-F. Ren, and G.-C. Guo, “Quantum bus of metal nanoring with surface plasmon polaritons,” *Physical Review B*, vol. 82, no. 24, p. 241401, 2010.
- [33] G.-Y. Chen, N. Lambert, C.-H. Chou, Y.-N. Chen, and F. Nori, “Surface plasmons in a metal nanowire coupled to colloidal quantum dots: Scattering properties and quantum entanglement,” *Physical Review B*, vol. 84, no. 4, p. 045310, 2011.
- [34] D. E. Chang, V. Vuletić, and M. D. Lukin, “Quantum nonlinear optics [mdash] photon by photon,” *Nature Photonics*, vol. 8, no. 9, pp. 685–694, 2014.
- [35] J. Poyatos, J. Cirac, and P. Zoller, “Quantum reservoir engineering with laser cooled trapped ions,” *Physical review letters*, vol. 77, no. 23, p. 4728, 1996.
- [36] Y. Lin, J. Gaebler, F. Reiter, T. R. Tan, R. Bowler, A. Sørensen, D. Leibfried, and D. J. Wineland, “Dissipative production of a maximally entangled steady state of two quantum bits,” *Nature*, vol. 504, no. 7480, pp. 415–418, 2013.
- [37] H. Krauter, C. A. Muschik, K. Jensen, W. Wasilewski, J. M. Petersen, J. I. Cirac, and E. S. Polzik, “Entanglement generated by dissipation and steady state entanglement of two macroscopic objects,” *Physical review letters*, vol. 107, no. 8, p. 080503, 2011.
- [38] A. Gonzalez-Tudela, D. Martin-Cano, E. Moreno, L. Martin-Moreno, C. Tejedor, and F. J. Garcia-Vidal, “Entanglement of two qubits mediated by one-dimensional plasmonic waveguides,” *Phys. Rev. Lett.*, vol. 106, p. 020501, 2011.
- [39] D. Martin-Cano, A. Gonzalez-Tudela, L. Martin-Moreno, F. J. Garcia-Vidal, C. Tejedor, and E. Moreno, “Dissipation-driven generation of two-qubit entanglement mediated by plasmonic waveguides,” *Phys. Rev. B*, vol. 84, p. 235306, 2011.
- [40] Y. He and K.-D. Zhu, “Strong coupling among semiconductor quantum dots induced by a metal nanoparticle,” *Nanoscale Res. Lett.*, vol. 7, p. 95, 2012.

- [41] Y. He and K.-D. Zhu, “Optical detection of quantum entanglement between two quantum dots near a metal nanoparticle,” *Quant. Info. Comp.*, vol. 13, pp. 0324–0333, 2013.
- [42] C. Gonzalez-Ballester, F. J. García-Vidal, and E. Moreno, “Non-markovian effects in waveguide-mediated entanglement,” *New Journal of Physics*, vol. 15, no. 7, p. 073015, 2013.
- [43] C. Lee, M. Tame, C. Noh, J. Lim, S. A. Maier, J. Lee, and D. G. Angelakis, “Robust-to-loss entanglement generation using a quantum plasmonic nanoparticle array,” *New Journal of Physics*, vol. 15, no. 8, p. 083017, 2013.
- [44] R. D. Artuso and G. W. Bryant, “Quantum dot-quantum dot interactions mediated by a metal nanoparticle: Towards a fully quantum model,” *Phys. Rev. B*, vol. 87, p. 125423, 2013.
- [45] S. Nicolosi, A. Napoli, A. Messina, and F. Petruccione, “Dissipation-induced stationary entanglement in dipole-dipole interacting atomic samples,” *Physical Review A*, vol. 70, no. 2, p. 022511, 2004.
- [46] M. S. Tame, K. McEnery, Ş. Özdemir, J. Lee, S. Maier, and M. Kim, “Quantum plasmonics,” *Nature Physics*, vol. 9, no. 6, pp. 329–340, 2013.
- [47] C. Gonzalez-Ballester, E. Moreno, and F. Garcia-Vidal, “Generation, manipulation, and detection of two-qubit entanglement in waveguide qed,” *Physical Review A*, vol. 89, no. 4, p. 042328, 2014.
- [48] M. A. Nielsen and I. L. Chuang, *Quantum Computation and Quantum Information*. Cambridge: Cambridge University Press, 2000.
- [49] R. Horodecki, P. Horodecki, M. Horodecki, and K. Horodecki, “Quantum entanglement,” *Rev. Mod. Phys.*, vol. 81, pp. 865–842, 2009.
- [50] R. A. Shah, N. F. Scherer, M. Pelton, and S. K. Gray, “Ultrafast reversal of a fano resonance in a plasmon-exciton system,” *Phys. Rev. B*, vol. 88, p. 075411, 2013.
- [51] M. Min and P. Fischer, “An efficient high-order time integration method for spectral-element discontinuous galerkin simulations in electromagnetics,” *J. Sci. Comput.*, vol. 57, pp. 582–603, 2013.
- [52] K. Uga, M. Min, T. Lee, and P. Fischer, “Spectral-element discontinuous

galerkin lattice boltzmann simulation of flow past two cylinders in tandem with an exponential time integrator,” *Computers & Mathematics with Applications*, vol. 65, no. 2, pp. 239–251, 2013.

- [53] X. Wu, S. K. Gray, and M. Pelton, “Quantum-dot-induced transparency in a nanoscale plasmonic resonator,” *Optics express*, vol. 18, no. 23, pp. 23633–23645, 2010.
- [54] W. K. Wootters, “Entanglement of formation of an arbitrary state of two qubits,” *Phys. Rev. Lett.*, vol. 80, pp. 2245–2248, 1998.
- [55] X. Chen, H.-R. Park, M. Pelton, X. Piao, N. C. Lindquist, H. Im, Y. J. Kim, J. S. Ahn, K. J. Ahn, N. Park, *et al.*, “Atomic layer lithography of wafer-scale nanogap arrays for extreme confinement of electromagnetic waves,” *Nature communications*, vol. 4, 2013.
- [56] P. Kuhler, E.-M. Roller, R. Schreiber, T. Liedl, T. Lohmuller, and J. Feldmann, “Plasmonic dna-origami nanoantennas for surface-enhanced raman spectroscopy,” *Nano letters*, vol. 14, no. 5, pp. 2914–2919, 2014.
- [57] V. V. Thacker, L. O. Herrmann, D. O. Sigle, T. Zhang, T. Liedl, J. J. Baumberg, and U. F. Keyser, “Dna origami based assembly of gold nanoparticle dimers for surface-enhanced raman scattering,” *Nature communications*, vol. 5, p. 3448, 2014.
- [58] M. Geiselmann, R. Marty, J. Renger, F. J. Garcia de Abajo, and R. Quidant, “Deterministic optical-near-field-assisted positioning of nitrogen-vacancy centers,” *Nano letters*, vol. 14, no. 3, pp. 1520–1525, 2014.
- [59] D. Nepal, L. F. Drummy, S. Biswas, K. Park, and R. A. Vaia, “Large scale solution assembly of quantum dot–gold nanorod architectures with plasmon enhanced fluorescence,” *ACS nano*, vol. 7, no. 10, pp. 9064–9074, 2013.
- [60] D. Sun, Y. Tian, Y. Zhang, Z. Xu, M. Y. Sfeir, M. Cotlet, and O. Gang, “Light-harvesting nanoparticle core–shell clusters with controllable optical output,” *ACS nano*, vol. 9, no. 6, pp. 5657–5665, 2015.
- [61] G. M. Akselrod, C. Argyropoulos, T. B. Hoang, C. Ciraci, C. Fang, J. Huang, D. R. Smith, and M. H. Mikkelsen, “Probing the mechanisms of large purcell enhancement in plasmonic nanoantennas,” *Nature Photonics*, vol. 8, no. 11, pp. 835–840, 2014.

- [62] N. Thakkar, C. Cherqui, and D. J. Masiello, “Quantum beats from entangled localized surface plasmons,” *ACS Photonics*, vol. 2, no. 1, pp. 157–164, 2015.
- [63] W. Dür, G. Vidal, and J. I. Cirac, “Three qubits can be entangled in two inequivalent ways,” *Physical Review A*, vol. 62, no. 6, p. 062314, 2000.
- [64] M. Otten, J. Larson, M. Min, S. M. Wild, M. Pelton, and S. K. Gray, “Origins and optimization of entanglement in plasmonically coupled quantum dots,” *Phys. Rev. A*, vol. 94, no. 2, p. 022312, 2016.
- [65] W. Zhang, A. O. Govorov, and G. W. Bryant, “Semiconductor-metal nanoparticle molecules: Hybrid excitons and the nonlinear fano effect,” *Phys. Rev. Lett.*, vol. 97, p. 146804, 2006.
- [66] A. Ridolfo, O. Di Stefano, N. Fina, R. Saija, and S. Savasta, “Quantum plasmonics with quantum dot-metal nanoparticle molecules: Influence of the fano effect on photon statistics,” *Phys. Rev. Lett.*, vol. 105, p. 263601, 2010.
- [67] T. Hartsfield, W.-S. Chang, S.-C. Yang, T. Ma, J. Shi, L. Sun, G. Shvets, S. Link, and X. Li, “Single quantum dot controls a plasmonic cavity’s scattering and anisotropy,” *PNAS*, vol. 112, pp. 12288–12292, 2015.
- [68] W. Zhou, M. Dridi, J. Y. Suh, C. H. Kim, D. T. Co, M. R. Wasielewski, G. C. Schatz, and T. W. Odom, “Lasing action in strongly coupled plasmonic nanocavity arrays,” *Nature Nanotechnology*, vol. 8, pp. 506–511, 2013.
- [69] C. K. Dass, T. Jarvis, V. P. Kunets, Y. I. Mazur, G. G. Salamo, C. Lienau, P. Vasa, and X. Li, “Quantum beats in hybrid metal-semiconductor nanostructures,” *ACS Photonics*, vol. 2, pp. 1341–1347, 2015.
- [70] J. S. Fakonas, H. Lee, Y. A. Kelaita, and H. A. Atwater, “Two-plasmon quantum interference,” *Nature Photonics*, vol. 8, pp. 317–320, 2014.
- [71] J. Larson and S. M. Wild, “A batch, derivative-free algorithm for finding multiple local minima,” *Optim. Eng.*, vol. 17, no. 1, pp. 205–228, 2016.
- [72] J. Larson and S. M. Wild, “Asynchronously parallel optimization solver for finding multiple minima,” Preprint ANL/MCS-P5575-0316, Argonne National Laboratory, MCS Div., March 2016.
- [73] S. M. Wild, “Solving derivative-free nonlinear least squares problems with

POUNDERS,” Preprint ANL/MCS-P5120-0414, Argonne National Laboratory, MCS Div., April 2014.

- [74] S. M. Wild, J. Sarich, and N. Schunck, “Derivative-free optimization for parameter estimation in computational nuclear physics,” *J. Phys. G*, vol. 42, no. 3, p. 034031, 2015.
- [75] W. Dür, G. Vidal, and J. I. Cirac, “Three qubits can be entangled in two inequivalent ways,” *Phys. Rev. A*, vol. 62, p. 062314, Nov 2000.
- [76] J. S. Kim, A. Das, and B. C. Sanders, “Entanglement monogamy of multipartite higher-dimensional quantum systems using convex-roof extended negativity,” *Phys. Rev. A*, vol. 79, p. 012329, Jan 2009.
- [77] H. J. Briegel and R. Raussendorf, “Persistent entanglement in arrays of interacting particles,” *Phys. Rev. Lett.*, vol. 86, pp. 910–913, Jan 2001.
- [78] B. A. Bell, M. S. Tame, A. S. Clark, R. W. Nock, W. J. Wadsworth, and J. G. Rarity, “Experimental characterization of universal one-way quantum computing,” *New Journal of Physics*, vol. 15, no. 5, p. 053030, 2013.
- [79] E. Cohen-Hoshen, G. W. Bryant, I. Pinkas, J. Sperling, and I. Bar-Joseph, “Excitonplasmon interactions in quantum dotgold nanoparticle structures,” *Nano Lett.*, vol. 12, pp. 4260–4264, 2012.
- [80] R. Schirhagl, K. Chang, M. Loretz, and C. L. Degen, “Nitrogen-vacancy centers in diamond: Nanoscale sensors for physics and biology,” *Annual Reviews of Physical Chemistry*, vol. 65, pp. 83–105, 2014.
- [81] M. H. Devoret and R. J. Schoelkopf, “Superconducting circuits for quantum information: An outlook,” *Science*, vol. 339, pp. 1169–1174, 2013.